Biomechanical Characterization and Computational Modeling of the Anterior Eye

A DISSERTATION
SUBMITTED TO THE FACULTY OF THE GRADUATE SCHOOL
OF THE UNIVERSITY OF MINNESOTA
BY

Sara Jouzdani

IN PARTIAL FULFILLMENT OF THE REQUIREMENTS
FOR THE DEGREE OF
DOCTOR OF PHILOSOPHY

Victor H. Barocas

February 2013

Acknowledgments

I would like to thank my advisor, Professor Victor Barocas, who believed in me and gave me the opportunity to become a better scientific researcher. I am grateful for his genuine guidance, allowing me to explore and be innovative. He has been and will always be my great mentor and friend.

I would also like to thank my PhD committee members, Allison Hubel, Alptekin Aksan, John Bischof, and Taner Akkin, for their help and support during the course of my graduate tenure.

I would also like to thank all Barocas lab members who made our work environment both educational and healthy. I would like to specifically acknowledge Dr. Rouzbeh Amini and Dr. Julie Whitcomb, who made my transition in the beginning easier and undoubtedly contributed to my success. Faisal Hadi, Victor Lai, Ramesh Raghupathy, Tina Nagel, Colleen Witzenburg (O'Brien), Amy Claeson, Sarah Hunt, Lazarina (Inka) Gyoneva, Dr. Hallie Wagner, and Dr. Spencer Lake have done much to help me and I consider them among my dearest friends. Also, Eric M. Christiansen and Philip Ytterberg, who assisted me in my research and were as excited about ocular research as I am.

Last but not least, I want to thank my family and friends for their moral support and encouragement during the course of this work. I would particularly like to thank my beloved mom, Dr. Mahboubeh Rezaei, whom I would not be who I am today without her, Thank you mom!

Dedication

This dissertation is dedicated to all the patients who suffer from glaucoma with the hope that this work will be a part of new treatment development.

Abstract

Glaucoma is the second leading cause of blindness worldwide. Certain types of glaucoma are directly related to the iris contour. For example, in primary angle closure glaucoma (ACG), the iris is positioned abnormally to the anterior. In my research project, I tried to reveal the mechanisms underlying iris contour abnormalities using a combination of computational and experimental studies.

The iris contour is determined by the balance of three forces: muscular contractions, iris elastic responses, and hydrodynamic forces. The iris muscular forces arise from activation of the iris constituent muscles while the elastic forces are the result of passive mechanical behavior of the iris. Unlike the other two forces that are generated by the iris, the hydrodynamic forces are caused by the continuous flow of the aqueous humor (AH) in the anterior eye. An accurate and predictive computational model, which could provide insights into pathophysiology of glaucoma and possibly lead to novel therapeutic strategies, must accounts for all of the three elements contributing to the iris contour. As part of the continues investigations in Dr. Barocas's lab at the University of Minnesota, the main purposes of this study were (1) to characterize the passive mechanical properties of the iris, (2) to characterize iris-related risk factors to ACG using anterior segment optical coherence tomography (AS-OCT) technique, and (3) to develop a computational model of the iris-aqueous-humor interaction in the anterior eye during dilation.

The iris is composed of three constituent components: the stroma, the *sphincter iridis*, and the *dilator pupillae*. To quantify the relative stiffness of different sections of the iris, mechanical indentation tests and histological analysis in combination with a three- dimensional finite element (FE) simulation were performed. The iris was divided into three regions and the indentation tests were performed on both anterior and posterior sides of porcine irides. The effective moduli and viscoelastic parameters for all regions were calculated. Three-dimensional anatomically accurate models of iris indentation were generated in ABAQUS, based on histological data. An inverse method was developed to determine depth-dependent elastic properties of the iris by comparing experimental results and FE predictions. The study outcomes supported the hypothesis that the posterior layer was the stiffest and produced larger force with increasing depth.

In addition to the differences in their passive stiffness, the iris constituent components also differ in their physiological function and/or pathophysiological roles. For example, there is clinical evidence that in high-risk patients, pupil dilation, caused by relaxation of sphincter iridis and contraction of dilator pupillae, can lead to acute ACG or exacerbate chronic ACG. To study such risk factors, experimental and computational studies were performed.

In the experimental study, twenty normal subjects underwent complete ophthalmic examination and AS-OCT in a controlled-light study. Dynamic changes of the anterior chamber and the iris configuration were captured during light-to-dark (dilation) and dark-to-light (constriction) conditions in a series of AS-OCT images. The

relationship between iris parameters (like iris volume) and anterior chamber parameters (like anterior chamber angle and anterior chamber volume) with changes of pupil diameter were evaluated. We observed a decrease (increase) in iris volume and anterior chamber angle during dilation (constriction), and no significant change in anterior chamber volume. The results of this experimental study emphasized the idea that relative compressibility of the iris and dynamic pupillary block play important roles in angle closure mechanism.

Furthermore, a mathematical model of the anterior segment was developed to study ACG risk factors. In a fluid-solid interaction model of the anterior segment, the contribution of three anatomical and physiological factors (dilator thickness, AH blockage, and iris compressibility) to changes in anterior chamber angle during pupil dilation was investigated. The model predicted that iris bowing during dilation was driven primarily by posterior location of the dilator muscle and aqueous humor blockage. The model also predicted that the risk of ACG during dilation increased with iris incompressibility, a result consistent with several clinical observations.

Table of Contents

List of Tables

List of Figures

Chapter 1 Nomenclature

1.1 Abbreviations

AC = Anterior Chamber

ACA = Anterior Chamber Angle

ACG = Angle-Closure Glaucoma

AH = Aqueous Humor

AOD500 = Angle Opening Distance at 500 μm

AS-OCT = Anterior Segment Optical Coherence Tomography

FE = Finite Element

IFIS = Intraoperative Floppy Iris Syndrome

IOP = Intraocular Pressure

IR = Iris Root

LPI = Laser Peripheral Iridotomy

MP = Mid-Periphery

OAG = Open-Angle Glaucoma

OCT = Optical Coherence Tomography

+PB = Presence of Pupillary Block

-PB = Absence of Pupillary Block

PDS = Pigment dispersion syndrome

PM = Pupillary Margin

SL-OCT = Slit Lamp Optical Coherence Tomography

TM = Trabecular Meshwork

UBM = Ultrasound Biomicroscopy

1.2 English Letters

= Slope in a linear regression model

= Cross-sectional area

= Intercept in a linear regression model

= Coefficient of quadratic term in the lens position function

= Coefficient of constant term in the lens position function

= Radius of cylindrical tip

= Non-negative material properties

= Distance

= Compressibility term

= Radial unit vector

= Circumferential unit vector

= Instantaneous modulus

= Equilibrium modulus

= Elastic modulus

= Elastic modulus vector

= Sample thickness

= Deformation gradient matrix

= Viscoelastic shear constant in Prony series function

= Shear modulus

= Initial shear modulus

= Indentation depth

= Identity matrix

= Detriment of deformation matrix

= Initial bulk modulus

= Normal unit vector

= Pressure

= Indentation force

= Vector of simulation forces

= Vector of simulation forces

= Distance between the corneal axis and the centroid of the area

= residual vector

(R-squared) = Coefficient of Determination

= Stress

s = Seconds

= Time

= Traction tensor

= Displacement

= Radial displacement

= Axial displacement

= Velocity

= Radial velocity

= Axial velocity

= Volume

= Current position

= Rest position

1.3 Greek Letters

= Premier Lamé coefficients

= Weighting factor

$\Delta P = P_{Posterior} - P_{Anterior}$ = Pressure difference between posterior and anterior chambers

= Distance coefficient in the contact-prevention force

= Correction factor for calculating elastic modules using force-displacement curve

= Second Lamé coefficients

= Weight factors matrix

= Viscosity

= Density

= Cauchy stress

= Cauchy stress for a neo-Hookean material

= Cauchy stress of the dilator

= Cauchy stress of the sphincter

= Cauchy stress of the stroma

= Scalar stress acting on dilator muscle

= Scalar stress acting on sphincter muscle

= Sum of squares of the residuals

= Viscoelastic time constant in Prony series function

ν = Poisson’s ratio

Chapter 2 Introduction

2.1 Ocular Anatomy and Physiology

The eye is a complex organ which is supported and controlled by the extraocular muscles around it. The eye is divided into the posterior segment including the vitreous humor, retina, choroid, and optic nerve and the anterior segment containing the sclera, cornea, iris, and lens (Figure 2-1a).

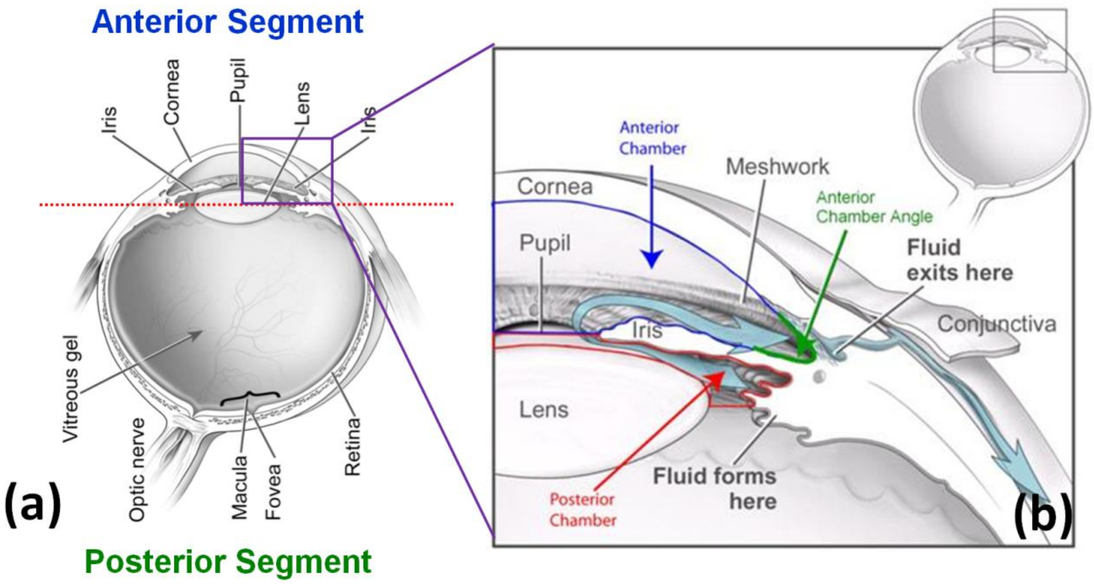

Figure 2-1 (a) Anatomy of the eye composed of the anterior and posterior segments. (b) Anatomy of the anterior segment and flow of AH (image courtesy: National Eye Institute, NIH, Bethesda, MD).

2.1.1 Posterior Segment

The largest structure of the eye is the vitreous humor. The vitreous humor is composed of water (98%), hyaluronic acid, and collagen fibers [1]. This transparent gel plays optical as well as mechanical roles within the eye. It provides a support function by pushing against the posterior surface of the lens during accommodation. During accommodation, the eye moves the lens forward anteriorly to focus on objects at different viewing distances. Clinical and mathematical studies support the idea that the vitreous provides an essential support function during accommodation [2, 3]. The vitreous humor also keeps the retina in place by pressing it against the choroid (Figure 2-1a).

The multi-layered retina lies at the back of the eye and is a derivative of and an extension of the optic nerve. The rods and cones of the retina are responsible for converting light into electrical signals [4].

2.1.2 Anterior Segment

The anterior segment can be divided into two chambers (Figure 2-1a): the anterior chamber, which extends from the cornea to the iris; and the posterior chamber that lies between the iris and the lens.

The cornea is the most anterior structure of the eye globe, a transparent multi-layer tissue, and covers the anterior chamber. The cornea along with the lens and trabecular meshwork is avascular tissues and is nourished by diffusion within the aqueous humor (AH). The lens is positioned posterior to the iris and plays an important role in the refraction of light and accommodation. In the following sections an overview of the anatomy and physiology the AH flow and iris is presented.

2.1.2.1 Aqueous Humor

AH provides oxygen and nutrients to the lens and cornea and carries away waste products from the metabolism of ocular avascular tissues [5]. It flows from the ciliary body into the posterior chamber, and through the pupil, and it drains into the anterior chamber (Figure 2-2). The angle between the anterior surface of the iris and the posterior surface of the cornea is defined as the anterior chamber angle (ACA). The ACA is typically about 30° in the normal eye (Figure 2-2). The majority of aqueous flow exits through the trabecular meshwork into Schlemm's canal. The other main outflow pathways are through uveoscleral outflow, the vitreous gel, and the retina [6].

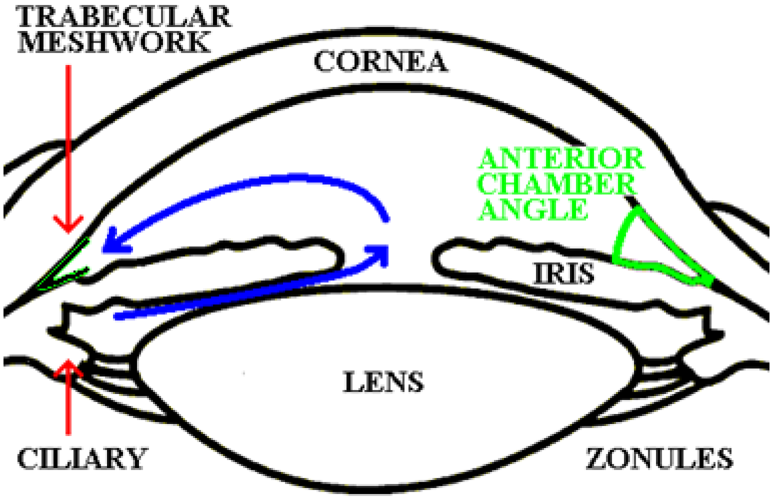

Figure 2-2 Anatomy of the eye composed of the anterior and posterior segments. The ACA is the angle between the posterior cornea and anterior iris.

The rate of AH outflow varies between 2.4-3.0 μL/min which has a slower rate at night and for older people [7]. AH flow meets some resistance during the passage from the posterior chamber into the anterior chamber. By crossing through the narrow gap between the iris and the lens, a small resistance is generated. This phenomenon is termed relative pupillary block. Also, drainage of the AH flow through the trabecular meshwork produces a largest resistance which is the major contributor to intraocular pressure (IOP). The IOP, the pressure inside of the eye, can be calculated from the Goldmann equation and is related to the AH rate, which is inversely related to the outflow facility. The IOP is approximately 15.7-21.3 mmHg in the normal eye [8, 9]. However, long-term and short-term variations in IOP have been reported. Fluctuation of IOP could be produced during the day or night, but the lowest amount was reported during sleep [10]. Exercise and changes in elevation could also have an effect on IOP [11].

2.1.2.2 Iris

The iris muscle is responsible for determining the size of the pupil and in regulating the amount of light reaching the retina. The thickness of the iris is reported to be 0.6 mm and 0.5 mm near the pupillary margin and iris root, respectively [4]. Human pupil diameter can vary between 1.0 mm to 9.0 mm at maximum constriction and maximum dilation, respectively [12]. In addition to the elastic forces generated by mechanical behavior of the iris, iris movement is determined by two factors: (1) the hydrodynamic forces caused by the continuous flow of the AH and (2) internal stresses arise that from activation of the iris constituent.

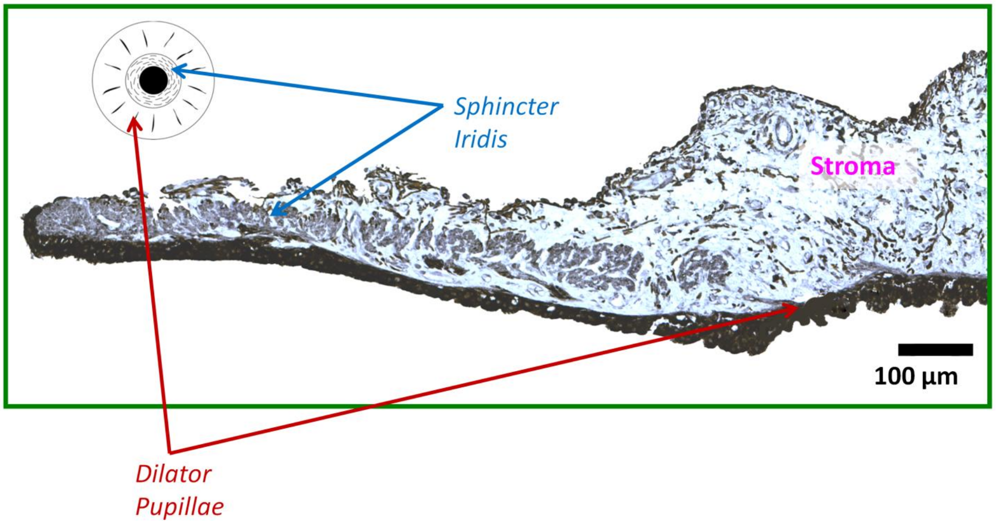

Figure 2-3 Histological cross-section of the porcine iris showing its three comprising segments: the *Sphincter Iridis*, *dilator pupillae* and stroma (histology image is from Julie E. Whitcomb)

The iris is composed mainly of three components, the *sphincter iridis*, the *dilator pupillae*, and the stroma (Figure 2-3). These three main layers are reviewed in the subsequent sections:

The sphincter muscle is a smooth muscle located near the pupillary margin on the posterior surface of the iris. The average thickness of the sphincter muscle is 0.1-0.17 mm with a thickness of 0.75-0.8 mm for humans [4]. In the porcine model the average sphincter thickness is 0.134 mm [13]. The sphincter iridis is oriented circumferentially and innervated by the parasympathetic nervous system to contract the iris. The stimulation of sphincter muscle can uniformly reduce the pupil size. Although it is not clear whether the dilator muscle is in its relaxed state during the iris contraction, the sphincter muscles shortens by 87% in length as the pupil size is reduced from 8.00 mm to 1.5 mm in diameter [4].

The dilator muscle layer has a thickness of 4.0-6.0 μm and is located on the posterior surface of the iris [4, 14]. The periphery of the dilator muscles extends to the iris root and disappears to the midportion of the sphincter muscle [4]. In contrast with the sphincter, the *dilator pupillae* is arranged radially and is innervated by the sympathetic nervous system [12].

The stroma is located on the anterior side of the iris and is composed of a collagen network that supports the structure of the iris. The loose nature of the tissue allows AH flow to move in and out of the stroma during dilation and contraction. The communication of AH flow between the iris stroma and the anterior chamber had been shown using injected ink [15]. More recently, Quigley et al. [16] reported the iris volume is decreased during pupil dilation, demonstrating that the AH can freely pass into the iris stroma.

2.2 Iris Contour Abnormalities and Glaucoma Care

Glaucoma refers to a group of eye disorders that results in damage to the optic nerve, and eventually, loss of vision. Glaucoma is typically characterized by an increase in IOP. In recent decades the glaucoma classification emphasizes the importance of visually significant optic nerve damage [7]. Glaucoma is the most common cause of irreversible blindness worldwide as results of glaucoma. Over 60 million people worldwide affected where 8.4 million became bilaterally blind [7]. Studies have shown

Latino Americans and African Americans are at a greater risk of developing glaucoma than other ethnic populations [17]. The two major types of glaucoma are primary open-angle glaucoma (OAG) and primary angle-closure glaucoma (ACG).

2.2.1 Primary Open-Angle Glaucoma

The most prevalent form of glaucoma is OAG. OAG occurs spontaneously where there is no apparent ocular or systemic mechanism, without any hereditary predisposition. In OAG, outflow of the AH through the trabecular meshwork is obstructed, which increases the IOP, however, the angle remains open. Eventually, high IOP may result in irreversible optic nerve damage and vision loss (specifically peripheral vision loss). Also, the ACA for patients with OAG is always open whether the angle is wide or narrow or the IOP is normal or high [18].

2.2.2 Primary Angle-Closure Glaucoma

ACG is defined as obstruction of aqueous outflow via the trabecular meshwork by the peripheral iris when the ACA is extremely narrowed (Figure 2-4). When the angle is closed, the IOP may become very high, causing symptoms such as blurred vision and pain. Some cases of ACG are involved with pupillary block, a mechanism in which the flow of aqueous from the posterior to the anterior chamber is inhibited due to the small gap between the iris and the lens. Additionally, the iris is abnormally positioned towards the anterior [18].

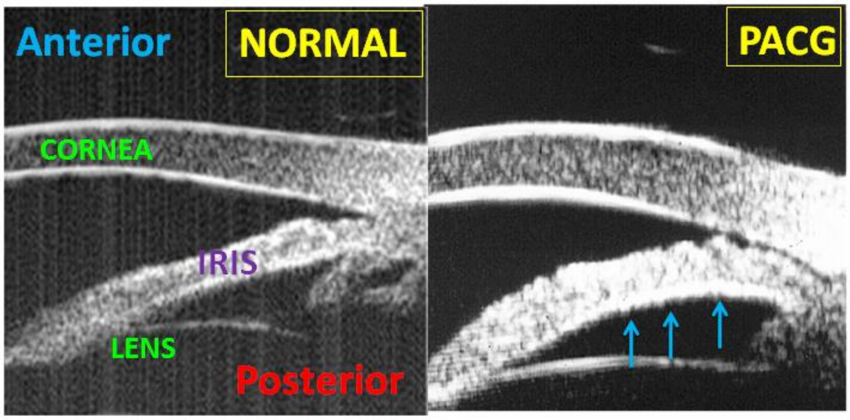

Figure 2-4 UBM images of (left) normal eye and (right) ACG.

Several studies show that small eye size, a thick lens, steeper anterior lens curvature, relatively anterior lens position, and short anterior chamber depth are all risk factors for ACG [19, 20]. Although, the risks of precipitating acute angle closure by dilation is still uncertain, there are studies that have shown a significant increase in IOP [21]. Therefore, the dynamic changes of the iris configuration during dilation have received attention recently.

Iris shortening, increased iris thickness and convexity [22, 23], decreased cross-sectional area and iris volume, [16, 24]and dynamic changes of the iris during dilation have been shown as risk factors in angle closure glaucoma.

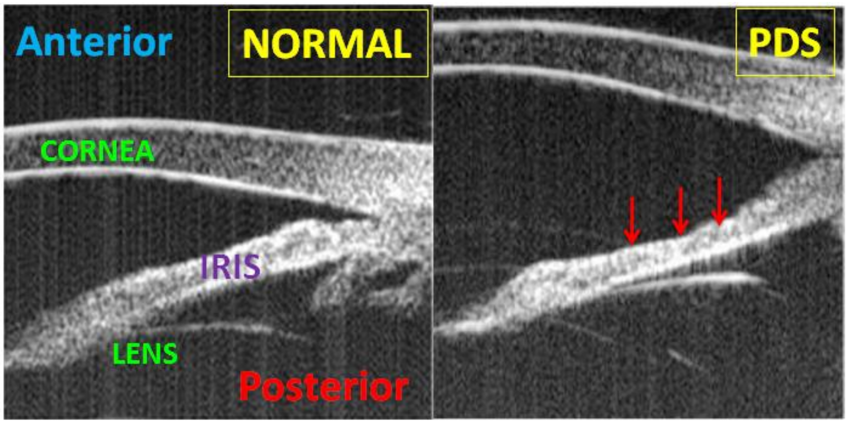

Figure 2-5 UBM images of (left) normal eye, (right) PDS provided by Dr. Prata, New York Eye and Ear Infirmary.

2.2.3 Pigment Dispersion Syndrome

Pigment dispersion syndrome (PDS) is a common secondary glaucoma characterized by loss of pigment from the posterior iris surface into the AH. PDS usually occurs in response to the rubbing of the iris surface against the lens zonules. As a result, excessive pigment deposition in the intraocular structures such as the trabecular meshwork causes IOP elevation and optic disc damage. The anterior chamber is often deeper for patients with PDS [25].

Clinical studies show that PDS is involved with reverse pupillary block. In the reverse pupillary block mechanism, backward flow of AH results in higher pressure in the anterior chamber than in the posterior chamber, and the iris is abnormally bowed towards the posterior which causes an increase in iris–zonule and iris–lens contact (Figure 2-5).

Figure 2-6 Surgical image showing iris billowing, progressive intraoperative miosis and iris prolapse from the surgical incision [26].

2.2.4 Intraoperative Floppy Iris Syndrome

In addition to glaucoma, other syndromes such as intraoperative floppy iris syndrome (IFIS) are directly related to the iris contour. IFIS was first described by Chang and Campbell (2005) who proposed that IFIS was associated with the use of tamsulosin (Flomax) [26]. Tamsulosin is a systemic sympathetic α-1A antagonist that by binding to the postsynaptic nerve of the iris dilator pupillae relaxes this smooth muscle. Patients undergoing cataract surgery who were taking tamsulosin have more risk of developing IFIS.

Poor preoperative pupillary dilation, flaccid and prolapsed iris stroma, and progressive intraoperative pupillary constriction are observed during cataract surgery as IFIS symptoms (Figure 2-6).

Recent research has shown that other systemic sympathetic α-1A antagonists such as alfuzsion, terazosin, and doxazosin might be associated with IFIS by leading to disuse or atrophy of the iris, particularly of the dilator pupillae muscle [26, 27]. Current morphological studies are looking at the effect of tamsulosin on the human iris. The dilator and sphincter muscle thickness of a group of patients was measured using optical coherence tomography (OCT) by Prata et al. [28] and with light microscopy by Santaela et al. [14]. Both reports agreed that the average iris dilator thickness was significantly different between tamsulosin-treated eyes as compared with control eyes. These studies suggest that systemic α-1 adrenergic receptor antagonists like tamsulosin could be the reason for structural alteration of the iris tissue.

2.2.5 Diagnosis of Glaucoma

A basic ophthalmological examination is usually performed to screen for glaucoma. An ophthalmologist may perform tests to measure the patient’s refraction, IOP, ACA, and visual field.

OCT is an imaging technique that captures a stereoscopic, 3D, view of the eye. It also provides useful information about the anterior segment such as anterior chamber depth, and ACA. During the OCT test, the AH is examined for pigment granules. The iris is also transilluminated to assess the loss of posterior iris pigment to diagnose PDS or to look for tears in the pupillary sphincter. The anterior chamber volume, the concavity of the peripheral iris, and the curvature of the lens may be evaluated. The anterior surface of the lens capsule could be examined to observe exfoliation, pigment on the zonules and other abnormalities. However, the examination is not completed until the IOP is measured.

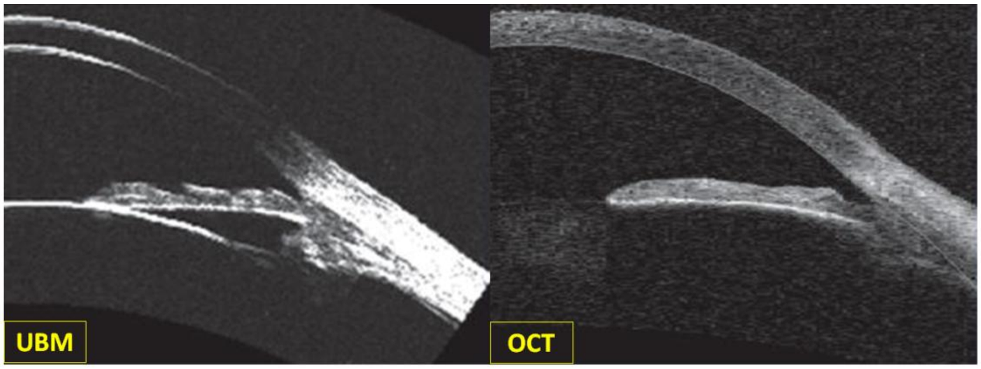

Figure 2-7 (right) Anterior segment OCT and (left) UBM images [29].

Ultrasound biomicroscopy (UBM), like OCT, is designed for imaging the anterior segment of the eye. It provides the ability to view *in vivo* cross sections of the structures of anterior segments with a resolution of approximately 50 μm (Figure 2-7). High resolution anterior segment imaging has allowed ophthalmologists to elucidate numerous aspects of the pathophysiology of eye disorders [30].

Raised IOP is the most important modifiable risk factor for the development and progression of glaucomatous optic neuropathy. A tonometer is an ocular instrument that examiners use to evaluate the IOP. The Maklakov tonometer is the simplest type of tonometer whereas the Goldmann tonometer is considered the most accurate and standard one (Figure 2-8). Since the device in some cases makes contact with the cornea, an eye drop such as proparacaine is introduced onto the surface of the eye. The tonometer is pushed against the cornea and the force required to flatten a certain area of the cornea is converted to pressure.

Figure 2-8 Maklakov (left) and Goldmann tonometer (right).

Reliable knowledge about the anatomy of the anterior segment, particularly the ACA, could help ophthalmologists to better manage glaucoma. Indentation gonioscopy is a clinical techanique and standard tool in the evaluation of the ACA. In an indentation gonioscopy test, a goniolens is pushed against the cornea of patient to characterize the iris contour and measure the ACA (Figure 2-9). Measured angles of 20-35° are classified as open angle whereas less than 10° measured angles are categorized as very narrow angle/closed angle [7].

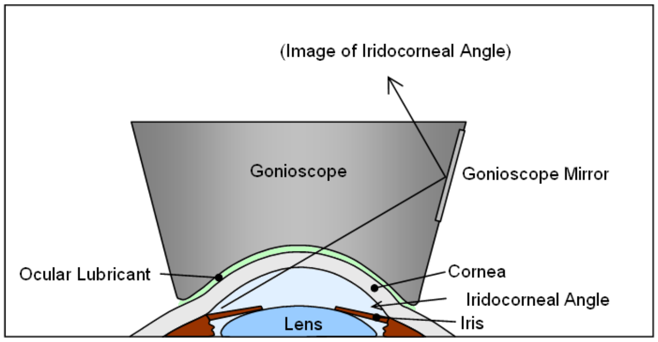

Figure 2-9 Gonioscopy schematic

In normal eyes, due to greater pressure in the posterior chamber rather than the anterior chamber, the iris has a convex periphery. In contrast, a flat or concave iris contour may be associated with plateau iris or PDS, respectively. The ACA is narrowed and consequently not visible in gonioscopy. However, by indenting the gonioscopy toward the cornea, the narrowed angle chamber angle can be opened [31].

2.2.6 Current Glaucoma Treatment

Pharmaceuticals (applied directly or taken orally) often are the first common treatment for glaucoma. These include prostaglandin analogs, beta blockers, sympathomimetics, carbonic anhydrase inhibitors, and parasympathomimetics. Glaucoma eye drops can be very effective at reducing IOP and preventing eye damage, although like other eye drops, they can cause side effects on different patients. Pilocarpine is an example of a parasympathomimetic. Clinical studies have reported adding a small amount of pilocarpine into the anterior camber of the eye can reduce the anterior chamber volume and rate of AH production and increase the rate of AH outflow and the IOP [32]. It also reduces the size of the pupil that can cause a lessening in vision and can prevent normal dilation [33].

Laser Peripheral Iridotomy (LPI) was first used to treat ACG, although it may be performed to treat OAG and PDS as well. LPI is a procedure where a surgeon makes a small hole in the peripheral iris to facilitate the flow of AH from the posterior to the anterior chamber. This application allows equilibrating the pressure between the chambers which eliminates the relative pupillary block and eventually lowers the IOP

[18]. Although LPI is almost performed exclusively in patients with angle closure glaucoma and is known as a safe application, there are some risks to consider in this procedure, including corneal endothelial cell damage [32], inflammation, and bleeding of the eye. Also, it could injure the lens by damaging it directly due to the laser itself or indirectly by lessening the circulation of the AH around the lens and reducing lens nourishment [34]. Several studies have reported that the IOP after performing LPI was not significantly decreased in patients [35, 36]. Moreover, in some cases the surgeon manages to perform more than one LPI [18].

While the current pharmacological and surgical treatments of glaucoma are considered quite successful to save remaining vision, they cannot improve lost sight. Moreover, there are risk factors and side effects associated with these treatments. Therefore, the need to improve therapeutic techniques is an immediate problem. Understanding the dynamic behavior of the anterior segment, particularly the pathophysiology of the iris, will help us to improve diagnosis and general treatment strategies for iris contour abnormalities.

Chapter 3 Analysis of the Anterior Segment during Dynamic Pupil Dilation and Constriction using Optical Coherence Tomography

(This work was part of the paper “Analysis of the Anterior Segment during Dynamic Pupil Dilation and Constriction using Optical Coherence Tomography” by Sara Jouzdani, Eric M. Christiansen, Syril Dorairaj, Alfredo Castillejos, Jeffrey M. Liebmann, Robert Ritch, and Victor H. Barocas, Clinical and Experimental Ophthalmology 2012, In review)

3.1 Summary

The purpose of this study was to examine the dynamic changes in iris configuration and anterior chamber (ACA) during pupil dilation and constriction using anterior segment optical coherence tomography (AS-OCT). Twenty normal subjects underwent complete ophthalmic examination and AS-OCT in a controlled-light study. Dynamic changes of anterior chamber (AC) and iris configuration were captured during light-to-dark (dilation) and dark-to-light (constriction) conditions in a series of AS-OCT images. The relationship between iris parameters - iris chord length, curvature, concavity ratio, cross-sectional area, and volume - and AC parameters - AC cross-sectional area, volume, and angle opening distance (AOD500) - with changes in pupil diameter were evaluated. The hysteresis area of each measured variable vs. pupil diameter during dilation and constriction was calculated to examine possible asymmetry between dilation and constriction at the same pupil diameter. The iris curvature and concavity ratio

increased with dilation while AOD500, chord length, cross-sectional area, and volume of the iris decreased significantly ($p < 0.05$, paired t-test). The reverse occurred for all measurements during constriction. AC cross-sectional area and volume did not change significantly during pupil dilation or constriction ($p > 0.05$). No significant effect was observed in the hysteresis area calculations. The volume of the AC did not change significantly during dilation or constriction.

3.2 Introduction

Angle closure glaucoma (ACG) is a major cause of irreversible blindness [37]. Although the anatomical basis of ACG is not fully understood, closing or narrowing of the angle is often attributed to pupillary block, in which the flow of aqueous humor (AH) from the posterior chamber to the AC is inhibited due to the small gap between the central posterior iris surface and the anterior surface of the lens. Higher pressure in the posterior chamber generates a net force that bows the iris anteriorly, resulting in narrowing of the ACA and blockage of the aqueous outflow pathway. Although it is well known that pupillary block is a major mechanism causing ACG, its contribution during dilation is not clear. We have shown theoretically [38, 39] that pupillary block of the steady AH flow (static pupillary block) does not explain the tendency of the angle to narrow with dilation. Moreover, no significant change in posterior chamber volume was observed during dilation by Dorairaj et al. [40] All of these studies suggest that dynamic motion of the iris may provide a more reasonable mechanism to capture the behavior of pupillary block rather than *static* pupillary block mechanism. We define this mechanism as "*dynamic* pupillary block," in which AH is trapped temporarily in the posterior chamber and causes the anterior iris bowing.

Iris thickness, particularly in the iris root region, and iris curvature increase significantly [22, 23, 41-43] during pupil dilation while ACA, iris cross-sectional area, and iris volume decrease [16, 44, 45]. The stroma is composed of a network of loosely organized collagen and interstitial fluid [15]. Therefore, loss of the iris volume during dilation may be due to motion of the extracellular fluid out of the iris and into the AC.

The changes with dilation, however, are often examined only in light vs. dark conditions rather than at a series of light levels, and there is often little control over the light level. Further, effects involving fluid flow - (1) dynamic pupillary block and trapping of AH in the posterior chamber, and (2) exudation/imbibition of AH by the iris stroma [16] - could produce an asymmetry between dilation and constriction. In the case of dynamic pupillary block, one would expect that the iris would be pushed to the AC during dilation, but would be pushed to the posterior by fluid trapped in the AC during constriction, similar to reverse pupillary block [46-49]. Amini et al. [50] have shown recently that the posterior location of the dilator can contribute to the anterior iris bowing using a non-pupillary block dependent mechanism. Anterior bowing of the iris as a result of the contraction of the dilator, located in the extreme posterior of the iris and in the absence of the aqueous dynamic pressure change, suggests that the dilator muscle's anatomical location affects the iris configuration during dilation. Thus, a controlled-light study of pupil dilation and constriction could provide more insight into the role of different effects in determining iris contour changes during dilation and consequently the mechanism of angle closure with dilation. Specifically, we tested the hypothesis that there would be a dilation/constriction hysteresis, as would be predicted by the dynamic pupillary block model. The objective of this work was to assess whether there are significant differences in the iris configuration during dilation and constriction at the same pupil diameter.

3.3 Methodology

3.3.1 *In Vivo* Experiments (S. Dorairaj, A. Castillejos, and J. Liebmann)

The study followed the tenets of the Declaration of Helsinki and was approved by the Institutional Review Board (IRB) for Human Research of New York Eye and Ear Infirmary. A total of 20 volunteer subjects were prospectively enrolled after obtaining informed consents. All subjects underwent a complete ophthalmic examination, including a review of medical history; measurement of best-corrected visual acuity (BCVA); slit-lamp biomicroscopy; Goldmann applanation tonometry (GAT); gonioscopy; and dilated fundoscopic examination. All eyes were normal on gonioscopic examination and showed no evidence of a glaucomatous optic disc or IOP elevation. Subjects with a history or current use of topical or systemic medication that could affect the angle or the pupillary reflex, those with a history of previous intra-ocular surgery and lasers, and those unable to fixate prior to the AS-OCT examination were excluded. One eye was randomly selected for an AS-OCT examination and analysis. All participants were imaged in terms of the nasal and temporal angle (0-180°) using AS-OCT system with resolution < 25 µm and a lateral resolution of 20-100 µm (1310-nm diode laser; Heidelberg Engineering, Heidelberg, Germany). Images were acquired at different standardized lighting conditions, grading from light to dark to light, by a single well-trained operator. Participants were asked to sit back after imaging and wait for 15 seconds, during which the lighting conditions were changed. After 15 seconds of subject adaptation to the new lighting conditions, images were re-acquired. Subjects were examined in a room equipped with a 100 W lamp attached to a home-made, pedal-activated step dimmer switch. The lamp was initially set at full power (100 W), and then was stepped down to 0 W (room lit only by the light from the examiner's computer) and back up to 100 W in 25 W increments (Figure 3-1).

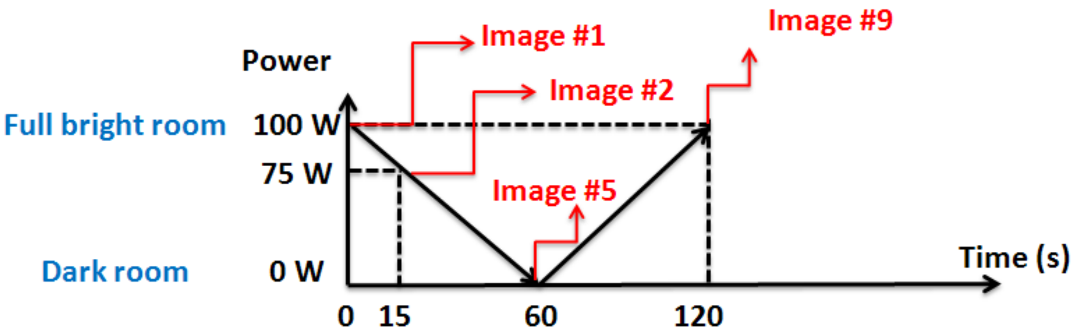

Figure 3-1 Lamp power (Watt) over time (seconds). 5 images were taken over 60 seconds when the light power changed from full power (100 W) to 0 W and 5 images when the light power backed up to full power (100 W).

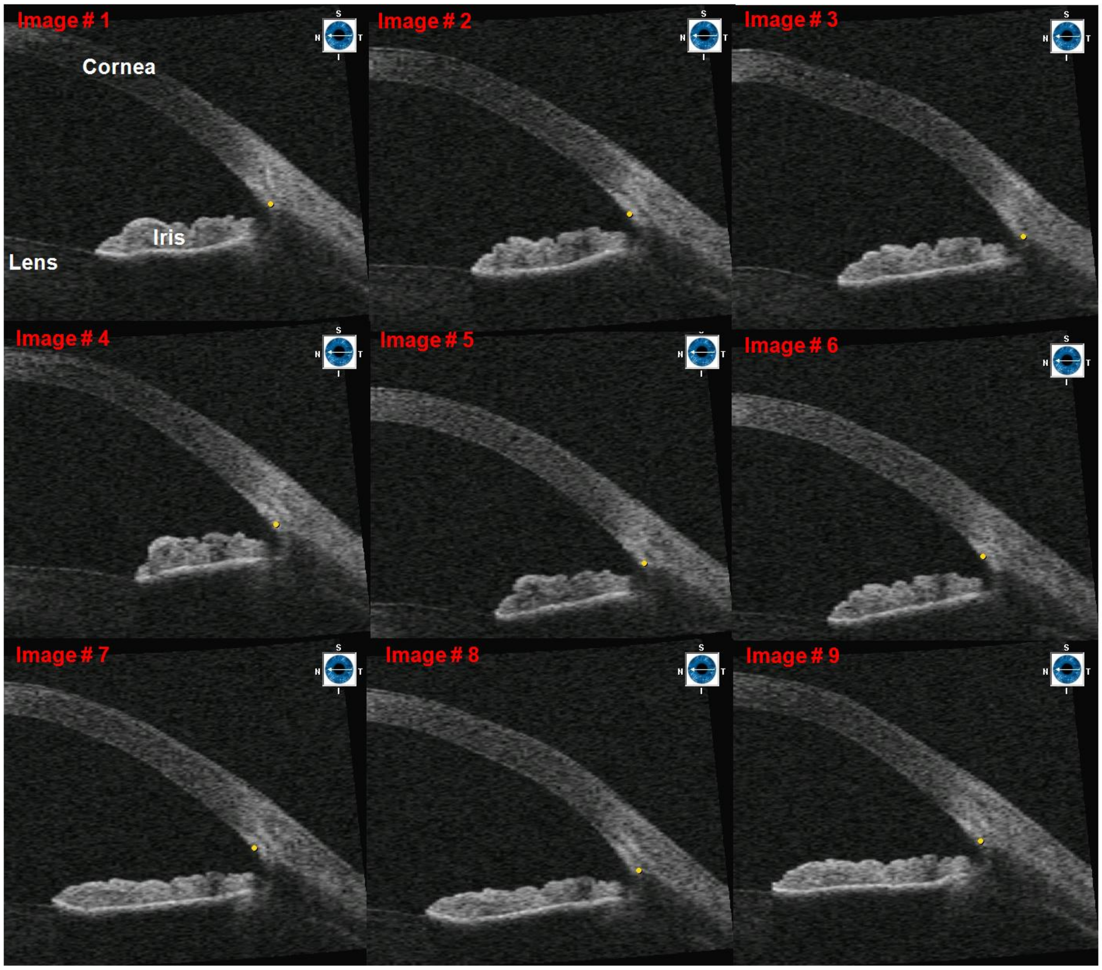

Figure 3-2 Typical AS-OCT images of one subject. Dilation occurred during the first 60 seconds (images 1-5) and followed by constriction during the second 60 seconds (images 5-9).

A total of 9 images were captured for each subject. Dilation occurred between 0 and 60 seconds (images 1-5) and followed by constriction between 60 and 120 seconds (images 5-9) as shown in Figure 3-2. Each AS-OCT image consists of 944 × 524 pixels (lateral × axial). The lateral scanning width was set to 15 mm.

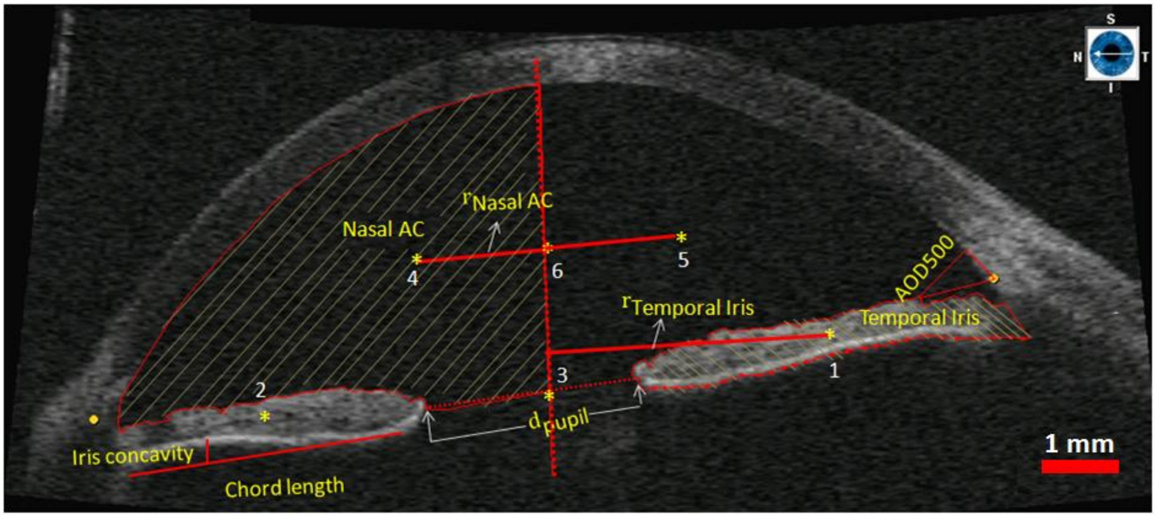

Figure 3-3 Typical AS-OCT image. Anterior segment and iris parameters using imageJ software: The pupil diameter, area and centroids of anterior nasal iris (1), temporal iris (2), AC (3), nasal AC (5), temporal AC (6), iris chord length, iris curvature, and AOD500.

3.3.2 Image analysis (S. Jouzdani and E. Christiansen)

Anterior segment parameters for each image were evaluated by two different independent observers who were masked to other test results and clinical information on participants.

Quantitative analysis of the AC and iris configuration (Figure 3-3) was performed using the ImageJ software available from the National Institutes of Health [51].

The pupil diameter was calculated by drawing a line across the pupil margin. The AC, the nasal iris, and the temporal iris were traced manually, and their areas and centroids (center of area) were calculated via a custom ImageJ macro (points 1 and 2 in Figure 3-3). The center of the pupil was defined as the midpoint of the line segment joining the centroids of nasal and temporal iris cross-sectional areas (point 3 in Figure 3-

3). We also considered calculating the pupil center by taking the midpoint of between iris tips, but the first method was found to be more accurate in slanted images. The AC area and its centroid (points 6 in Figure 3-3) were calculated. The corneal axis was drawn through the centroid of the AC and the center of the pupil (the dashed line in Figure 3-3). The corneal axis allowed us to divide the AC in two areas (i.e. temporal and nasal AC) and AC nasal (points 4 in Figure 3-3) and temporal (points 5 in Figure 3-3) centroids. The volume of the solid formed by rotating the AC and iris (both nasal and temporal) areas around the corneal axis was estimated by the following expressions

$$/2 \qquad 3\text{-}1$$

$$/2 \qquad 3\text{-}2$$

where is the distance between the corneal axis and the centroid of iris or AC, and is the cross-sectional area of the iris or AC. These formulas are equivalent to averaging the volumes calculated separately based on the nasal and temporal halves of the image. In the case of equal nasal and temporal regions, Equations 3-1 and 3-2 reduce to the well-established theorem of Pappus [52].

AOD500 was measured by drawing a perpendicular line from the cornea at 500 μm from the scleral spur to the iris surface as shown in Figure 3-3. The scleral spur was defined as the point at which a change in curvature of the inner surface of the angle wall became apparent, often presented as an inward protrusion of the sclera [53]. The iris chord length was defined by drawing a line from the most peripheral point of the iris to the iris tip. Iris curvature was measured by drawing a perpendicular line from the chord to the iris pigment epithelium at the point that had the largest distance from the iris chord length as shown in Figure 3-3. The iris concavity ratio was also calculated, defined as the ratio between iris curvature and chord length [50]. Distances were converted from pixels using the manufacturer's recommended factor of 0.016 mm/pixel. Linear regression was performed on both the dilation and constriction phases to assess significance of the changes observed, and the coefficient of determination ( ) was also calculated. Furthermore, in order to examine the difference between dilation and constriction, the hysteresis area, that is the area between the dilation and constriction curve, for each variable. A small hysteresis area indicated little difference between the dilation and constriction curves, whereas a large hysteresis area indicated that quantity of interest was different between dilation and constriction at the same light level. The average of both nasal and temporal measured values for chord length, curvature, AOD500, and AC and iris cross-sectional areas was used for the analysis. Unless stated otherwise, values are reported as mean ± 95% CI. Effects with *p*-value less than 0.05 ($p < 0.05$) were deemed significant; those with ($p < 0.1$) were deemed trends.

3.4 Results

The 20 subjects had mean age of 32.7 ± 4.2 years, 40% were Asian (8/20), 55% were Caucasians (11/20) and 5% (1/20) was African American, including 8 female and 12 male subjects. Figure 3-3 shows the change in each measured variable for dilation ($t = 0\text{-}60$ sec) and constriction ($t = 60\text{-}120$ sec) phases using simple linear regression

3-3

where , are the slope and intercept respectively, and the linear regression results including *p*-value, and R-squared ( ) were calculated and reported in Table 3-1. As summarized in Table 3-1, all parameters changes significantly during dilation and constriction except for AC cross-sectional area and volume.

Table 3-1 Summary of linear regression model.

Parameter [value (t) - value(t=0)]	**Intercept ( )**	**Slope ( )**	*p*-value	
Dilation (t = 0-60 sec)				
Pupil Diameter (mm)	0.056	0.022	<0.0001	0.99
Iris Area (mm^2)	0.003	-0.004	<0.0001	0.99
AC Area (mm^2)	0.235	0.004	0.482	0.18
Iris Volume (µL)	-0.188	-0.059	<0.005	0.98
AC Volume (µL)	1.570	-0.029	0.468	0.19
Iris Curvature (mm)	-0.030	0.002	<0.05	0.78
Iris Chord length (mm)	0.010	-0.011	<0.0001	1.00
Concavity ratio	0.007	5.63e-4	<0.05	0.86
AOD500 (mm)	-0.015	-0.004	<0.05	0.98
Constriction (t = 60-120 sec)				
Pupil Diameter (mm)	3.222	-0.032	<0.005	0.97
Iris Area (mm^2)	-0.646	0.006	<0.005	0.97
AC Area (mm^2)	0.845	-0.006	0.883	0.88
Iris Volume (µL)	-7.002	0.059	<0.05	0.87
AC Volume (µL)	0.380	0.003	0.843	0.02
Iris Curvature (mm)	0.240	-0.002	<0.005	0.96
Iris Chord length (mm)	-1.543	0.015	<0.005	0.97
Concavity ratio	0.066	-5.08e-4	<0.005	0.93
AOD500 (mm)	-0.437	0.002	<0.05	0.93

As expected, the pupil diameter changed significantly with light level (Figure 3-4 a). There was no significant change of AC cross-sectional area (Figure 3-4b) or volume (Figure 3-4c). Unlike the AC, the iris cross-sectional area (Figure 3-4d) and volume (Figure 3-4e) both showed a significant decrease with dilation and a significant increase with constriction, consistent with observations by others [16, 44] and with the idea that there is fluid transfer between the iris and the AH. It is suspected that the relatively small amount of volume passed between the iris and AC was not sufficient to be resolved within the accuracy of the AC measurement in Figure 3-4b and c. AOD500 decreased during dilation and increased during constriction (Figure 3-4f). The iris curvature increased with dilation (Figure 3-4g), and the iris chord length decreased (Figure 3-4h). Therefore, the concavity ratio increased with dilation (Figure 3-4i). The reverse occurred for all three measurements during constriction.

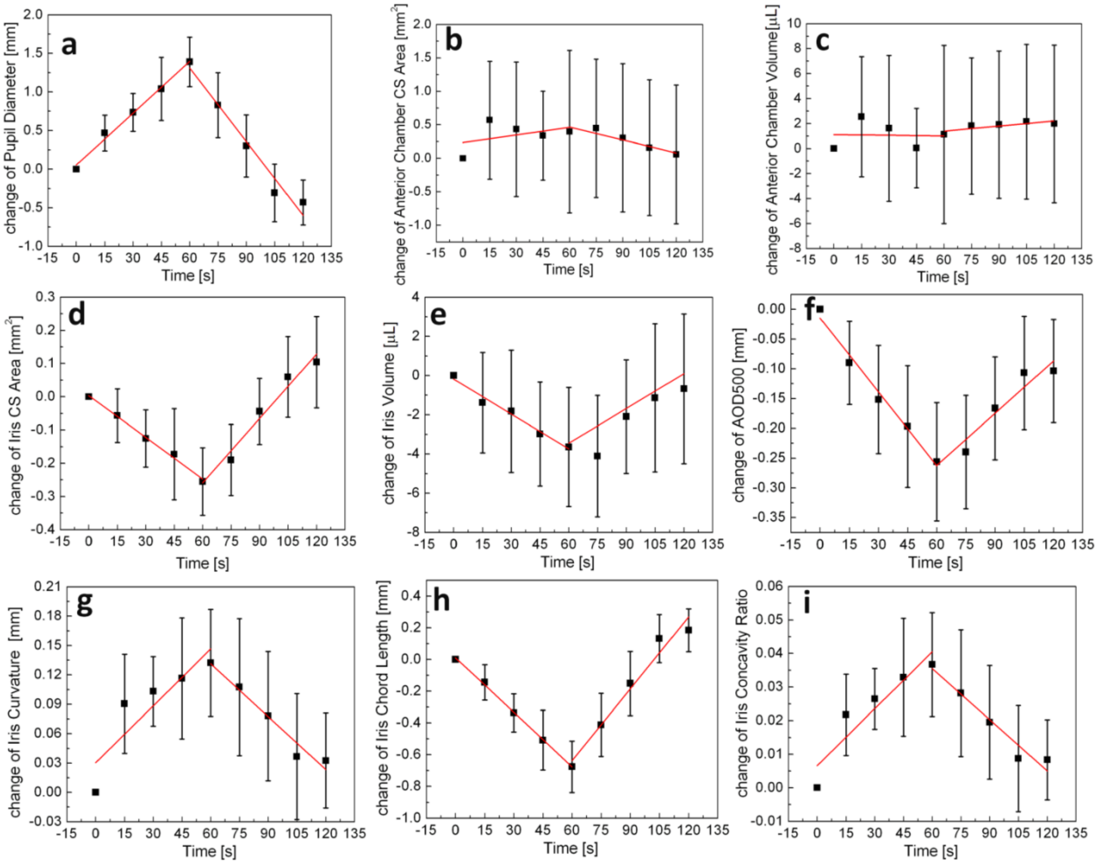

Figure 3-4 Linear regression analysis showing the change of measured variable from the initial (t=0 sec) case for dilation (t = 0-60 sec) and constriction (t = 60-120 sec). During dilation, the pupil diameter (a) increase significantly, the AC cross-sectional area (b), and the AC volume (c) do not significantly changed. The iris cross-sectional area (d) and the iris volume (e), the AOD500 (f), and the chord length (h) decreased. The curvature (g) increased, and the concavity ratio (i) increased. The reverse occurred for all measures during constriction (bars are 95% confidence interval, n = 20).

The measurements that exhibited a significant change with dilation/constriction in Figure 3-4 were further examined by plotting each variable vs. pupil diameter for both dilation and constriction (Figure 3-5). Figure 3-5a shows the AOD500 measurements and also how the hysteresis area and pupil range were defined. As can be seen from the average data of Figure 3-5, the AOD500 (Figure 3-5a) was higher during dilation than constriction. The iris cross-sectional area showed very little hysteresis (Figure 3-5b), but the iris volume was higher during dilation (Figure 3-5c). The iris curvature (Figure 3-5d) showed a difference for small pupil diameters but was largely independent of constriction-dilation direction for large pupil diameters. When the curvature was divided by chord length (Figure 3-5e), the resulting concavity ratio (Figure 3-5f) showed similar behavior – little difference between constriction and dilation for the large pupil diameters, but a divergence between the two curves for small pupil diameter.

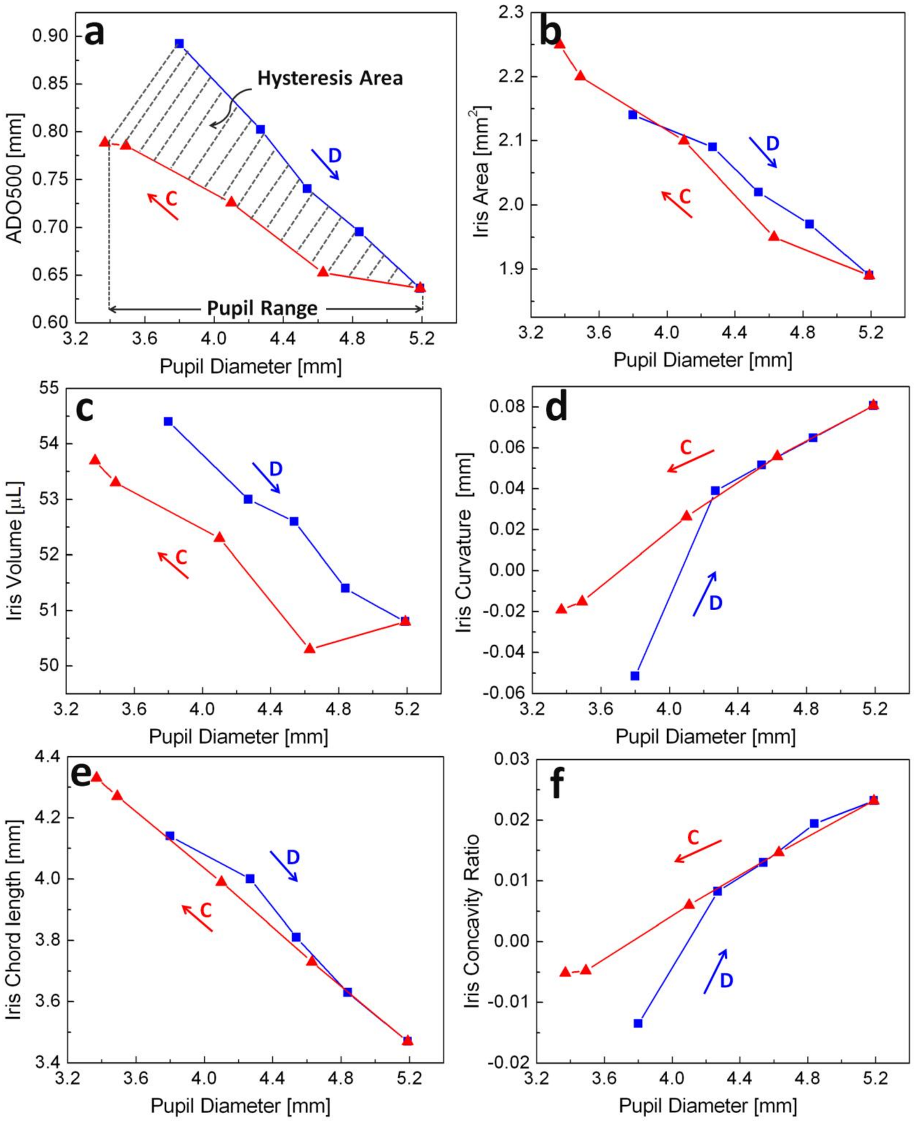

Figure 3-5 The relationship between mean of measured values for (a) AOD500, (b) iris area, (c) iris volume, (d) curvature, (e) chord length, and (f) concavity ratio as function of pupil diameter size (mean, n = 20). Dynamic dilation (D) and constriction (C) are shown in blue and red arrows, respectively. Typical hysteresis area and pupil range measurements (for AOD500) are demonstrated in (a).

Table 3-2 Hysteresis area for measured values (mean ± 95% CI, n = 20), and *p*-value

Parameter	**Average Hysteresis Area (Mean ± 95% CI)**	*p*-value
Iris Area (mm^2)	0.013 ± 0.038	0.62
Iris Volume (µL)	0.12 ± 0.039	0.30
Iris Curvature (mm)	-0.010 ± 0.038	0.34
Iris Chord length(mm)	0.008 ± 0.042	0.58
Concavity ratio	-0.003 ± 0.010	0.32
AOD500(mm)	0.033 ± 0.0363	0.08

The hysteresis area was also calculated for each individual patient, and the summary data are presented in Table 3-2. There was no significant hysteresis at the 95% confidence level ($p > 0.05$ for all quantities), but the AOD500 showed a trend, ($p = 0.08$) that should be investigated, as will be addressed further in the Discussion section. There was no significant hysteresis in iris area, volume, and curvature between dilation and constriction.

The changes in the measured parameters during dilation and constriction were also investigated by comparing all measured values in initial and final images. The lighting conditions in initial and final images were the same (lamp at 100 W in both cases), but the pupil diameter and AOD500 decreased significantly by an average of 11.32% ($p < 0.01$) and 11.63% ($p < 0.05$), respectively, from before dilation to after constriction, while the iris chord length increased by an average of 4.44% ($p < 0.05$). Other parameters did not change significantly between the two full-light conditions.

3.5 Discussion

Before discussing the results of this study in the larger context, we compare them to the recent work of Cheung et al. [43], who examined dynamic changes in iris contour following an abrupt change in light level from dark to light. They broke the response down into three groups: concave-concave (iris remained concave in light and dark), convex-convex (iris remained convex in light and dark), and concave-convex (iris was concave in light but convex in dark). Comparing our results to Cheung's results for subjects with open angle (Figure 3-6), we see that our data fell into similar groups. Cheung's experiments showed a higher fraction of subjects in the convex-convex group than ours. We suspect that this is due to the younger age of our subjects (32.7 years old vs. 52.4 for Cheung's open-angle subjects), particularly given the correlation of convexity with age [43, 54].

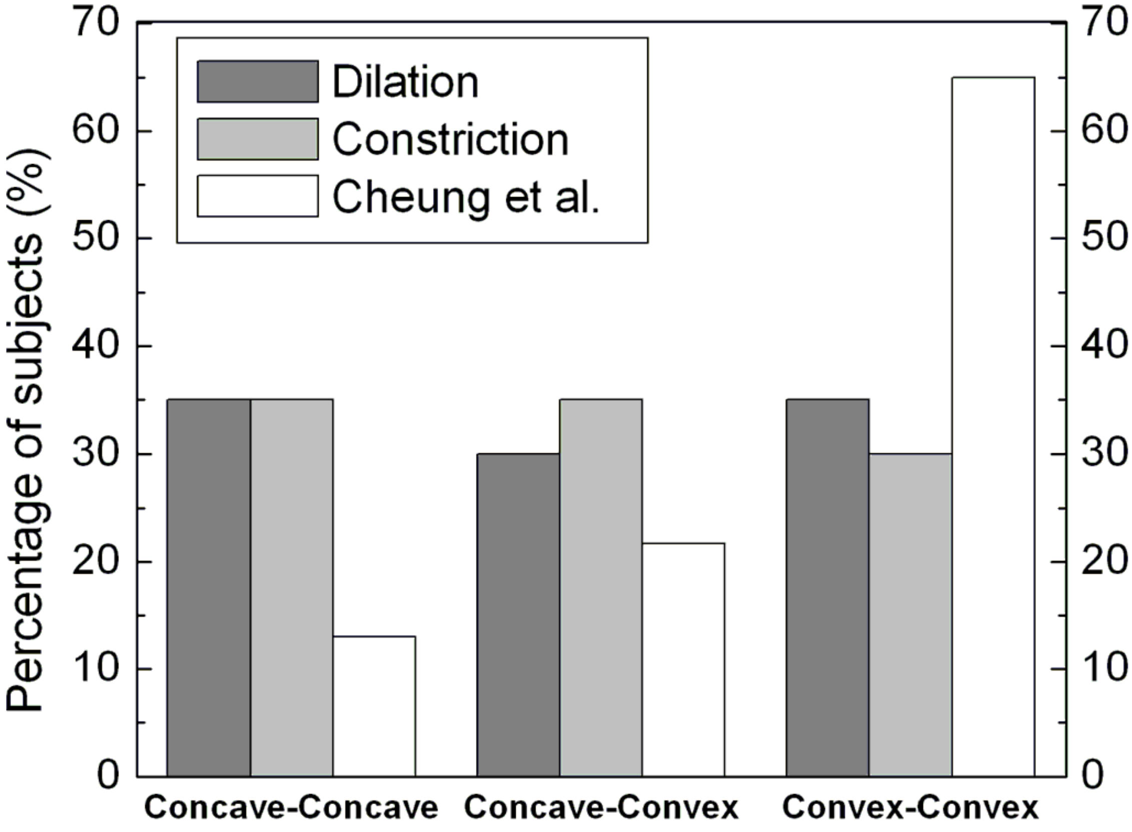

Figure 3-6 The distribution of subjects expressed in percentage (%). Three different dynamic patterns of iris configuration during dilation, and constriction, and comparison with the data of Cheung et al. [43].

There was a significant difference between the pupil diameters in the initial and final images. At the initial and final pupil diameter, the intensity of light is the same, but this difference could be explained by the dark-adaptation of the retina. The pupil could have been more sensitive at the end of the experiment, causing a smaller pupil.

Although LPI is a common and effective treatment for ACG, several case studies have reported residual angle closure [35, 36, 55], and the mechanism by which the angle narrows during dilation remains poorly understood. The different theories regarding dilation-induced angle narrowing are discussed in subsequent paragraphs in the context of our results.

Quigley and others [16, 44, 45] have put forward the idea that the iris loses water volume in normal individuals during dilation but not in ACG patients, suggesting that the reduced ability to change iris volume during dilation forces the iris into the angle. The current study, which involved only normal subjects, obviously cannot address the differences between normal and ACG patients. Nevertheless, we observed a small but significant decrease in iris volume during dilation and a corresponding increase during constriction, which was consistent with previous studies. Although the hysteresis area was not significantly different from zero, there was a slight overshoot in the iris volume, with the volume continuing to decrease during the first constriction step even though the pupil diameter was decreasing. This overshoot was not seen in the AOD500 measurements. The lack of significant difference in iris volume between dilation and constriction suggests that, for the normal subjects studied, fluid can move easily out of and into the iris because any practically significant resistance would have resulted in a volume hysteresis.

Huang and Barocas [39] proposed the idea of *dynamic* pupillary block, in which the motion of the iris changes the equilibrium volumes of the anterior and posterior chambers, but the pupil remains blocked, forcing anterior bowing of the iris to accommodate AH trapped in the posterior chamber. Dynamic pupillary block would suggest that the iris curvature would exhibit significant hysteresis if the experiment were performed on a time scale that allowed some but not all of the aqueous to leak through the pupil. The lack of hysteresis in our study has three reasonable explanations: (1) dynamic pupillary block is not an important effect (in normal or angle closure patients), (2) dynamic pupillary block is not an important effect in normal subjects but is important in angle glaucoma patients, or (3) the time scale of the experiment was too short for the dynamic pupillary block effect to be relieved, which would be necessary to create the hysteresis. Further studies, clearly needed to distinguish among these explanations, are now possible based on success of the current study. Stability of AC volume (Figure 3-3c), combined with our previous observation that PC volume is stable during dilation, suggesting that there is a minimal flow between AC and PC during dilation and consistent with dynamic pupillary block concepts.

We have also [50] suggested that the posterior placement of the dilator muscle within the iris contributes to the anterior bowing that occurs during dilation. This mechanism, which could work synergistically with either or both of those identified above, would be expected to be reversible without hysteresis and thus is consistent with all of our observations.

The hysteresis in AOD500, although not significant at the 95% confidence level, yielded a low enough *p*-value to suggest that a larger study, perhaps in combination with a study on narrow-angle subjects for comparison, could yield a significant effect. If the hysteresis were to prove significant, it would raise the question of how the angle can exhibit significant differences between dilation and constriction when the iris curvature and the iris volume do not. That is, one must ask what is different in dilation vs. constriction that affects AOD500 more pronouncedly than it does the other geometric parameters, or whether it is simply a matter that the other quantities have more variation, making hysteresis difficult to measure with available technology.

It is interesting to note that *both* pupil diameter and AOD500 decreased over course of the experiment. That is, at the end of the experiment, even though the light level was as at the start, the pupil was more constricted, and the angle was narrower. Even that the angle tends to narrow with dilation and open with constriction (Figure 3-4a, 2.4c, 2.4f), the start-to-end results are counterintuitive and suggest a dynamic effect.

Chapter 4 Contribution of Different Anatomical and Physiological Factors to the Iris Contour and Anterior Chamber Angle Changes during Pupil Dilation: Theoretical Analysis

(This work was part of the paper “Contribution of Different Anatomical and Physiological Factors to Iris Contour and Anterior Chamber Angle Changes during Pupil Dilation: Theoretical Analysis” by Sara Jouzdani, Rouzbeh Amini, and Victor H. Barocas, Invest Ophthalmol Vis Sci 2012, Submitted)

4.1 Summary

In this study we investigated the contribution of three anatomical and physiological factors (dilator thickness, dynamic pupillary block, and iris compressibility) to changes in iris configuration and anterior chamber angle (ACA) during pupil dilation. A mathematical model of the anterior segment based on the average values of ocular dimensions was developed to simulate pupil dilation. To change the pupil diameter from 3.0 mm to 5.4 mm in 10 seconds, active dilator contraction was applied by imposing stress in the dilator region. Three sets of parameters were compared in the simulations: (1) a THIN (4 μm, 1% of full thickness) vs. a THICK dilator (covering the full thickness iris) to quantify the effects of dilator anatomy, and (2) in the presence (+PB) vs. absence of pupillary block (-PB) to quantify the effect of dynamic motion of aqueous humor (AH) from the posterior to the anterior chamber, and (3) a

COMPRESSIBLE vs. an INCOMPRESSIBLE iris to quantify the effects of iris volume change. Changes in the apparent iris-lens contact and angle opening distance (AOD500) were calculated for each case. The THIN case predicted a large increase (average 700%) in iris curvature compared to the THICK case (average 70%), showing that the anatomy of dilator plays an important role in iris deformation during dilation. In the presence of pupillary block, AOD500 decreased 25% and 36% for the COMPRESSIBLE and INCOMPRESSIBLE iris, respectively. Iris bowing during dilation was driven primarily by posterior location of the dilator muscle and by dynamic pupillary block, but pupillary block did not have as large an effect on angle closure as measured by AOD500. Incompressibility of the iris, in contrast, had a relatively small effect on iris curvature but a large effect on AOD500. Thus, we conclude that all three effects are important.

4.2 Introduction

Angle closure is well documented to be more severe in dilation [23, 56]. Three potential causes for dilation-induced angle closure, all meriting further consideration, are the following: posterior location of the dilator muscle, (dynamic) pupillary block, and iris volume change (or lack thereof). These three physiological effects are reviewed in the subsequent paragraphs.

The dilator muscle’s anatomical location and thickness affect iris configuration during dilation. In human eyes, the dilator is located on the posterior surface of the iris with a thickness of 4-8 μm [4, 14]. Amini et al. [50] have recently shown that the posterior location of the dilator muscle can result in anterior bowing of the iris during dilation by a process independent of the AH dynamic pressure change. Contraction of the dilator muscle, located in the extreme posterior of the iris, tends to curl the iris and bow it to the anterior, consequently narrowing the angle.

Mapstone [57] theorized that pupillary block arises when the resultant of the two iris internal forces, namely muscle contraction and material stretch, produces a net force acting towards the lens surface and blocking the pupil. Pupillary block has generally been invoked in association with the steady flow of the AH through the pupil [58-60]. Huang and Barocas [39], however, showed that steady-state pupillary block is inconsistent with increased angle closure during dilation. Thus, one may naturally postulate that dilation-induced pupillary block is rather a transient phenomenon. In particular, iris motion during dilation may pressurize the AH in the posterior chamber and subsequently drive AH from the posterior to anterior chamber. If, however, internal forces (due to active contraction and tissue stretch) pin the iris tip against the lens surface and obstruct AH flow at the iris-lens gap, the pressure in the posterior chamber will rise and bow the iris to the anterior. We refer to this phenomenon as “dynamic pupillary block.” In other words, dynamic motion of the iris provides a more reasonable mechanism by which dilation could induce bowing than does the *static* pupillary block mechanism.

The iris volume change during dilation is another physiological factor that may contribute to angle closure. Quigley et al. [16] observed a significant dynamic change in the iris volume of normal subjects during dilation but not in patients suffering from angle-closure. They proposed the idea of iris relative incompressibility in angle closure glaucoma (ACG) patients. Aptel et al. [44] reported similar results for open angle glaucoma (OAG), the control group, and ACG patients. Quigley et al. [16] have argued eloquently that ACG patients have less tendency to lose iris volume due to relative iris incompressibility compared to the normal subjects. Lack of significant changes in the iris volume would cause crowding of the peripheral iris into the iris root and narrowing of the anterior chamber angle (ACA).

Thus, we considered three distinctive factors as possible contributors to the narrowing of the angle during dilation:

(1) Posterior location of the dilator muscle.

(2) Dynamic pupillary block and trapping of AH in the posterior chamber.

(3) Exudation/imbibition of AH by the iris stroma observed as relative incompressibility of the iris during dilation.

Each of these effects can be important, and their relative roles may vary among individuals. Because all three effects occur in every patient, it would be difficult, if not impossible, to study them in isolation via experiment. Computer simulation, in contrast, can be used to eliminate one or more factors, allowing us to assess the role of each factor independently and to quantify any positive or negative interaction among the various effects. The goal of this work was to determine, via a computational model, how each of the three factors listed above, in isolation as well as in conjunction with one or both other factors, contributes to angle closure.

4.3 Methodology

Our previous axisymmetric computational model of the anterior segment [38, 39, 48, 49, 61] was modified to simulate pupil dilation. The model domain representing the anterior segment was divided into the AH and iris as shown in Figure 4-1. The governing Equations of each component are presented in the following sections. As shown in Figure 4-1, the rest state of the iris was assumed to be planar with 3.0 mm pupil diameter. Geometric and mechanical parameters used in model development were based on published data (Table 4-1).

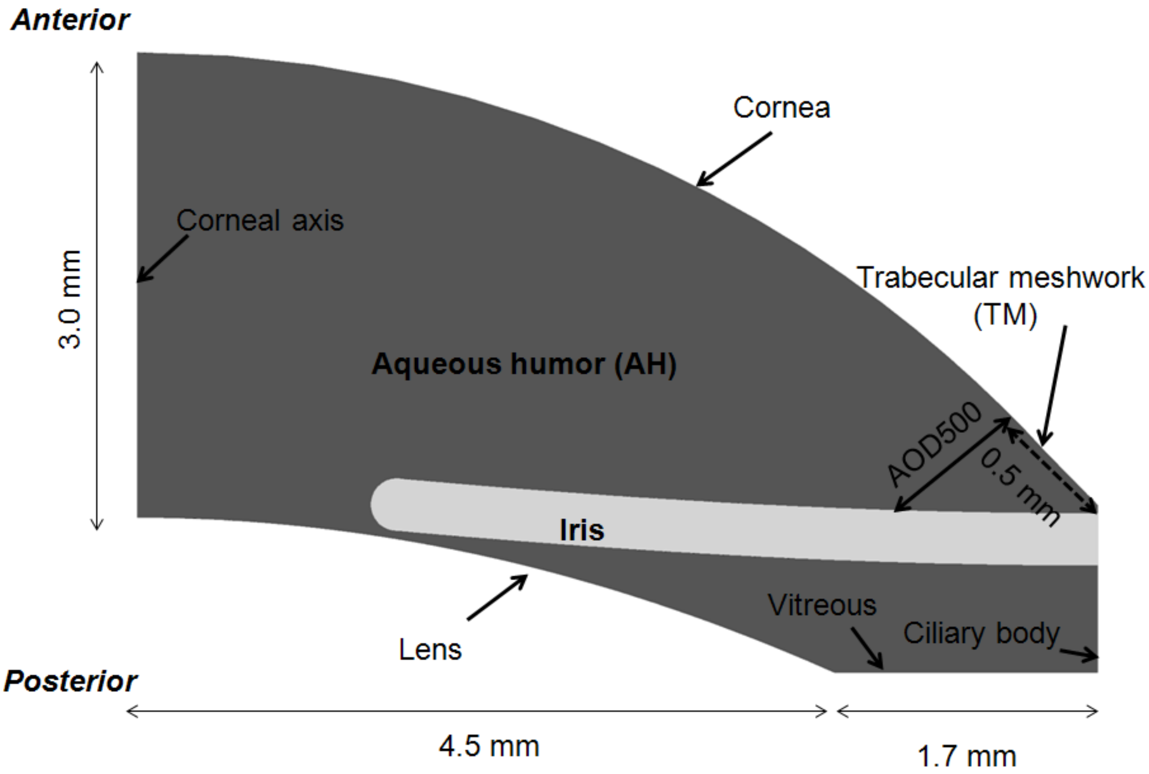

Figure 4-1. Axisymmetric model of the anterior segment showing the AH (light grey) and iris (dark grey) as well as, the boundaries and dimensions of the model.

Table 4-1 Geometric parameters and mechanical properties of the tissues in the model.

Parameter(average value)	**Value (and Reference)**
Cornea radius of curvature	7.8 mm [5]
Iris thickness	0.34 mm [62]
Anterior chamber diameter	12.37 mm [63]
Anterior lens curvature	10.29 mm [64]
Lens diameter	9.0 mm [65]
Iris-zonule distance	0.69 mm [62]
Modules of elasticity of the iris	27 kPa [66]

The finite-element (FE) meshes were generated using GAMBIT (Fluent Inc., Lebanon, NH) via the paving technique. The Galerkin FE method was employed to solve the mathematical equations, as described previously [49]. The pressure difference between the posterior and anterior chambers, ΔP, AOD500, and apparent contact length were calculated during simulated dilation. The apparent iris-lens contact was defined by the distance over which the iris was within 500 µm from the lens. AOD500 was defined as the perpendicular distance from the trabecular meshwork to the iris surface at a point 500 µm from iris root (Figure 4-1).

4.3.1 Model domains and equations

The two physical domains of the axisymmetric model were the AH and the iris.

4.3.1.1 Iris

The iris was considered a neo-Hookean solid described by Cauchy momentum equation

4-1

where is the Cauchy stress , which for a neo-Hookean material is defined by the following equation:

$$- \qquad \overline{\qquad\qquad}$$ 4-2

where ν is the Poisson's ratio, G is the shear modulus, and is the identity matrix. The deformation gradient is defined by

$$\overline{\quad}$$ 4-3

4-4

with **x** being the current position of a material point, **X** being its rest position. The gradient and divergence operators were with respect to current coordinates.

In Equation 4-2, the iris is modeled as a passive tissue. However, the activation of the two constituent muscles of the iris could affect the biomechanical parameters of the iris and AH flow. The iris consists of three main components: the stroma, sphincter iridis muscle, and *dilator pupillae* muscle. The stroma is a collagenous connective tissue whose loose nature allows AH exudation/imbibition during dilation and contraction. The activation of the two constituent muscles of the iris, the *sphincter iridis* and the *dilator pupillae,* controls the iris motion. Fibers of the *dilator pupillae* are aligned radially on the posterior iris surface and the sphincter muscle is located circumferentially near pupillary margin.

4.3.1.2 Dilator (simulation dilation)

Human pupil diameter can vary between 1.0 mm at maximum constriction and 9.0 mm maximum dilation, respectively [12]. In this study we are simulating dilation. Since the exact contribution of the individual muscles to dilation is not clear, a simplified iris was modeled with two components: an active component i.e. dilator and a passive component i.e. stroma. The dilator was localized on the posterior surface of the iris and the stroma was created on the anterior side of the iris. Pupil dilation over time (Figure 4-2) was simulated by imposing an additional stress on top of the neo-Hookean stress along the dilator in the radial direction as defined by the following equations:

4-5

4-6

where and represent the stress of the dilator and stroma, respectively and were replaced in Cauchy momentum equation (Equation 4-1). is the unit vector representing the direction of non-deformed dilator muscle (i.e. radial direction), and the symbol represents dyadic product. is a scalar stress acting on dilator muscle in radial direction to dilate the iris. Although added one degree of freedom to the model, the magnitude of determined in such way that variation of pupil diameter over time was similar to the reported clinical studies [67]. Based on Crawford's work, pupil diameters changed from 3.0 mm to 5.4 mm during 10 seconds. The rest state of the iris was assumed to be planer with 3.0 mm pupil diameter.

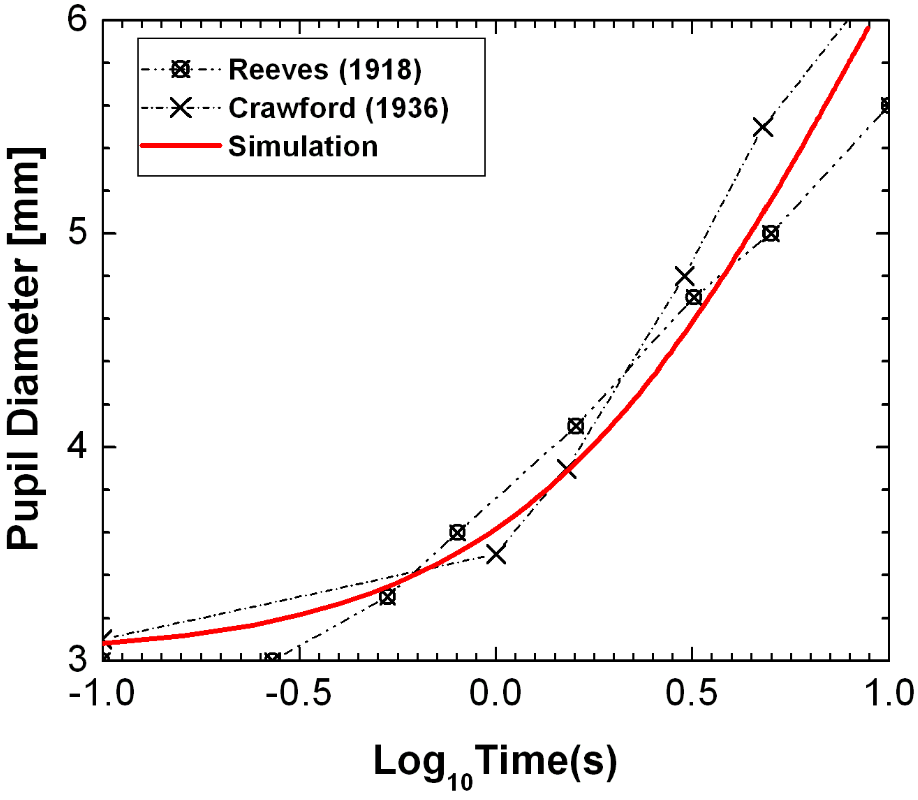

Figure 4-2 Pupil diameter vs. time during dark adaptation. In dilation simulations, the variation of pupil diameter over time was consistent with published clinical data. [67, 68]

4.3.1.3 Aqueous humor

The AH was modeled as an incompressible Newtonian fluid described by the full Navier-Stokes equations for the momentum and continuity equations:

4-7

— 4-8

4-9

where is velocity, is stress tensor, is pressure, is density, is viscosity, and is identity matrix. AH has a density, , of 1000 kg m^{-3} [69] and a viscosity, , of 7.5 10^{-4} kg m^{-1} s^{-1} at 37ºC

4.3.1.4 Aqueous humor: pseudo-solid domain

In order to determine the displacement of the fluid domain, a pseudo-solid method was used [70]. In this method, the fluid mesh was represented as a linear elastic solid using the following governing equations:

4-10

4-11

where and are Lamé coefficients. The displacement from the rest position, , and the Eulerian strain tensor, , are defined by:

4-12

– 4-13

Divergence and the gradient are with respect to the current coordinates.

4.3.2 Boundary conditions

The boundary conditions of the governing equations of the system are discussed in the following sections.

4.3.2.1 Corneal Axis

The eye is assumed to be symmetric about the axis perpendicular to the lens (corneal axis). The boundary condition on the corneal axis is imposed so that the velocity normal to the axis of symmetry, , and the derivative of the axial velocity, , with respect to the radial direction are zero.

4-14

—— 4-15

4.3.2.2 Lens

The lens is modeled as a rigid solid surface, and the no-slip condition dictates that the velocity of the AH be zero.

4-16

The lens capsule is quite stiff ($E \approx 20$ MPa [71]) and the position and contour of the lens are generally controlled actively, so we treat the lens as uninfluenced by AH dynamics and prescribe its position and movement, depending in the nature of problem [see chapter 5].

4.3.2.3 Vitreous

The vitreous surface was also treated as a fixed rigid boundary in the pseudo-solid domain. Therefore, the no-slip condition dictates that the velocity of the AH be zero:

4-17

Moreover, a free normal traction condition of the vitreous surface was implied. Since the rate of AH flow inflow and outflow was constant, vitreous inflow/outflow would make up for any changes in the domain volume:

4-18

4.3.2.4 Cornea

The cornea was modeled as a rigid boundary in the pseudo-solid domain. Also, the no-slip boundary condition was imposed on the corneal surface:

4-19

4-20

4.3.2.5 Trabecular meshwork and Ciliary body

Similar to the cornea, the trabecular meshwork and the ciliary body were modeled as rigid surfaces in the pseudo-solid domain:

4-21

The AH flow is secreted from the ciliary body and mostly exits through the trabecular meshwork. The rate of AH secretion is largely independent of IOP [72] and is about [73-75]. For the inflow (ciliary body) and the outflow (the trabecular meshwork), a parabolic velocity strongly was imposed to satisfy the following equation

4-22

4.3.2.6 Iris-aqueous interface

On the iris-aqueous interface, the velocity of the iris and the AH were required to be equal in order to satisfy the no-slip boundary condition. Shear stress generated by AH flow deformed the interface of the iris-AH. The displacement of the iris was calculated by setting the viscous traction in the fluid equal to the elastic traction exerted by the iris at the iris-AH interface Therefore, the traction in the fluid was set equal to the traction on the solid surface:

4-23

The aqueous velocity on the iris-aqueous interface surface was enforced strongly to be equal to the velocity of the iris at the boundary.

— 4-24

Based on clinical obstructions, the iris volume may decrease during dilation as extracellular fluid moves out from the iris, particularly the stroma section. This hypothesis was examined by modeling the iris as compressible material, e.g. $\nu = 0.3$ (Equation 4-2). The extracellular fluid probably moves out mostly from the anterior side of the iris (the stroma) into the anterior chamber. The volumetric flow rate was modeled as change of the iris volume at the two consequent time steps.

4-25

The volumetric flow rate, , can also be calculated via the following equations:

4-26

4-27

where is a unit vector normal to the iris surface at the each node along the iris-aqueous interface and and are area and volume element, respectively. Using the implicit Euler method, the temporal derivatives were approximated by a first-order difference between the values of function at the two consequent time steps, the iris velocity, , was defined by the following equation

4-28

where “ ” and “ ” are the nodal and temporal indices, respectively.

It is likely that the fluid exudates into the anterior chamber from the anterior surface of the iris. Therefore, the average extracellular fluid velocity, , is defined by:

4-29

where is the area of upper surface of the iris (Figure 4-3). The average extracellular fluid velocity was applied at the iris-aqueous interface. Since the curvature of the iris is dependent on time during the pupil dilation, under the assumption that the velocity moves out from the iris uniformly, the aqueous velocity (Equation 4-24) was modified to

— 4-30

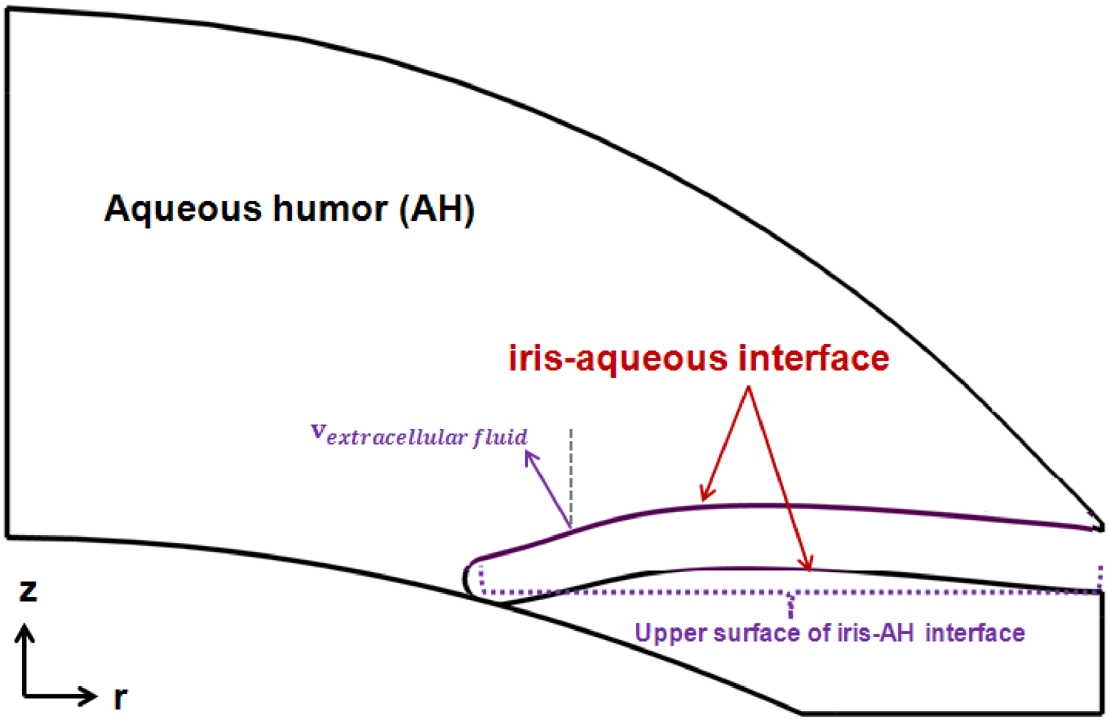

Figure 4-3 The extracellular fluid was added to the iris-aqueous interface to account for iris volume change during dilation.

4.3.3 Contact between Iris and Other Tissue

The iris thickness, particularly near of its root, increases as the dilation progresses. As the iris bows more anteriorly during dilation, the iris root region nearly comes into contact with the trabecular meshwork (TM). Similar behavior occurs at the pupillary margin as the iris tip approaches the anterior lens surface [48]. Actual contact between two smooth surfaces is theatrically impossible due to lubricating AH flow at the contact region. In the numerical procedure, however, the overlap of the two surfaces can occur and lead to failure of the simulation. In order to prevent iris-TM and iris-lens overlap, artificial stresses were introduced on the iris nodes to enforce a no-contact zone between the iris and lens (or TM) [48]

$$— \qquad 4\text{-}31$$

with being the vector normal to the lens or TM surface at the nearest point to the surface, A and being adjustable coefficients, and being the minimum distance from the iris to the lens or TM. The coefficient corresponded to how far the no-contact zone extended into the AH, and the coefficient A corresponded to how strongly the no-contact zone was enforced. The effect of the contact-prevention force between the lens and iris on apparent contact was examined previously [48]. Based on Heys' work [48], the values of and A_{lens} used in all +PB studies were 0.4 µm and 5 10^{10} Pa, respectively, to prevent overlap between the iris and the lens. -PB was modeled by applying a higher artificial stress on the iris normal to the lens by using = 4.0 µm in Equation 4-31.

The contact-prevention force depends on the distance along the iris over which the force is applied. Figure 4-4 shows the effect of that distance on AOD500. As shown in Figure 4-4, if the contact-prevention force was applied over a longer distance, it had a significant impact on the active iris displacement, and AOD500. In all simulations, and A_{TM} were set in such way that they had the minimal effect on the outcome. Based on the data in Figure 4-4, the maximum values of and A_{TM} used in all studies were 16 μm and 5 10^{10} Pa, respectively.

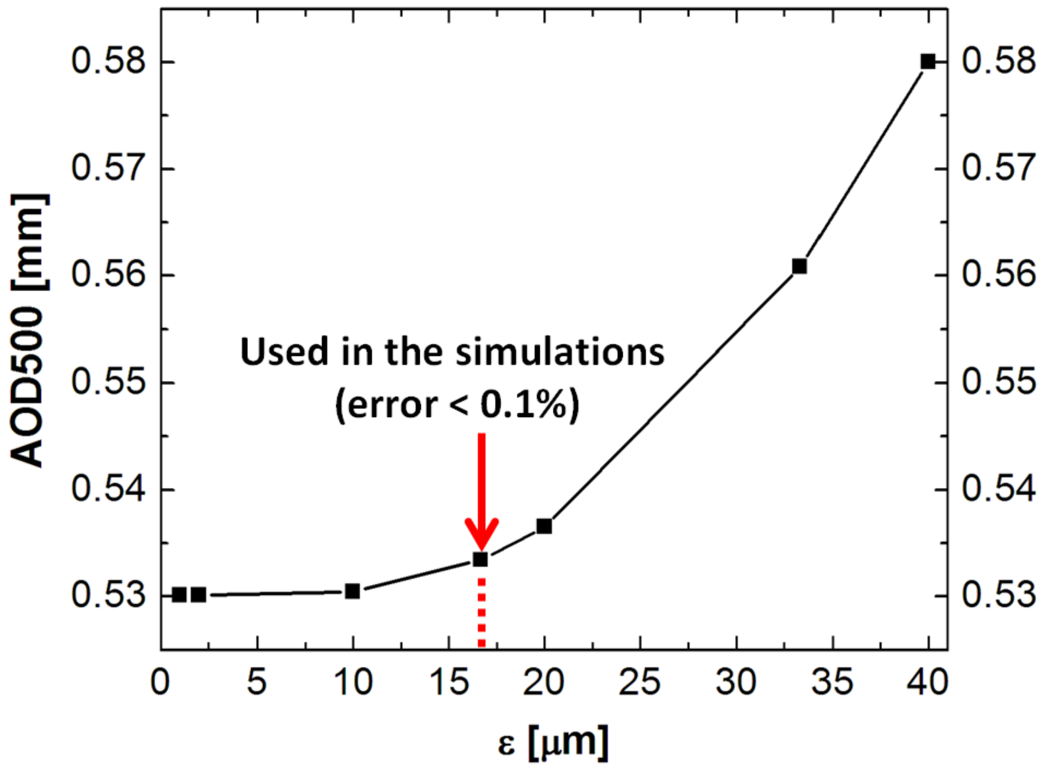

Figure 4-4 The effect of the contact-prevention force between the TM and iris on AOD500. A significant impact on the active iris displacement was observed, when the contact-prevention forces were applied over a longer distance.

4.3.4 Aqueous (fluid) domain remeshing

A major computational challenge was remeshing the FE domain as the pupil diameter increased. As the iris dilated, elements along the iris-lens gap distorted. In order to minimize this distortion, the FE nodes were allowed to slide along the lens. The sliding method of nodes on lens surface following the iris node was explained in detail in Dr. Rouzbeh Amini's dissertation [76]. However, as the pupil diameter continued to increase, much larger deformations arose, particularly near the pupil margin, that led to divergence of the solution. In order to maintain convergence of the solution and prevent extreme element distortion, the simulation was stopped at a certain time where the solution was acceptable, and the domain was remeshed. It was sufficient to remesh only the fluid domain. The iris-aqueous interface velocity field was imposed on the new AH mesh and the steady state for the new AH domain was determined assuming the iris domain was fixed and the velocity field for all the nodes of the new AH mesh were obtained. The iris solution from the stop point and the new steady state solution for the new AH domain were then used to simulate the continued of dilation and the subsequent increase in the pupil diameter.

The deformation gradient should be always with **x** being the current position of a material point, and **X** being its rest position. However, for simplicity, we used the chain rule of differentiation:

$$\frac{}{} \qquad \frac{}{}\,\frac{}{} \tag{4-32}$$

with **x** being the current position of a material point, **X** being its rest position, and being the position of a material point at stop point (Figure 4-5).

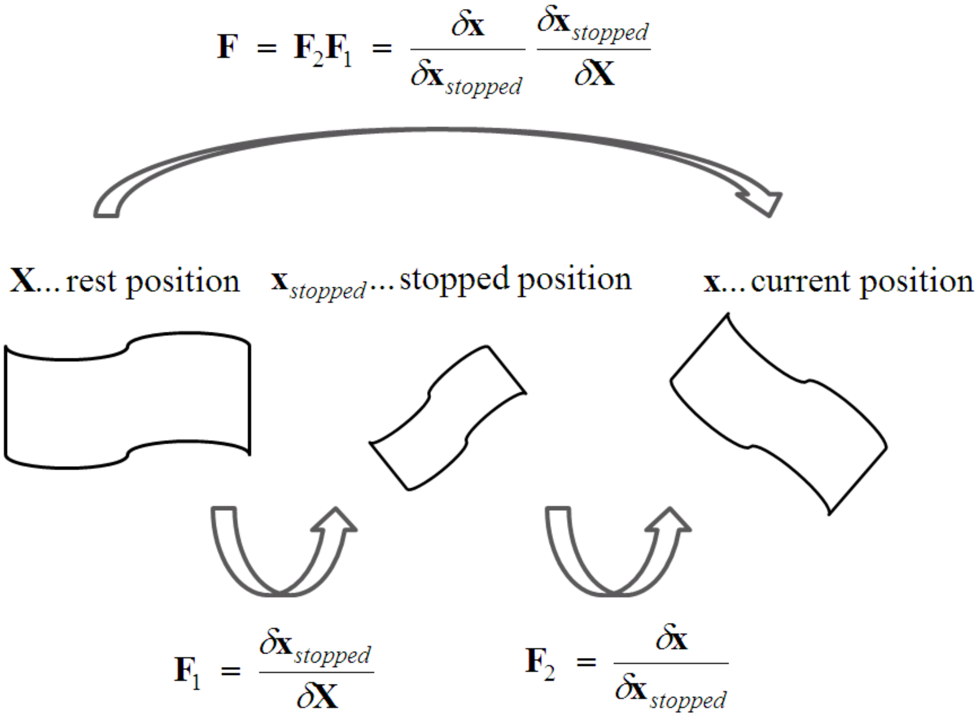

Figure 4-5. Motion of a body with respect to two different reference configurations.

4.3.5 Study design and implementation

Study Design and Implementation

In order to investigate the effects of three factors - dilator thickness, dynamic pupillary block, and iris compressibility - on the iris contour and AOD500 changes during dilation, a full factorial study was undertaken changing three parameters:

(1) Posterior location of the dilator muscle by modeling <u>Thin</u> vs. <u>Thick</u> dilator region

Two cases were considered. For the THIN dilator case, the dilator was modeled as a 4 µm thick layer along the posterior iris. For the THICK dilator case, the dilator occupied the entire iris thickness.

(2) Pupillary Block vs. no Pupillary Block

+PB arises naturally from the fluid-structure interaction model. -PB was modeled by applying an artificial force acting on iris nodes in the direction normal to the lenticular surface at the iris-lens gap (See section 4.3.3).

(3) Incompressible vs. Compressible iris

For the COMPRESSIBLE iris case, the iris was modeled as a compressible neo-Hookean solid with Poisson's ratio $\nu = 0.3$, for the INCOMPRESSIBLE iris case, the iris was modeled as a nearly incompressible neo-Hookean solid with Poisson's ratio $\nu = 0.49$. In the compressible iris model, aqueous was assumed to flow out of the shrinking iris at a rate that preserved total anterior segment volume.

A total of eight simulations were performed to investigate the role of each factor independently and to quantify interaction among these three effects. In all simulations, the pupil diameter changed from 3.0 mm to 5.4 mm during 10 seconds (Figure 4-2).

4.4 Results

We begin by comparing briefly the anatomically realistic (THIN) dilator with the unrealistic THICK dilator. The THIN case produced a threefold to ninefold increase in iris curvature, depending on the other factors, whereas the THICK case produced at most a 70% increase in iris curvature, a result consistent with our previous finding [50] that the THIN dilator drives curvature of the iris during dilation. Perhaps more importantly, Figure 4-6 shows that the THICK dilator caused the iris to dilate in a pupil-blocking manner, so the elimination of pupillary block had no effect (+PB and -PB cases nearly identical in Figure 4-6a, 4.65b). Incompressibility of the iris led to a decrease in AOD500 for the THICK dilator case (Figure 4-6c, 4.6d), but because the result is much more pronounced in the THIN case, and the THIN case represents the correct anatomy, we present results only for the THIN case for the remainder of this section.

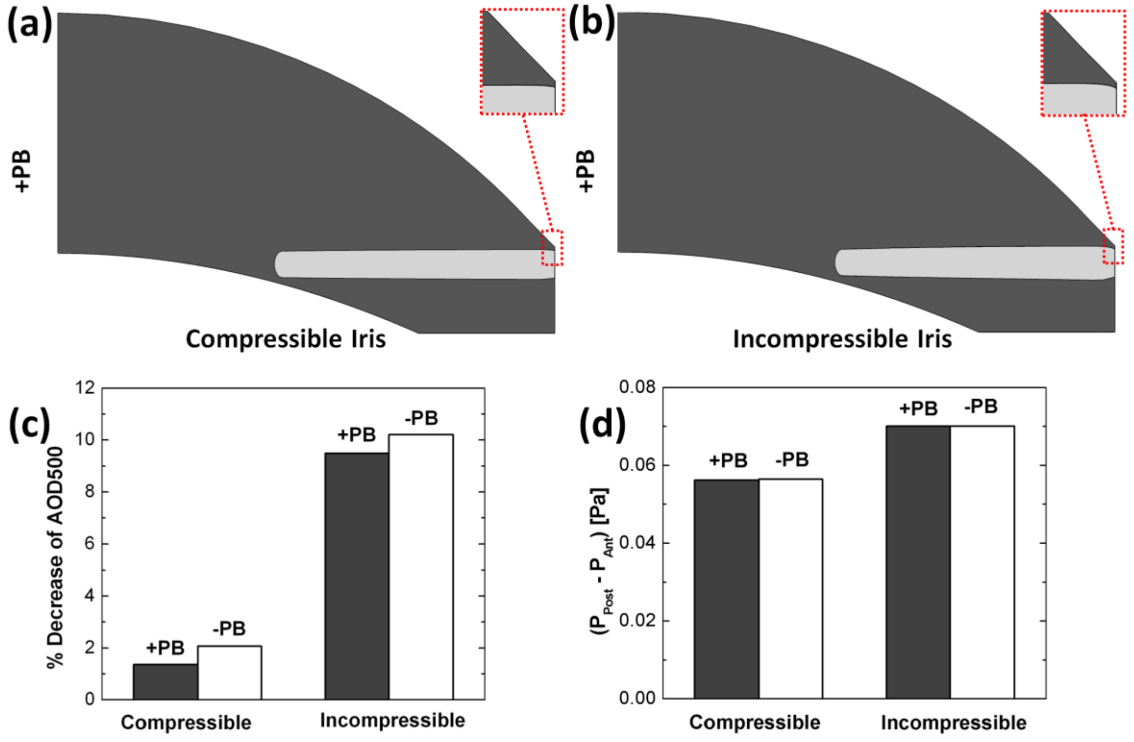

Figure 4-6 Mechanical response for two THICK cases: (a) COMPRESSIBLE and (b) INCOMPRESSIBLE iris in the presence of pupillary block. (c) % decrease of AOD500 and (d) pressure difference between the posterior and anterior chamber.

Figure 4-7 shows the iris contour for each of the four THIN cases (+/-PB, INCOMPRESSIBLE vs. COMPRESSIBLE). Two effects are clear. First, the presence of pupillary block causes the iris to bow forward more, narrowing the angle. Second, the incompressible iris bulges at the iris root as the dilator muscle contracts radially, pushing the iris stroma into the angle. The combination of the two effects is seen in the lower-left panel of Figure 4-7.

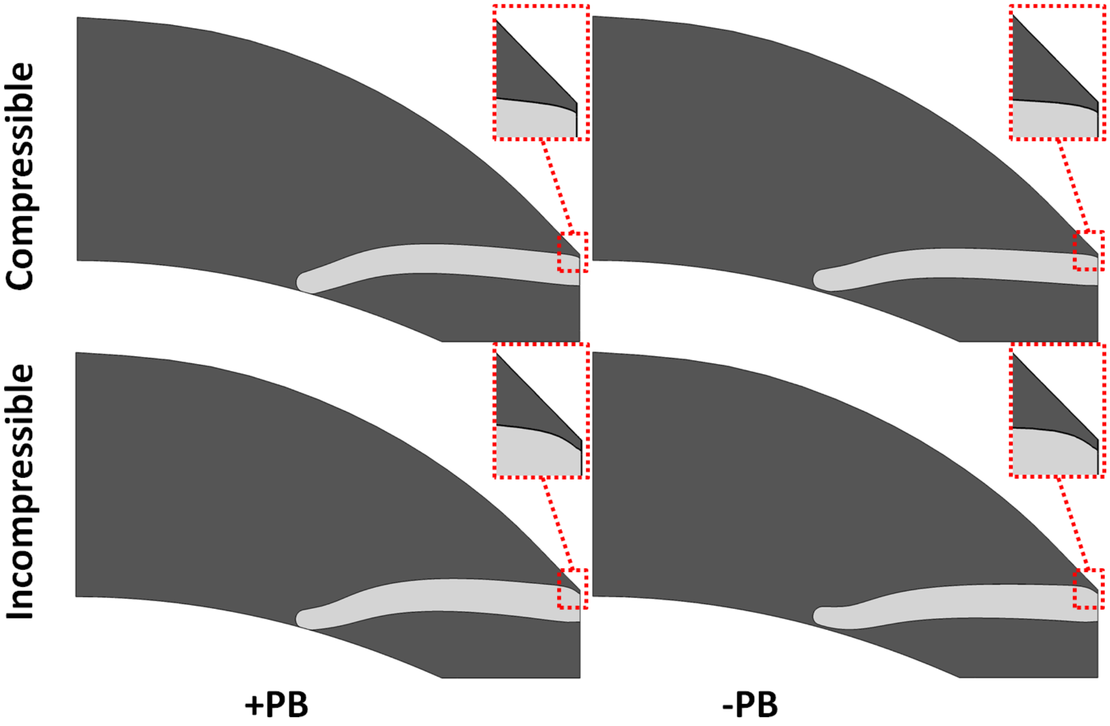

Figure 4-7 Changes in the iris profile and ACA for four THIN cases.

The results of Figure 4-7 are further quantified and analyzed in Figure 4-8. Examining the details of the iris contour (Figure 4-8a), it can be seen that the pupillary-block effect drives curvature of the iris, and that this effect is more pronounced in the case of a compressible iris. The curvature seen in the –PB cases is attributed to the thin iris since there is no significant pressure difference across the iris. The amount of iris-lens contact (Figure 4-8b, only the +PB case was considered since iris-lens contact was artificially eliminated in the –PB case) decreased slightly in the incompressible case. AOD500 decreased more (Figure 4-8c) in the presence of pupillary block and for the incompressible rather than the compressible iris. The combined effect of THIN dilator,

+PB, and INCOMPRESSIBLE was a 36% decrease in AOD500. Finally, the anterior bowing is explained by the substantial increase in posterior-anterior pressure drop in the +PB cases (Figure 4-8d).

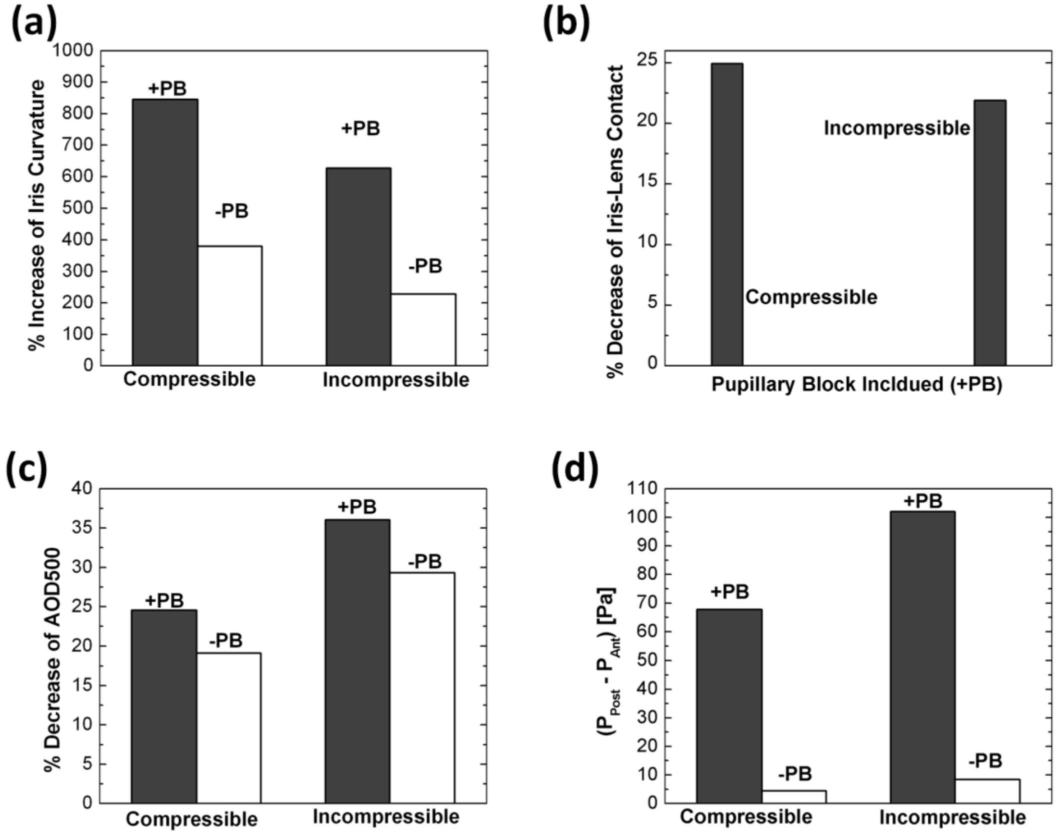

Figure 4-8 THIN cases. (a) % increase of iris curvature, (b) % decrease of iris-lens contact, (c) % decrease of AOD500, and (d) pressure difference between the posterior and anterior chamber.

Among all the cases, the least decrease in AOD500 and the pressure difference between posterior and anterior chambers, $\Delta P = P_{Posterior} - P_{Anterior}$, obtained in the case of THIN dilator, -PB, and COMPRESSIBLE iris. All of the other choices (THICK, INCOMPRESSIBLE and +PB, either singly or in combination) lead to greater decrease in AOD500, that is more severe angle closure.

In the COMPRESSIBLE case, the iris lost approximately 9% of its volume during the course of dilation. In the INCOMPRESSIBLE case, the volume loss was less than 1% (for a truly incompressible material, there would be no volume loss).

4.5 Discussion

As summarized in Table 4-2, computational models of the anterior segment have been developed previously to study phenomena such as miosis, blinking, reverse pupillary block, etc. To our knowledge, the present study was the first theoretical study to examine the idea of dynamic pupillary block during dilation and the role of iris incompressibility in angle closure.

Table 4-2 Comparison of the theoretical models of the anterior segment.

Investigator	**Methods**		**Other information**
	Aqueous Humor	**Iris (Incompressible)**	
Heys *et al.* 2001 [38]	Transient Stokes flow	Linear elastic, Passive	Mechanics of the healthy eye, iris constriction†, blinking, and iris bombé were studied.
Heys and Barocas 2002 [48]	Transient Stokes flow	Linear elastic, Passive	Accommodation in healthy eye and pigmentary glaucoma was studied. The lens was considered as a moving rigid boundary.
Huang and Barocas 2004 [39]	Steady-state Navier-Stokes flow	Nonlinear elastic, Active	Pupil constriction in the healthy eye and PCGA eye along with the PCGA anatomical risk factors were studied.
Huang and Barocas 2006 [77]	Transient Navier-Stokes flow	Nonlinear elastic, Passive	The accommodative micro fluctuations were studied. The lens was considered as a moving rigid boundary.
Amini and Barocas 2010 [49]	Transient Navier-Stokes flow	Nonlinear elastic, Passive	Corneoscleral indentation was modeled to study reverse pupillary block mechanism. The indentation was modeled by posterior rotation of the iris root
Amini *et al.* 2012 [50]	Excluded	Nonlinear elastic	Anterior bending of the iris during dilation was studied

The changes in iris configuration and ACA associated with change in pupil diameter have been examined in several clinical studies [23, 53] Concavity, shortening, and thickening of the iris [22] and consequently narrowing anterior chamber [78] during dilation suggest that dilation plays an important role in angle closure pathogenesis. More recently, dynamic changes and anatomical factors related to the iris have received more attention. The purpose of this study was to create a mathematical model to simulate the dynamic motion of the iris and ACA associated with change in pupil diameter. Specifically, we studied the effects of three anatomical factors – (1) the posterior location of the dilator, (2) dynamic pupillary block during dilation, and (3) iris relative compressibility.

All eight case studies showed that AOD500 decreased significantly during dilation, a result consistent with several clinical observations [43, 78]. Leung et al. [78] showed that the changes of AOD500 were significantly higher in eyes with narrow angles than in those with open-angle in response to dark-light changes. Quigley et al. [16] and See et al. [45] showed that the iris loses water volume in normal individuals during dilation but less volume in ACG patients, suggesting a relative incompressibility for ACG patients. Our results showed that the models with a compressible iris lost 9% of their volumes as pupil diameter changed from 3.0 mm to 5.4 mm during 10 seconds and had less change in AOD500 compared to models with incompressibility of the iris. The 9% volume change is smaller than the ~15% volume change determined via OCT by Aptel et al. [44] but was deemed sufficient to compare to the incompressible case. Finally, to provide a more clear presentation of the results, only the simulation predictions for $\nu = 0.3$ and $\nu = 0.49$ (explicitly referred as compressible and incompressible cases) have been included in this paper. Our studies of the intermediate values (results not presented) showed a smooth transition in AOD500 from $\nu = 0.3$ to 0.49.

When the entire thickness of the iris was simulated as the active tissue, the anterior bowing of the iris during dilation was insignificant. In the case of -PB, the presence of artificial force on the iris, prevented anterior bending of the iris and caused a slight angle-closing artifact. In the cases with a THICK dilator, less change in iris curvature and consequently less decrease in AOD500 were seen. A thin dilator on the posterior surface of the iris caused more bending of the iris and more decrease in AOD500, suggesting the importance of the anatomy of dilator during dilation. Amini et al. [50] also examined iris configuration changes during dilation in the absence of AH and showed a thin layer dilator on the posterior surface of the iris resulted in more anterior bowing of the iris. In the cases with a THIN dilator, the pupillary-block effect drives curvature of the iris whereas the compressibility effect drives the narrowing of AOD500.

Chapter 5 Interaction of Different Ocular Events Affects Iris Contour

5.1 Summary

In this study, we examined changes in iris configuration and anterior chamber angle during and after blinking, accommodation, and constriction using a mathematical model of the anterior segment. Geometric and mechanical parameters for the model were based on published data. Blinking was modeled by posteriorly rotating the iris root for 80 ms and returning it to original position in 200 ms every three seconds. Accommodation was modeled by moving the boundary of the lens surface anteriorly to change the anterior chamber depth by 0.2 mm. Pupil constriction was modeled by imposing a circumferential stress in the sphincter to reduce pupil diameter. The iris was modeled as a compressible or an incompressible neo-Hookean material to investigate the effect of relative compressibility of the tissue on the results. Accommodation and constriction were performed simultaneously after 10 s of blinking. Iris curvature and iris-lens contact were calculated. Before blinking, the iris was bowed slightly toward the posterior, and the pressure in the posterior chamber was slightly higher than that in the anterior chambers for both compressible and incompressible models. After blinking, there was little small change in iris curvature and iris-lens contact. As accommodation and pupil constriction constriction began, the pressure was elevated in the anterior chamber (reverse pupillary block), causing more pronounced posterior bowing of the iris. Immediately after

accommodation and constriction, iris-lens contact length and AOD500 increased by approximately 10 % and 23% (average values), respectively while the pressure drop across the iris decreased to ΔP = -35.0 Pa. Long after accommodation and constriction (300 s), the pressure in the posterior chamber again became higher than anterior chamber for both models (ΔP = +26.4 Pa). However, obtaining the same results in cases of simulating accommodation and constriction simultaneously and simulating accommodation and constriction sequentially indicates that the interaction between and accommodation and constriction is not synergistic. Clinical studies have shown that accommodation leads to posterior bowing of the iris, particularly in PDS patients who have flaccid and smaller iris. The combination of pupil constriction and accommodation produced significant posterior bowing of the iris. The effect was more pronounced when the iris was incompressible; suggesting that changes in iris volume could play a role in PDS [24] similar to that seen in angle closure [16].

5.2 Introduction

Accommodation is the process by which the focusing power of the eye is increased for seeing at near by changing the curvature of the lens. Pavlin et al. [47, 79] proposed the idea of posterior bowing of the iris as the lens moves during accommodation. Heys and Barocas [48] developed a detailed computational model of the anterior segment and examined the hydrodynamic effects of accommodation on the iris curvature. Consistent with UBM measurements [80], Heys and Barocas's model predicted that the curvature of the iris becomes more concave as a result of accommodation.

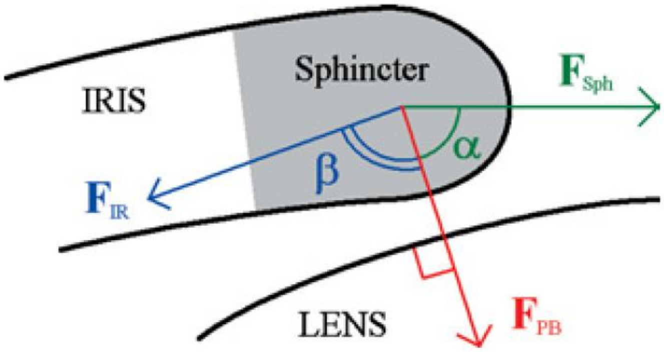

Figure 5-1 Schematic cartoon of pupil-blocking force that holds the iris tip near the lens

Following Heys et al.'s work, Huang and Barocas [39] extended the model to investigate active iris deformation. By imposing an additional circumferential normal stress representing the contraction of the *sphincter iridis* and altering the linear elastic iris to a nearly incompressible neo-Hookean solid, their model was able to confirm Mapstone's pupillary block theory. Mapstone [57] proposed that the pupil-blocking force (F_{PB}) is the sum of active force in the *sphincter iridis* (F_{Sph}) and passive force acting on the iris root (F_{IR}). The pupil-blocking force holds the iris tip close to the anterior lens surface regardless of the pressure between posterior and anterior chamber (Figure 5-1).

The near triad, occurring when the objects are close to the eyes, is defined as simultaneous accommodation, pupil constriction, and convergence. We consider that that convergence is a very minor effect because the whole globe moves as the eyes rotate inward and our current anterior segment model could be modified to simulate simultaneous accommodation and pupil constriction. Pupil constriction and accommodation have been studied in separately computational models [39, 48, 77]. Nevertheless, none of them has fully captured the complex problem of fluid-structure interaction between the aqueous humor (AH) and the iris, blinking, pupil constriction, and motion of the lens during the accommodation in a single comprehensive model. Simultaneous simulation of the two phenomena may determine if there is any synergistic interaction between accommodation and constriction.

The goal of this work was to examine AH and iris mechanics during accommodation and constriction. There are, however, different ways to combine constriction with accommodation. The first alternative is to constrict the pupil prior to accommodation. The second alternative is to introduce the lens movement and active iris stress to the model simultaneously. These two cases were performed and the outcomes were compared.

5.3 Methodology

In order to simulate the near triad with blinking, the following changes were applied in the anterior segment model:

5.3.1 Accommodation

Accommodation was modeled by moving the boundary of the anterior lens surface. Koretz et al. [81] described the anterior surface of the lens as a function of distance from the corneal axis by a parabolic function:

5-1

where and are radial and axial coordinates of the anterior lens surface. The parameters and are time-dependent and were calculated by assuming that there exists a position at the lens periphery that remains fixed. Based on the fact that the human eye accommodates principally by varying lens curvature and not position of the lens, this assumption is acceptable. Based on measurements of Cook and Koretz, the fixed point was set to be approximately 4 mm from the pupillary axis [82]. Under steady conditions, the initial position of the lens was set such that the calculated anterior chamber depth was approximately 3 mm, consistent with data for a normal eye [82, 83]. We assumed that during full accommodation, the anterior chamber depth changed by 0.2 mm over 0.5 s.

5.3.2 Constriction

The sphincter, a circumferentially-aligned smooth muscle, is located within the iris near the pupillary margin. The smooth muscle fibers are about 750-800 μm in width and 100-170 μm in thickness for humans [4]. The sphincter shortens more on contraction than other smooth muscles. In the model, the sphincter elements were localized in pupillary margin as shown in Figure 5-2, and the rest of the iris was modeled as stroma (passive) material.

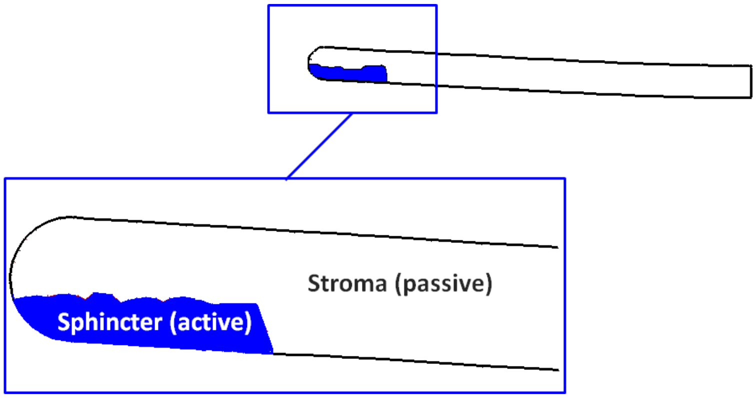

Figure 5-2 The Sphincter section localized within pupillary margin about 750 μm in width and 170 μm in thickness.

The model incorporated active sphincter contraction by imposing an additional circumferential normal stress on top of the neo-Hookean stress as defined by the following equations:

5-2

5-3

where and represent the stress of the active (sphincter) and passive (stroma), respectively and were used in Cauchy momentum equation (Equation 4-1). is the normal unit vector representing in the circumferential direction ( ), the symbol represents dyadic product, and is a scalar stress acting on sphincter muscle in circumferential direction to constrict the iris.

5.3.3 Blinking

5.3.3.1 Iris root

Based on our pervious study [61],we simulated each blink as 80 ms of closing during which the iris was rotated posteriorly, 200 ms opening during which the iris was rotated back to the pre-blinking position, and a hold during which the iris maintained at the pre-blinking configuration for 2720 ms to complete the three-second blink period [84, 85]. These steps were repeated over time to simulate blinking. Iris root rotation was imposed as a Drichlet boundary condition. For this study, the iris root was rotated 2.5° posteriorly during each blink.

5.3.3.2 Ciliary body

Similar to the iris root, ciliary body rotation was imposed as a Drichlet boundary condition to the pseudo-solid domain on the ciliary boundary where a net inflow of 2.5 was strongly imposed to satisfy the following equation:

— 5-4

5.3.4 Study design and implementation

Four cases were considered to examine the effect of blinking, constriction, and accommodation in a single computational model as well as the effects of compressibility on changes of iris profile:

SEQ-COMP (sequential-compressible) and SEQ-INC (sequential-incompressible): accommodation occurred over 0.5 s during which anterior chamber depth decreased 0.2 mm, followed by pupil constriction with = 20 kPa applied during 0.5 s. The iris was modeled as a compressible ($\nu = 0.3$) and a nearly incompressible ($\nu = 0.49$) material in SEQ-COMP and SEQ-INC, respectively.

SIMUL-COMP (simultaneous-compressible) and SIMUL-INC (simultaneous-incompressible): accommodation and pupil constriction occurred simultaneously over 1.0 s during which anterior chamber depth decreased 0.2 mm (accommodation) and = 20 kPa was applied to the sphincter section (constriction). The iris was modeled as compressible and nearly incompressible material in SIMUL-COMP and SIMUL-INC, respectively.

In all four cases, at the beginning of each simulation, blinking was performed during an initial 10 s period over which 3 blinks occurred. Figure 5-3 is a schematic illustration of different cases. The changes in the apparent iris-lens contact, AOD500, iris curvature, and pressure difference between posterior and anterior chamber, $\Delta P = P_{Posterior} - P_{Anterior}$, were calculated for each case.

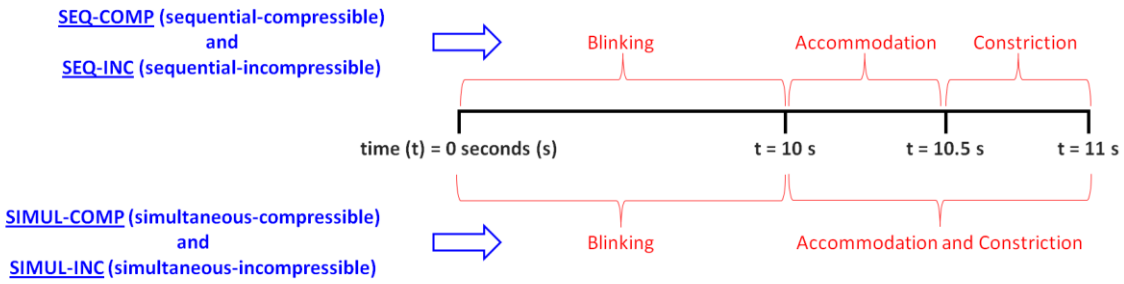

Figure 5-3 Four different cases were simulated. In cases of SEQ-COMP and SEQ-INC, accommodation and constriction were simulated simultaneously for compressible and incompressible iris, respectively where in cases of SIMUL-COMP and SIMUL-INC, accommodation simulation was followed by constriction for compressible and incompressible iris, respectively.

5.4 Results

More detailed explanations about changes in the iris profile during simulated blinking are presented in Appendix B. The results of the blinking portion of the simulation are shown in Figure 5-4. When the iris root was rotated back to its original position after blinking, small increases in AOD500 (Figure 5-4a) and apparent iris-lens contact distance (Figure 5-4b) were predicted, indicating that the iris was close to the lens. The iris concavity (Figure 5-4c) and ΔP (Figure 5-4d) decreased slightly in both compressible and incompressible models.

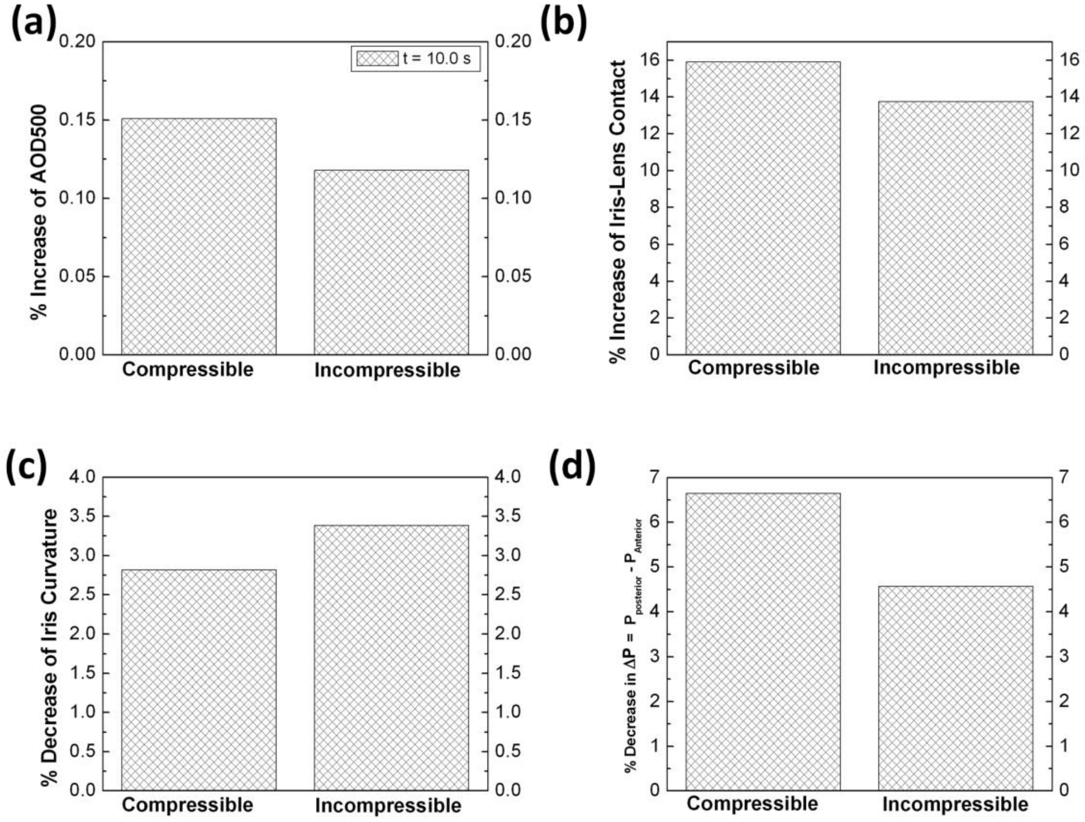

Figure 5-4 (a) % increase of iris curvature, (b) % decrease of iris-lens contact, (c) % decrease of AOD500, and (d) pressure difference between the posterior and anterior chamber after 3 blinks at t = 10 s for compressible and incompressible models.

The aqueous humor pressure distribution and iris profile for case of SEQ-COMP (sequential-compressible) is shown in Figure 5-5. After three blinks (Figure 5-5a), the iris is nearly linear with a slight pressure difference between the posterior and anterior chambers (ΔP = +1.0 Pa), but after accommodation (Figure 5-5b), the iris concavity is significantly increased because of reverse pupillary block (ΔP = -6.0 Pa). Constriction caused a more pronounced change in ΔP= -35.0 Pa as well as greater iris curvature

(Figure 5-5c). Finally, when the eye was allowed to stay accommodated and constricted for 420 seconds (Figure 5-5d), pupillary block and steady secretion of aqueous into the posterior chamber drove the iris away from the lens.

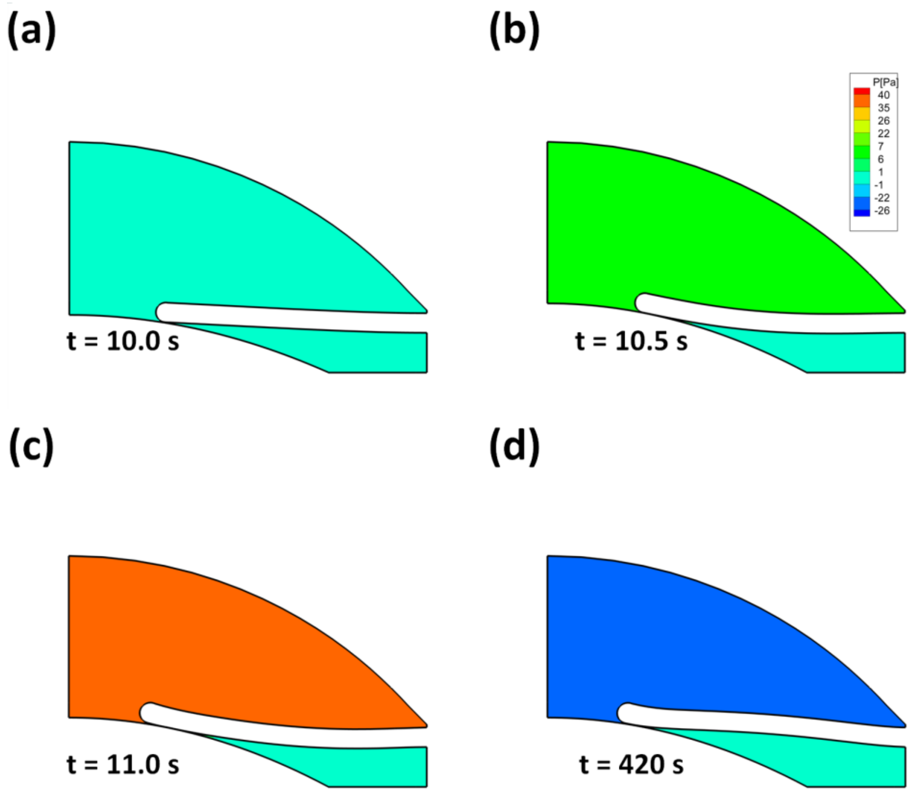

Figure 5-5 Iris profile and aqueous humor pressure distribution for case of SEQ-ICOMP (a) after blinking (t = 10 s) (b) after accommodation and beginning of pupil constriction (t = 10.5 s) (c) after pupil constriction (t = 11.0 s) (d) long after accommodation and constriction (t = 420 s).

The aqueous humor pressure distribution and iris profile for case of SIMUL-INC (simultaneous-incompressible) are shown in Figure 5-6. The combination of pupil constriction and accommodation produced significant posterior bowing of the iris immediately after accommodation and constriction (Figure 5-6c).

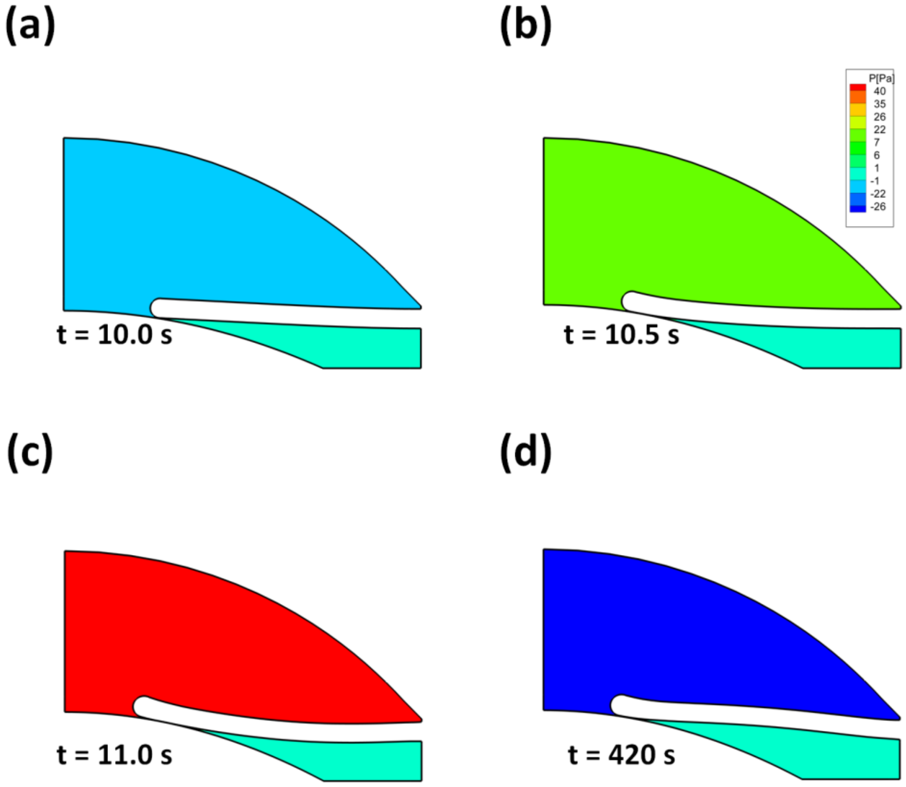

Figure 5-6 Iris profile and aqueous humor pressure distribution case of SIMUL-COMP (a) after blinking (t = 10 s) (b) middle of accommodation and pupil constriction (t = 10.5 s) (c) after pupil constriction and constriction (t = 11.0 s) (d) long after accommodation and constriction (t = 420 s).

Figure 5-7 show the simulation results for all four cases at t = 10.5 s and t = 11 s. Both accommodation and constriction caused the iris to deform into a concave configuration, indicated by negative iris curvatures (Figure 5-7a), and the ACA get wider as measure by an increase in AOD500 (Figure 5-7b). During accommodation, however, the anterior movement of the lens caused the pressure in the anterior chamber to be higher than the pressure in the posterior chamber (reverse pupillary block) as shown in Figure 5-7c. There were significant increases in apparent contact during accommodation and constriction for all cases (Figure 5-7d).

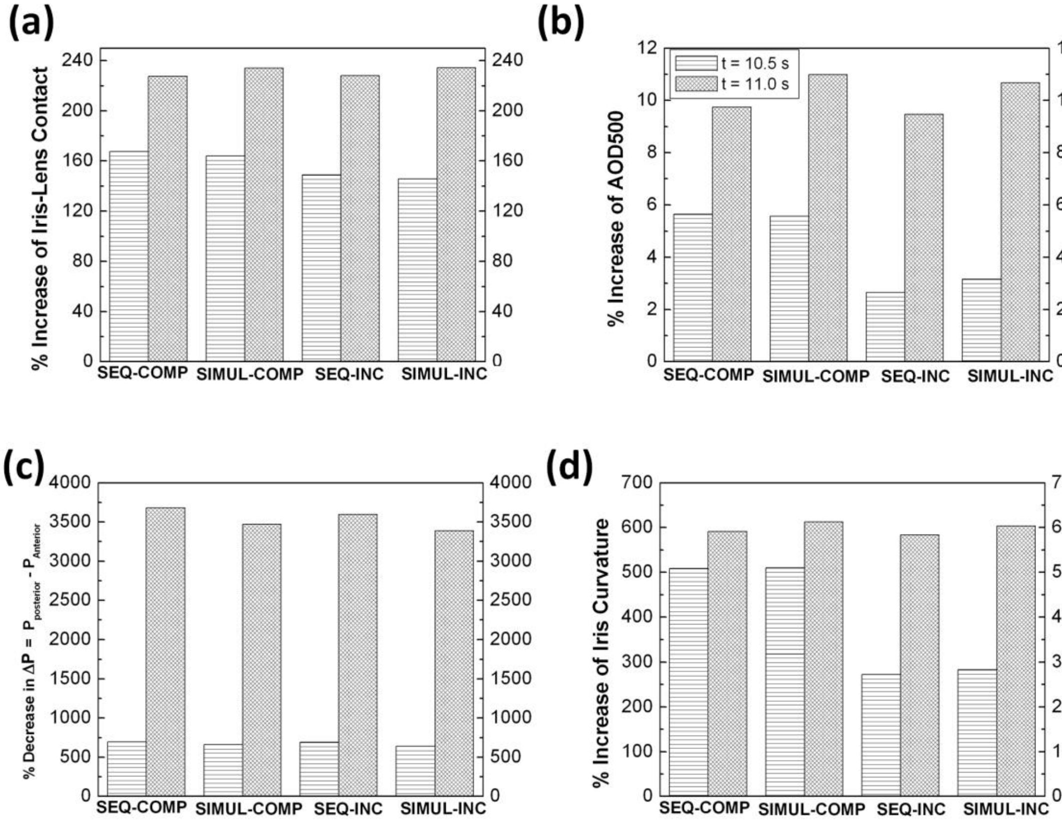

Figure 5-7 (a) % increase of iris curvature, (b) % decrease of iris-lens contact, (c) % decrease of AOD500, and (d) pressure difference between the posterior and anterior chamber at t = 10.5 s and t = 11 s. Iris is modeled as compressible material in cases of SEQ-COMP and SIMUL-COMP and as incompressible material in cases of SEQ-INC and SIMUL- INC.

At t = 10.5 s, which is the end of accommodation simulation, and at t = 11 s, which is at the end of accommodation and pupil constriction, the iris bowed posteriorly approximately 500% and 600% in SEQ-COMP and SEQ-INC (Figure 5-7d). These results indicate that posterior bowing of the iris was affected more by accommodation than by constriction. However, as shown in Figure 5-5c, the pressure difference between posterior and anterior cambers was influenced by constriction.

Comparing the results of SIMUL-COMP and SIMUL-INC at t = 10.5 s (at the middle of accommodation and constriction simultaneously simulations) and t = 11.0 s (at the end of accommodation and constriction simultaneously simulations), we see that the rate of change in calculated parameters were not linear. However, our results also predicted that accommodation followed by pupil constriction (SEQ-COMP and SIMUL-COMP) each during 0.5 s and accommodation and pupil constriction simultaneously during 1.0 s (SEQ-INC and SIMUL-INC) were nearly the same. All of the calculated parameters returned to their pre-blinking steady-state values over 420 s.

The effect of compressibility of the iris was more noticeable in changes of AOD500 (Figure 5-7b) and ΔP (Figure 5-7c).

5.5 Discussion

Clinical studies have shown that accommodation leads to posterior bowing of the iris, particularly in PDS patients who have a flaccid and/or smaller iris [47, 79]. Dorairaj et al. [86], for instance, examined the iris profile immediately and long after accommodation in normal subjects, ACG, and PDS patients. Using UBM imaging techniques, they were found that the largest drop in iris curvature and fastest recovery from the initial posterior displacement after accommodation occurred in PDS patients (probably due to a “reverse pupillary block” effect). The idea of reverse pupillary block is applied to accommodation as well as constriction; the anterior motion of the central lens pushes AH toward the peripheral posterior chamber, but the iris is pinned against the lens and blocks the flow causing higher pressure in anterior chamber than in the posterior chambers and resulting in an increase of iris-lens contact. In normal eyes, similar effects were also caused by blinking or accommodation.

The posterior bowing of the iris in PDS patients can be reversed with prevention of blinking, or pharmacologic miosis [87], and LPI [79, 87] but is increased with accommodation [86]. Liu et al. [88] examined the changes of the iris contour of patients with PDS after blinking, accommodation, and pharmacologic miosis (a drop of pilocarpine 2%). They found that the concave shape of iris became planar with blinking and only became posteriorly curved when accommodation was induced. Pupil constriction caused by pilocarpine made the iris planar.

This computational study evaluated accommodation and constriction in a single computational model to extend our understanding of the anatomical and dynamic iris factors that predispose towards development of PDS. Our results predicted that the combination of pupil constriction and accommodation produced significant posterior bowing of the iris. However, obtaining the same results in cases of SEQ-COMP and SIMUL-COMP (SEQ-INC and SIMUL-INC) indicates that the interaction between and accommodation and constriction is not synergistic. The effect was more pronounced when the iris was incompressible; suggesting that changes in iris volume could play a role in PDS [24] similar to that seen in angle closure [16].

Chapter 6 Spatial Heterogeneity of Iris Elasticity Measured by Indentation

6.1 Summary

The purpose of this study was to obtain the mechanical properties of individual components of the iris-specifically, the dilator, sphincter, and stroma. Nanoindentation experiments and histological mapping were performed in combination with a three-dimensional finite element (FE) model. A total of 12 porcine irides were indented in three different regions on the anterior and posterior surfaces and a load-displacement curve for each experiment was obtained. Histological analysis of one sample was done to determine the relative location of the three major constituent components during indentation. Using ABAQUS (SIMULIA, Providence, RI), two FE models (compressible and incompressible models) were created to simulate indentation. The sphincter and dilator were treated as incompressible neo-Hookean solids in both models, while the stroma was varied as a compressible ($\nu = 0.3$) and an incompressible neo-Hookean ($\nu = 0.495$) solid. Three linear combinations of elastic moduli were assigned to the sphincter, the dilator, and the stroma and indentation simulations were performed similar to the experiment indentation locations. Experimental force-displacement curves were compared using an inverse method to calculate individual elastic modulus for the dilator, sphincter, and stroma. In the incompressible model, using the linear region, the elastic modulus of dilator, computed by the slope of the toe region (0-50 μm on force-

displacement curve), was 1.43 ± 0.88 kPa (mean ± 95% CI, n = 4 iris simulations) compared to 1.21 ± 0.18 kPa for the stroma. Due to the location of the sphincter in the iris, the sphincter was only targeted in one indentation region, therefore, the elastic modulus was low and had high variance (0.33 ± 0.60 kPa). We have successfully shown that the specific components of the iris vary spatially, which can play an important role in the natural contour of the iris. The simulation results, however, do not completely capture the behavior of the iris since the poroelastic behavior, of the stroma was ignored.

6.2 Introduction

One of the determining factors in the deformation of the iris is the internal stresses generated due to the passive and active components of the constituent tissue. Although the mechanical model of iris-aqueous humor) (AH interaction can explore several physiological ocular phenomena by capturing the fluid-structure interaction of the AH flow and the iris, assessing the mechanical properties of the iris is also essential to understand ocular diseases and creating accurate computational models.

In addition to certain types of glaucoma (such as ACG [18] and PDS [89, 90]), IFIS [26] is directly related to the abnormal morphologies of the iris. Structural changes including thinning of the iris as whole [28], especially the dilator muscle, have been noted [14]. Prata et al. [28] found that patients using systemic α-1 adrenergic receptor antagonists have significantly thinner iris dilator muscle and smaller ratio of dilator/sphincter thickness and smaller pupil diameter. Although no changes in mechanical properties of dilator muscle (or iris) have reported directly, one may assume that atrophic anatomical changes in the dilator muscle may suggest changes in mechanical properties of the iris. Therefore, characterizing the mechanical behavior of the iris may help us to understand how the physiology and pathophysiology of the iris can affect diseases of the eye. An evaluation of the composition of the iris, especially the dilator muscle, can lead to a better understanding of how IFIS, ACG, and PCG may affect the overall contour of the iris.

There have been a few studies quantifying the mechanical properties of the iris. Heys and Barocas [66] measured the Young’s modulus of bovine iris by performing extension tests in the radial and azimuthal direction. The average azimuthal Young's modulus of the *sphincter iridis* was reported to be 340 kPa, where the azimuthal and radial Young's modulus of the *dilator pupillae* was found to be 760 kPa and 27 kPa, respectively. Similar to Heys and Barocas [66], Lei et al. [91] found that the azimuthal elastic modulus (24.7 kPa) was larger than the radial modulus of 5.3 kPa. Whitcomb et al. [92] examined pharmacological effects on the porcine iris stiffness to study the active mechanics of the iris. The modulus of porcine samples was measured before and after inducing mydriasis and miosis with drugs such as pilocarpine, phenylephrine, and tropicamide. As discussed in Chapter 1, tropicamide produces short-acting mydriasis by inhibiting the sphincter. Pilocarpine causes miosis not only by activating the sphincter but also by inhibiting the dilator, and phenylephrine causes pupillary dilation by stimulating the dilator muscle. Whitcomb et al. found that the modulus of the untreated iris using uniaxial stretch was 2.97 ± 1.3 kPa and 4.0 ± 0.9 kPa for circumferential and radial stretch, respectively. An increase (at least 1.5 times) in Young's modulus was reported after the iris was stimulated by the drugs.

In another study, Whitcomb et al. [13] explored how the different components of the iris contribute to the overall mechanical behavior using nanoindentation. Indentation stress-relaxation experiments were performed on both posterior and anterior surfaces using an indenter with a 1 mm cylindrical tip. The load-displacement curve for each experiment was used to estimate effective instantaneous and equilibrium moduli for the anterior and posterior surfaces of the tissue. Whitcomb et al. [13] found that the forces measured when indenting the posterior surface were roughly twice those measured for the corresponding indentation of the anterior surface. From these indentation tests, instantaneous moduli of 6.0 ± 0.6 kPa and 4.0 ± 0.5 kPa, and equilibrium moduli of 4.4 ± 0.9 kPa and 2.3 ± 0.3 kPa, were reported for posterior and anterior surface of the porcine irides, respectively. The conclusion of this study was a significant asymmetric stiffness of the iris under anterior vs. posterior indentation. Whitcomb et al. [13] also performed histological analysis on the albino porcine iris to characterize the thickness of the stroma, dilator, and sphincter. They found the average thickness of the dilator and sphincter to be around 26 µm and 133 µm, comparable to histological data analyses for human irides [4]. While the authors attributed the asymmetry to structural heterogeneity within the iris, they were unable to distinguish differences among the specific constituent components of the iris. More recently, Yoo et al. [93] also calculated the stiffness of different ocular tissues including the bovine irides using microindentation, and reported 4.86 kPa and 0.24 kPa for instantaneous and equilibrium modulus of the bovine irides, respectively.

Table 6-1 the experimental studies conducted on the iris.

Investigator	Species	Methods	Conclusion
Lowenfeld *et al.* 1971 [94]	Human	*In Vivo* pupil analysis	Pupil diameter changes were linear. Limited changes in sphincter & dilator regions occurred when either muscle was activated.
Tabandeh *et al.* 1995 [95]	Human	*Ex Vivo* relative active force tests	Sphincter activation resulted in 27.5 mN force and dilator activation resulted 23.3 mN
Heys *et al.* 1999 [66]	Bovine	Radial and Azimuthal extension experiments	**Dilator:** Radial modulus was 27 kPa and azimuthal modulus was 760 kPa **Sphincter:** Azimuthal modulus was 340 kPa
Yamaji *et al.* 2003 [96]	Rabbit	*Ex Vivo* length–tension relationship	Maximum force for sphincter and dilator corresponds to min/max pupil diameter
Lei *et al.* 2007 [91]	Porcine	*Ex Vivo* pupil analysis	Radial modulus was 5.3 kPa & azimuthal modulus was 24.7 kPa
Whitcomb *et al.* 2009 [92]	Porcine	Passive and Active mechanics	**Radial modulus:** passive modulus was 4.0 kPa and active was 7.7 kPa **Azimuthal modulus:** passive modulus was 3.0 kPa and active was 5.3 kPa
Whitcomb *et al.* 2011 [13]	Porcine	Nanoindentation	**Instantaneous modulus:** modulus was 6.0 kPa (posterior surface) and 4.0 kPa (anterior surface) **Equilibrium modulus:** modulus was 4.4 kPa (posterior surface) and 2.3 kPa (anterior surface)
Yoo *et al.* 2011 [93]	Bovine	Nanoindentation	Instantaneous modulus was 4.86 kPa and equilibrium modulus was 0.24 kPa

Table 6-1 summarizes the experimental studies conducted to characterize the mechanical properties of the iris. These experimental studies quantified the mechanical properties of the iris and addressed to various degrees the nonlinear and viscoelastic behavior of the iris, but, no research has been done to determine the relative contributions of the composing segments in a realistic model of the iris. The goal of this study was to explore the effect of the varying mechanics throughout the iris tissue and to determine the contribution to the overall mechanical behavior from three distinct structures of the iris: the stroma, the *sphincter iridis*, and the *dilator pupillae*. We combined nanoindentation, applied in different locations on the two surfaces of the iris, with an anatomically-based FE model to determine the properties of main components of the iris. Nanoindentation was used because this technique can measure local material properties in small, thin, and heterogeneous samples, making it suitable for extracting the individual properties of the iris components due to its small probe size [97, 98]. Furthermore, nanoindentation is far more sensitive to the tissue properties near the indenter than to those far from the indenter [99].

6.3 Methodology

6.3.1 Nanoindentation experiment

The iris was segmented into three regions - iris root (IR), mid-periphery (MP), and pupillary margin (PM) - as shown in Figure 6-1. The PM region contained primarily the stroma and sphincter on the anterior and posterior surfaces, respectively. The MP contained all three components, and the IR region contained the stroma and dilator on the anterior and posterior surfaces, respectively. Intact porcine irides were cut into two equal C-shaped halves and pinned to the aluminum stage of nanoindentation device. A nanoindentation test of the porcine iris was performed to assess the relative stiffness of these regions on the anterior and posterior surfaces. Indentation tests were performed using a Nanoindenter XP (MTS Inc., Eden Prairie, MN) with 0.02 mN and 30 nm load and displacement resolutions, respectively.

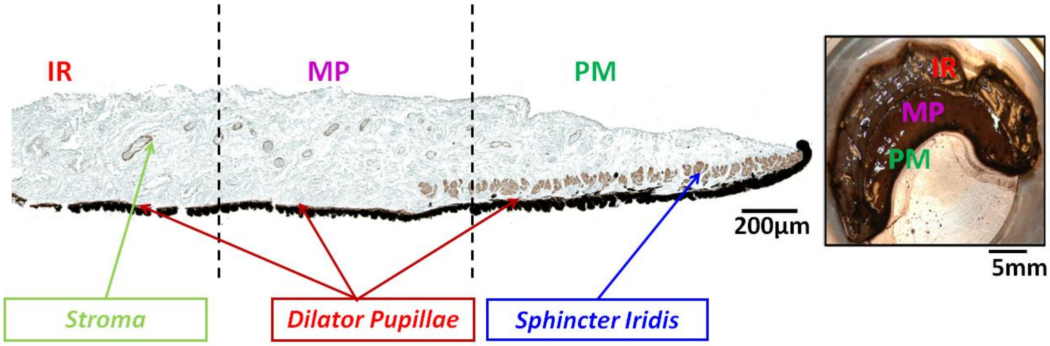

Figure 6-1 Iris was divided into three regions: IR, MP, and PM. The IR region includes the stroma and dilator. The MP region contains all three components, whereas the PM region includes mostly the sphincter and stroma.

Each sample was indented with a 1mm diameter non-porous flat-ended cylindrical indenter tip. The indentation protocol was a two-step 2.0 mN/s ramp with a hold at fixed displacement for 400 s between steps. The instantaneous modulus ( ) was calculated from the slope of the load-depth curve during rapid indentation (between 0.5-1.0 mN on the first ramp) whereas viscoelastic parameters of the tissues were obtained from stress relaxation during the 400 s hold. The equilibrium modulus ( ) were obtained from the slope of the load-depth curve during rapid indentation and using the data point at the end the of 400 second holds, respectively (Figure 6-2).

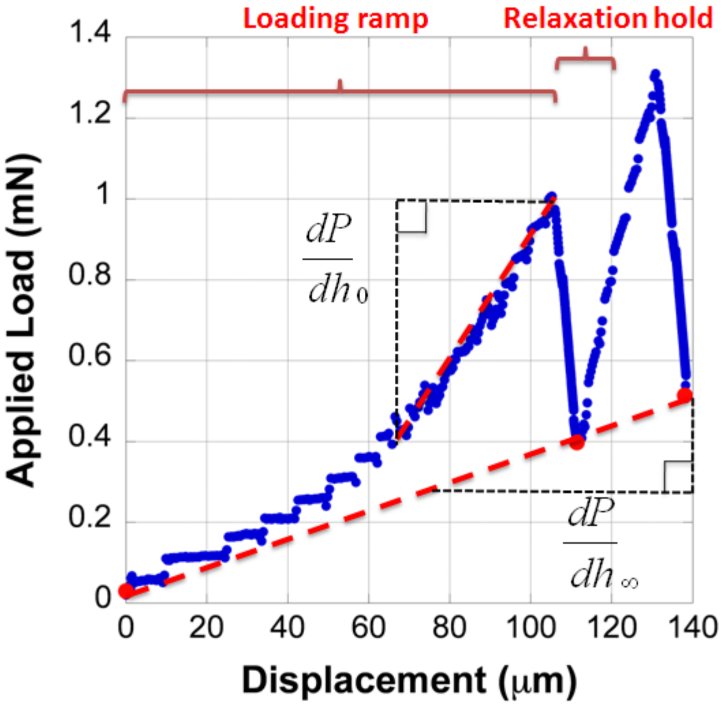

Figure 6-2 Representation of the calculation used to determine the effective instantaneous ( ) and equilibrium ( ) moduli for the iris.

Chiravarambath et al. [100] proposed that the modulus , for linear elastic materials indented by at flat-cylindrical tip can be defined by

— ——— 6-1

where is the indentation force, ν is the Poisson's ratio of the material, and − is a correction factor where is a function of the sample thickness, , and radius of cylindrical tip, , [101]. The iris was assumed to be nearly incompressible ($\nu = 0.495$) [66].

A relaxation function of the shear modulus with time, , was calculated from the instantaneous modulus, :

6-2

The continuous relaxation spectrum (above equation) can be replaced by a series of discrete relaxation functions. By assuming the iris as isotropic material, Suh et al. [102]showed that this continuous model is comparable to a three-exponential Prony series:

6-3

and are the viscoelastic constants, and represents the equilibrium shear modulus obtained by assuming that the equilibrium was achieved at the end of the hold period [102]. The viscoelastic parameters of the tissue were found by fitting shear modulus-time data to Equation 6-3. was assumed to be different from because a sharp drop in force was seen in the relaxation data [100]. The intermediate relaxation rate was defined as

6-4

The differences between the mechanical responses of the anterior and posterior iris surfaces as well as different regions (i.e. IR, MP, and PM) were quantified using student t-tests for paired data with equal variance. Two-way ANOVA was used for varying tissue characteristics. Statistical analysis was performed using Origin software (OriginLab, Northampton, MA).

6.3.2 Finite element model

Indentation of a 3D detailed structure of the iris was simulated using ABAQUS (SIMULIA, Providence, RI), similar to the indentation experimental tests. The indenter tip was modeled as a rigid body, flat-ended cylinder with a 1 mm diameter. The iris contour and its components were generated based on a histological image (Figure 6-1). The dilator and sphincter muscles were modeled with an average thickness of 80 and 300 µm, respectively whereas the thickness of the iris was 1100 µm at the iris root and 600 µm at the pupillary margin. The iris was modeled as a tridomain material consisting of three homogenous isotropic Neo-Hookean sections. The neo-Hookean material in ABAQUS is expressed in terms of and as defined as:

— 6-5

— 6-6

where and are the initial shear modulus and bulk modulus. Equations 6-5 and 6-6 can be rewritten as

——— 6-7

——— 6-8

The values determine the compressibility of the material; for a fully incompressible material, = 0. However, in this study we considered two cases: (1) a nearly incompressible stroma with $\nu = 0.495$ and (2) a compressible stroma $\nu = 0.3$ to represent a healthy and ACG, respectively.

200,000 to 400,000 C3D8R elements were used for the iris domain, with finer elements employed near the contact region where high stress concentration was expected. Contact between the indenter (master) and the iris (slave) was assumed to be frictionless, and the nodes on iris surface (the slave) could not penetrate the segments that make up the indenter surface (the master). The boundary condition for the iris was specified by fixing the bottom surface of the iris ($U_x=U_y=U_z=0.0$). The cylindrical indenter was allowed to move only in the vertical direction ($U_x=U_z=0.0$). Indentation in each of the three regions (IR, MP, and PM) on the posterior and the anterior surface of the iris was simulated (Figure 6-3). The 3D iris model was indented approximately 100-200 μm, close to the experimental indentation depth.

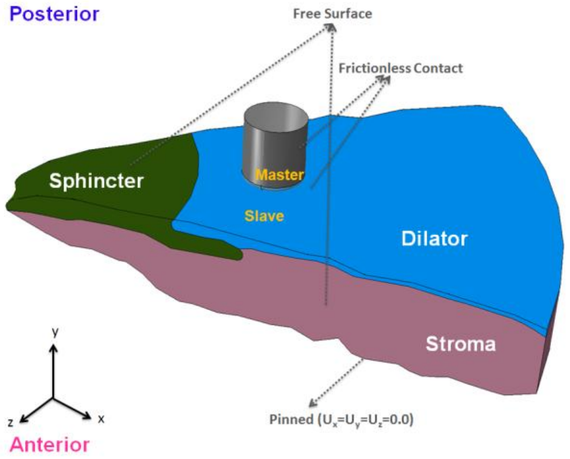

Figure 6-3 A 3D model of the iris with three main components (the dilator, sphincter and stroma). Indenter tip model as a 1 mm cylindrical rigid body. The mid-periphery region on the posterior surface is shown to be indented in this figure.

6.3.3 The inverse method principle

It has been established [103] that indentation of multilayered structures yields different results depending on the arrangement of the layers. We extended the recent method of Azeloglu et al. [104] to correlate a relationship between the elasticity of the iris and the relative contributions of each component. The goal was to quantify the mechanical properties of the iris components through comparisons between the experiments and FE model results. The applied force, , depends on the elastic modulus, , of each material (i.e. dilator, sphincter, and stroma) with a weighting factor,

6-9

The function is a relative weighting factor corresponding to indentation depth and the tissue geometry. For example, when the anterior surface of iris is indented in the IR region where only the stroma and dilator are located, the sphincter does not contribute in the applied force. Therefore, the weighting factors corresponded to the sphincter for all indentation displacement is zero (= 0).

Three linear combinations for elastic modulus of the iris components were assigned to ABAQUS model (Table 6-2), and indentation simulations were performed on three regions on both the posterior and anterior surfaces.

Table 6-2 Three linear combinations for elastic modulus of the iris components.

(matrix in Equation 6-10)

1	1	1
1	1	2
1	2	1

A total of 18 simulations were performed. For the simulation tests, Equation 6-9 was re-written as

6-10

where ***A*** is a 3 by 3 matrix and defined by the 3 linear combinations of elastic moduli in Table 6-2. Using applied force-displacement curves calculated from all the simulation results and the ***A*** matrix, the weighting factors matrix, , was calculated in Equation 6-10. For the experimental tests, Equation 6-9 was re-written as

6-11

For each iris sample, contained the six sets of applied force-displacement data points ( ) recorded from the Nanoindenter, and was a 3 by 1 vector of elastic modulus for dilator, sphincter, and the stroma, and (known after solving Equation 6-10) was an by 3 matrix representing the weighting factor values for all data points, .

To calculate the elastic modulus vector, , weighting factors calculated from simulations, , and the <u>experimental</u> force results were applied to Equation 6-11. A 95% confidence interval (CI) for the modulus of each component of the iris was evaluated:

6-12

where = dilator, sphincter, and stroma, was the t-value for a sample with degree of freedom ( ). and were the number of equations and unknowns, for a 95% confidence interval ( ), and can be obtained by

6-13

where is a vector of simulation forces for all the indentation depth. The residual vector, , and the sum of squares of the residuals, , are:

6-14

6-15

6.4 Results

6.4.1 Nanoindentation experiment

A total of 12 porcine irides (6 pairs) were used for analysis. Figure 6-4 shows a typical force-displacement curve during rapid indentation. The instantaneous moduli for each region and both surfaces ( ) were calculated using Equation 6-1 from the slope of the load-depth curve during rapid indentation between the applied loads of 0.5 mN to 1.5 mN.

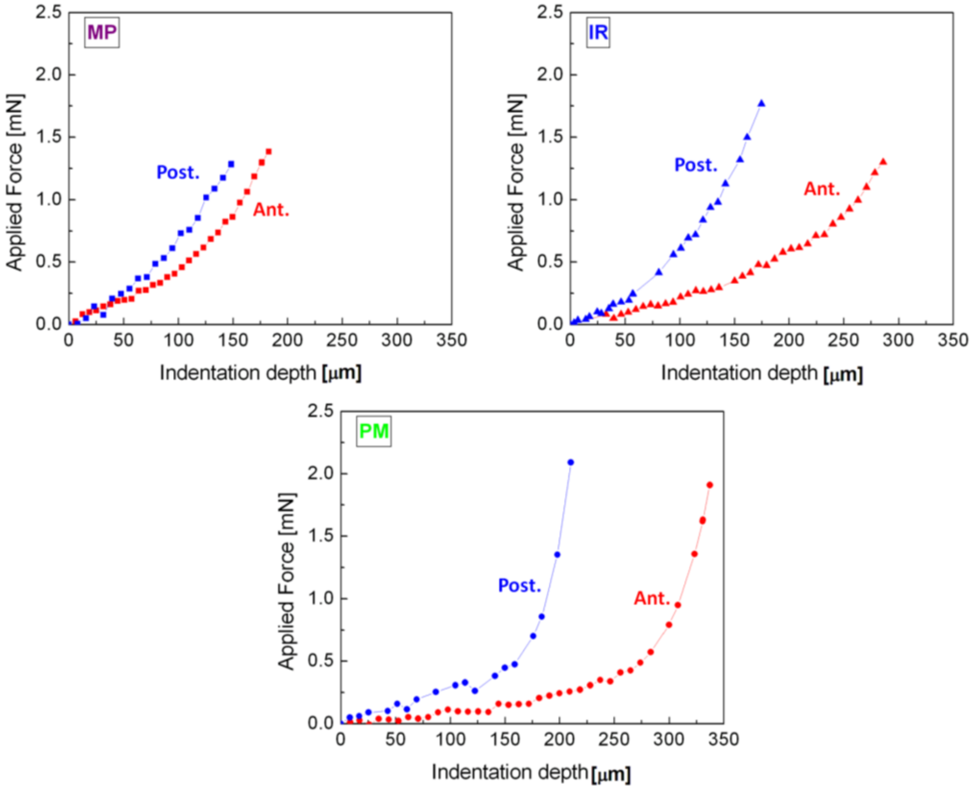

Figure 6-4 Typical applied force-displacement curve from anterior (**Ant.**) and posterior (**Post.**) indentation of pupillary margin (**PM**), mid periphery (**MP**), and iris root (**IR**) regions.

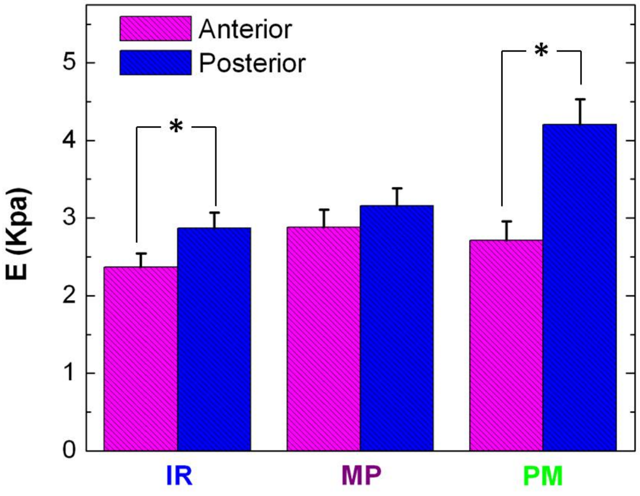

Figure 6-5 Instantaneous modulus of porcine irides for different regions (n=12). Posterior surface of the iris is significantly stiffer than the anterior surface, particularly for the pupillary margin (PM) and iris root (IR). The error bars represent 95% CI and a * indicates a *p*-value < 0.05.

A quantification of the instantaneous modulus of the porcine iris is presented in Figure 6-5.There was no significant difference between the instantaneous modulus of the anterior and posterior surface in the PM region. However, the instantaneous modulus was higher for the posterior surface compared to the anterior surface in the IR and MP regions ($p < 0.05$), consistent with Whitcomb et al.[13], the posterior surface of the porcine iris was stiffer in contrast to the anterior surface.

A typical stress-relaxation curve for the porcine iris is shown in Figure 6-6. Normalized shear modulus-time curve and viscoelastic parameters were generated fitting Equation 6-3 to the experimental relaxation data.

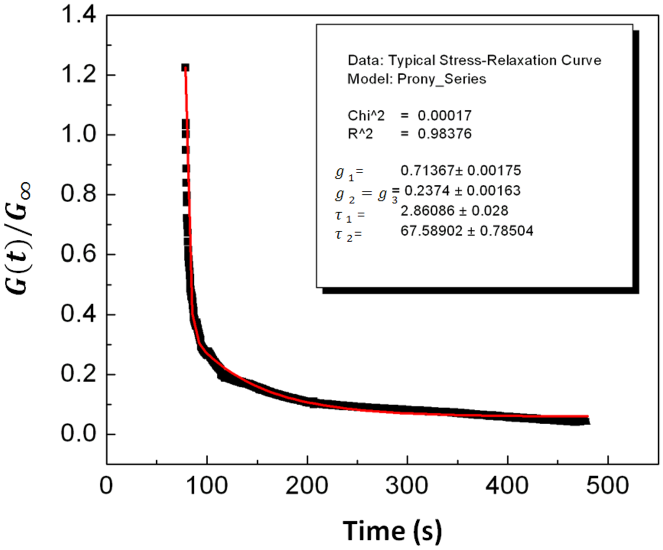

Figure 6-6 Stress Relaxation curve fitting using Prony series

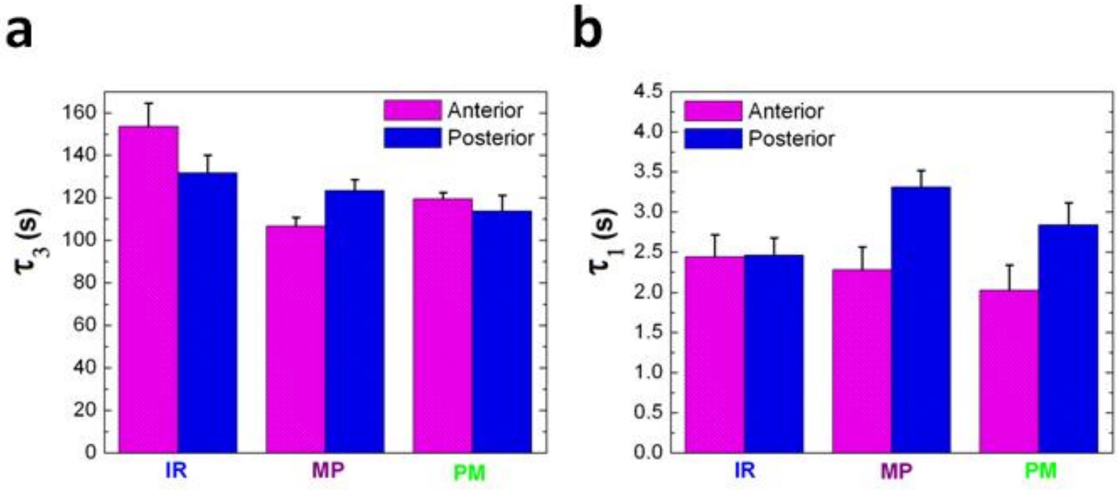

Figure 6-7 viscoelastic time constants (a) Rapid short term response. (b) Slower long term response. The error bars represent 95% CI and a * indicates a p-value < 0.05.

The anterior surface indentation showed a shorter relaxation time constant τ_1 (rapid short time constant) compared to the posterior surface. The only region that had a significant difference between the surfaces was the MP region where anterior was 2.28 ± 0.29 s and 3.31 ± 0.21s on the posterior ($p < 0.05$). In contrast, there was no significant difference of the third Prony relaxation time constant τ_3 (slower time constant) between the anterior and the posterior surface in all regions. However, τ_3, representing slower time constant in the tissue, was significantly different between MP and IR regions, and MP and PM regions on the anterior surface ($p < 0.05$). In addition, τ_3, was smaller for the MP region compared to other IR and PM regions on the anterior surface. Figure 6-7 summarizes the comparison between the relaxation time constants.

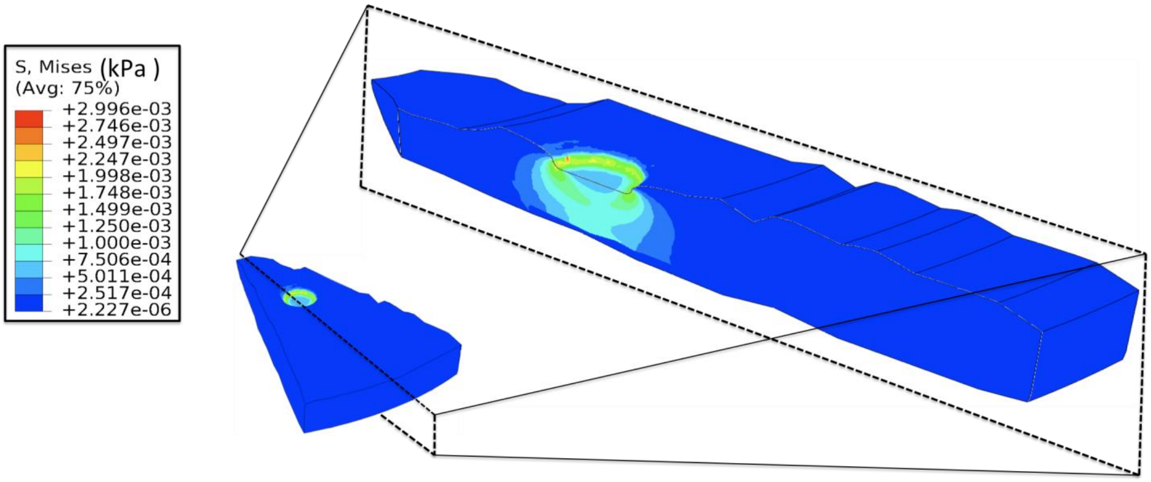

Figure 6-8 Von Mises stress distribution. Nanoindentation is far more sensitive to the tissue properties near the contact regions than to those far from the indenter

6.4.2 Simulation and the inverse method's results

Figure 6-8 shows the force-displacement results from indentation simulation. Higher stress concentration around the indenter tip observed compared to the elements far away from the contact region.

Figure 6-9 and 6-10 show the applied force-displacement curves obtained from ABAQUS simulation as three different sets of elastic moduli were imposed on the dilator, sphincter and stroma sections in the incompressible and compressible models, respectively. Slightly higher forces were observed in the incompressible simulations where slightly nonlinearity was seen in the compressible simulations in the same regions. When the elastic modulus of the dilator, sphincter, and stroma were varied (as shown in Table 6-2), the same trends were observed in both compressible and incompressible models. For example, in both models, for the case of anterior (and posterior) indentation in IR region when and , were assigned to the components of iris the force-displacement curves matched since the sphincter did not exist in the IR region; hence changing the elastic modulus of sphincter would not change the results. Noticeably, higher forces were generated in the simulated indentation of the anterior surfaces in the PM region when were imposed as material properties in both compressible and incompressible.

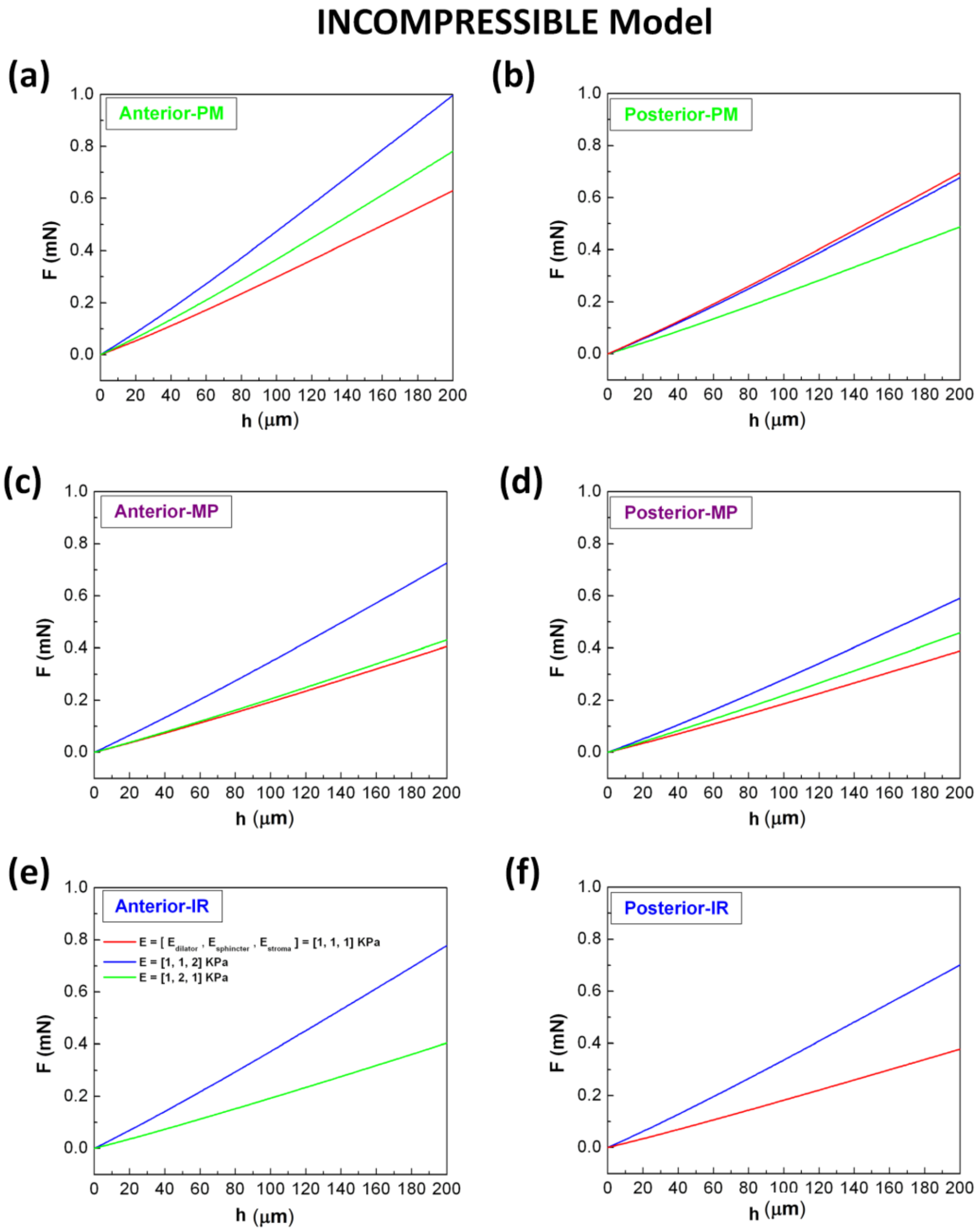

Figure 6-9 Force-displacement curves of incompressible indentation simulations in (a) anterior PM (b) posterior PM (c) anterior MP (d) posterior MP (e) anterior IR, and (f) posterior IR regions when three sets of elastic moduli were imposed to dilator, sphincter, and stroma.

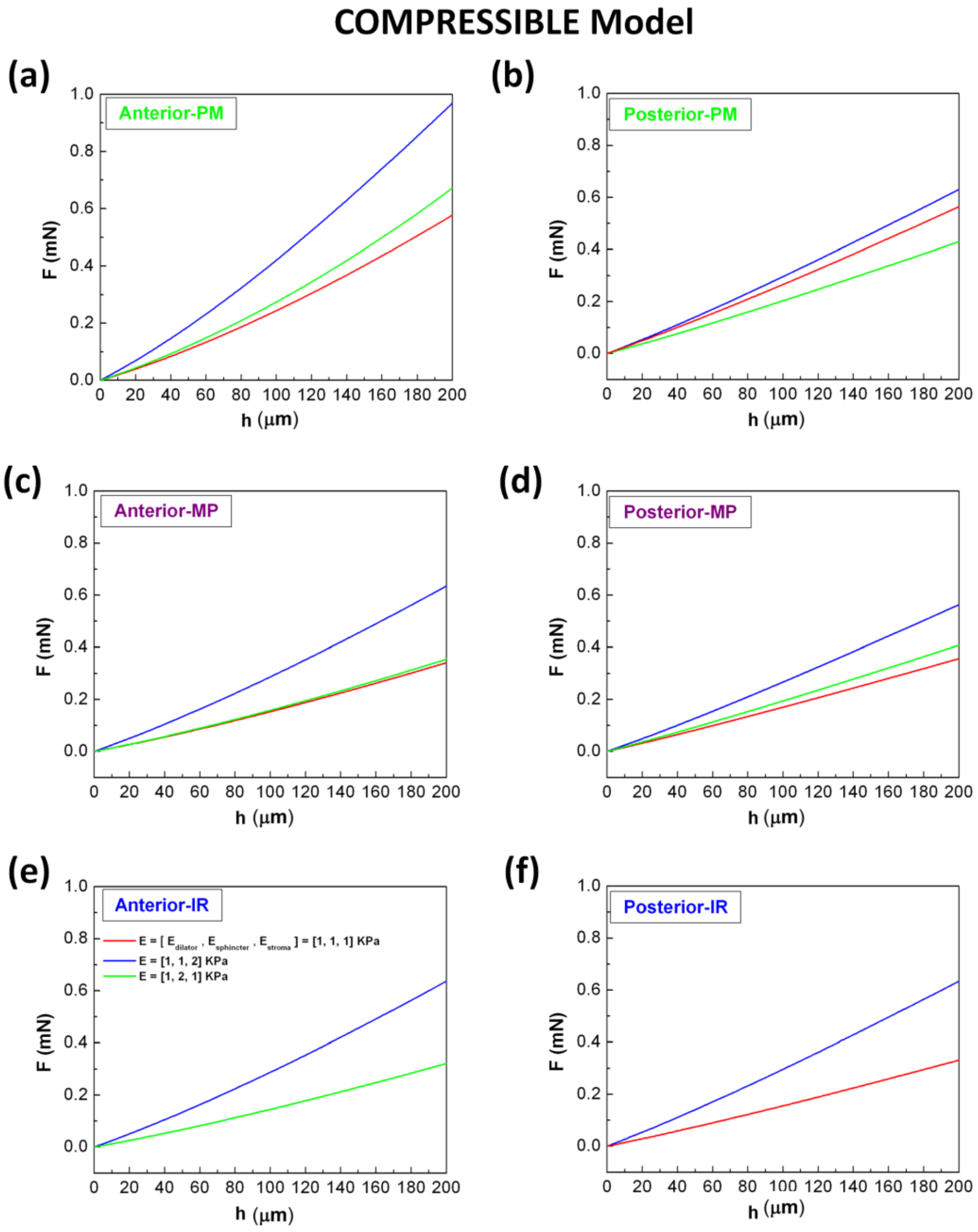

Figure 6-10 Force-displacement curves of compressible indentation simulations in (a) anterior PM (b) posterior PM (c) anterior MP (d) posterior MP (e) anterior IR, and (f) posterior IR regions when three sets of elastic moduli were imposed to dilator, sphincter and stroma.

In all of the cases, anterior surface indentation gave slightly larger forces than posterior surface, which is not consistent with the experimental results. This observation is explained in more detail in discussion section).

Using the force-displacement curves and Equation 6-10, the weighting factors, , were obtained for the dilator, sphincter, and stroma in all regions. Figure 6-11 and 6-12 show the weighting factors calculated for the IR, MP, and PM regions (both posterior and anterior surfaces) for compressible and incompressible models, respectively. Weighting factors corresponding to the stroma had higher values compared to the sphincter and dilator in the IR and PM regions on the anterior surface and vice versa in the IR and PM regions on the posterior surface. As expected, weighting factors corresponding to the sphincter were zero in the IR regions on both posterior and anterior surfaces.

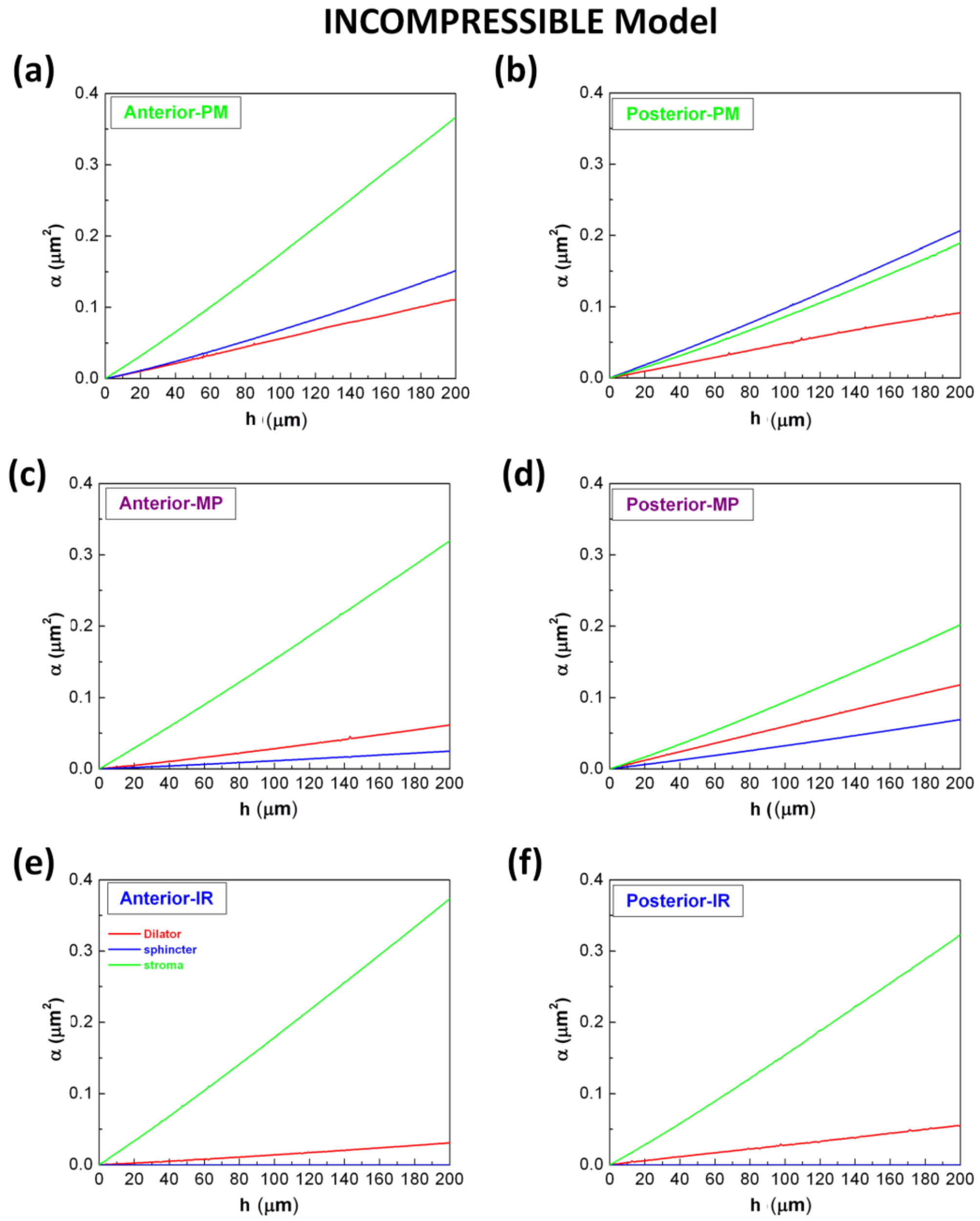

Figure 6-11 Weighting factors corresponding to sphincter (blue), dilator (red), and stroma (green) calculated from the incompressible model in (a) anterior PM (b) posterior PM (c) anterior MP (d) posterior MP (e) anterior IR, and (f) posterior IR regions when three sets of elastic moduli were imposed to dilator, sphincter, and stroma.

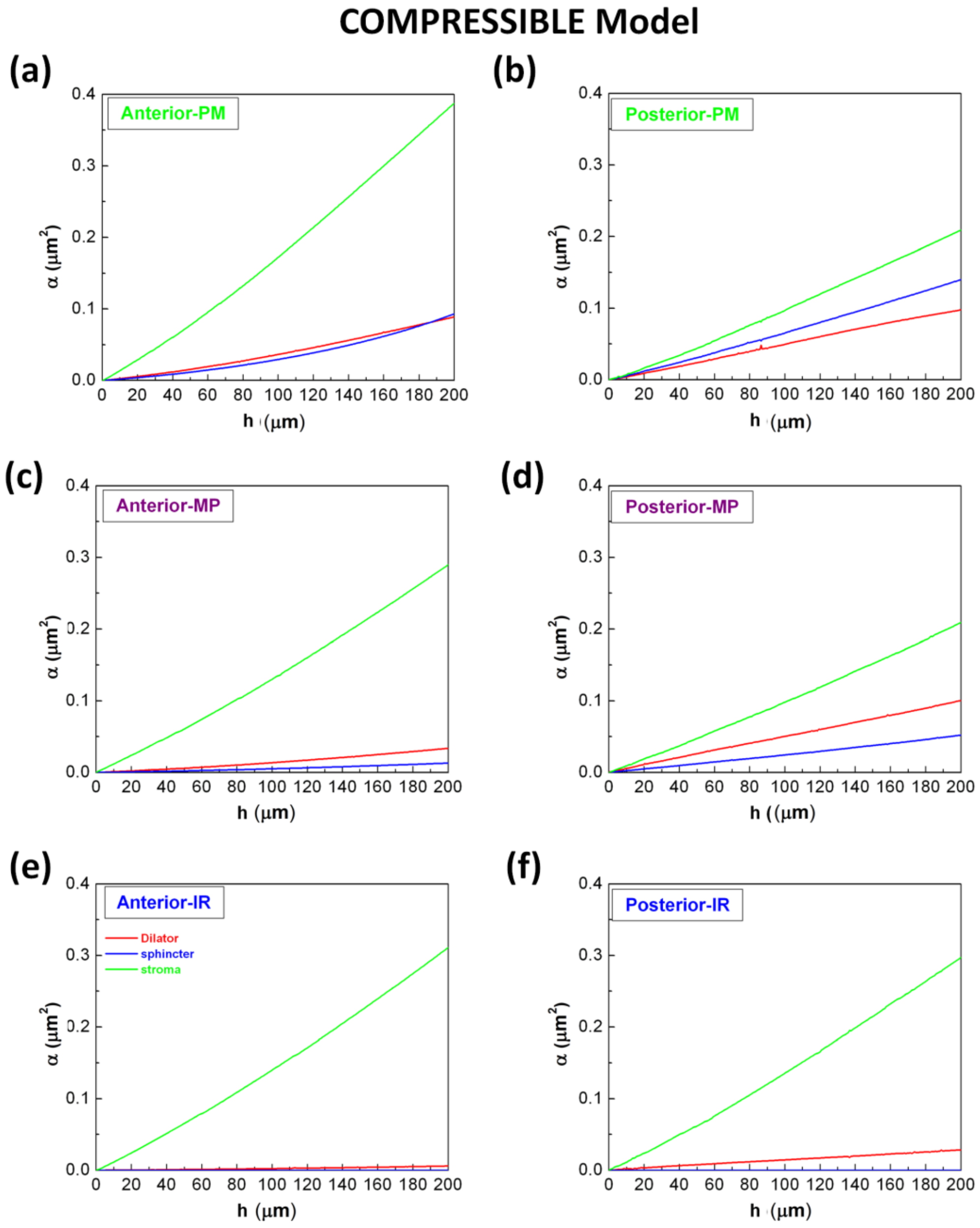

Figure 6-12 Weighting factors corresponding to sphincter (blue), dilator (red), and stroma (green) calculated from the compressible model in (a) anterior PM (b) posterior PM (c) anterior MP (d) posterior MP (e) anterior IR, and (f) posterior IR regions when three sets of elastic moduli were imposed to dilator, sphincter, and stroma.

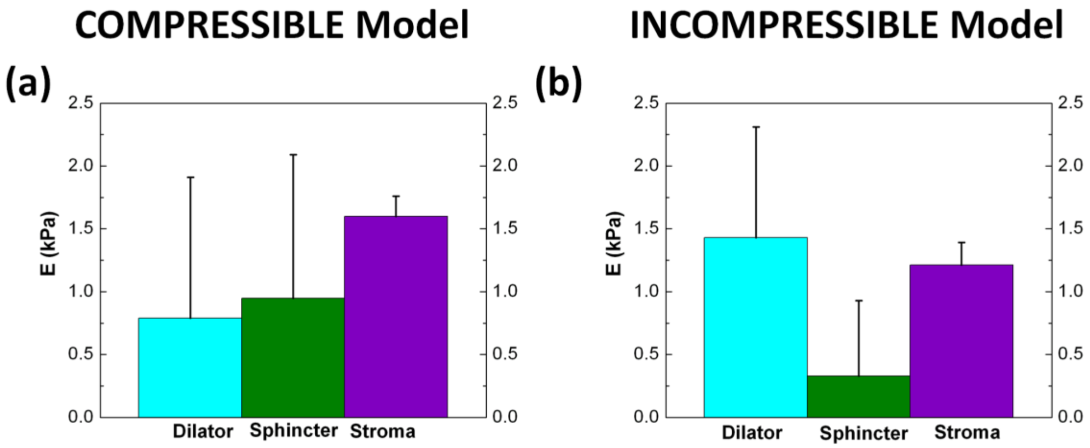

Figure 6-13 Elastic modulus for the dilator, the sphincter and the stroma were obtained through comparison the (a) compressible and (b) incompressible model and experiments results.

The accuracy of the inverse method was confirmed by creating a mock indentation simulation. The elastic moduli for the dilator, sphincter, and stroma were assigned with values of 1.1 kPa, 2.0 kPa, and 4.0 kPa in the ABAQUS's model, respectively. Six sets of indentation simulations were performed on both surfaces and all the regions (IR, PM, and MP). Using the weight factors matrix, , and applied force results of this set of simulations in Equation 6-11, the elastic modulus vector gave expected values of , .

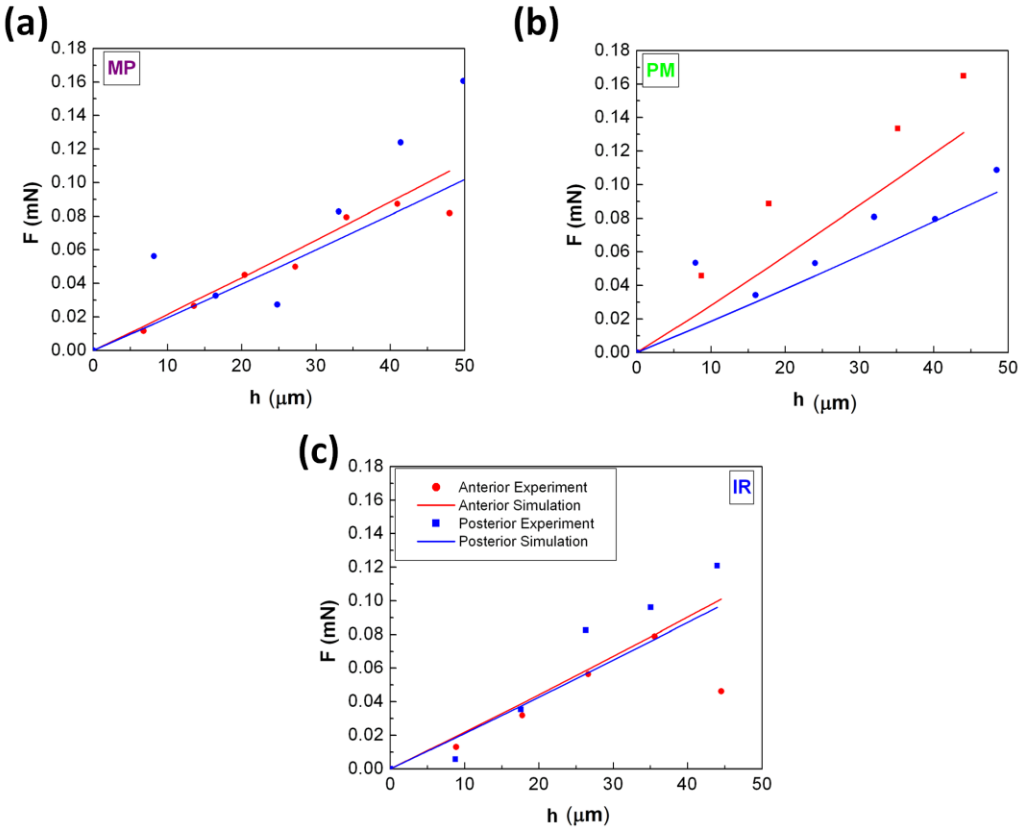

Figure 6-14 Typical experimental (solid) and simulation (outline) load- displacement curves for the anterior (red) and posterior (blue) surfaces at the (a) MP, PM (b), and IR (c) regions.

The passive mechanical behavior of the iris and the contribution of its three main components were determined through comparison between the experimental and FE results (Figure 6-13). The average modulus for the dilator, sphincter, and stroma for three porcine irides were calculated to be 1.43 ± 0.88, 0.33 ± 0.60, and 1.21 ± 0.18 kPa, respectively using incompressible model. Figure 6-14 shows the typical experimental and simulation force-displacement curves during rapid indentation for the three regions: IR, MP, and PM.

6.5 Discussion

The complex mechanical behavior of the iris may not be perfectly determined in our model due to some simplifications and assumptions; however, to our knowledge this study (using the inverse method) was the first attempt to calculate the relative elastic moduli of the iris components. Using uniaxial and biaxial tests [66, 92] or performing nanoindetation tests in different locations [13, 93], gave us a better understanding of the overall mechanical properties of the iris. Characterizing of the constituent components, however, represents an important next step in understanding the complex architecture of the iris. Specifically, characterization of the dilator can help us to understand the mechanism behind IFIS. Floppiness of the iris and poor pupil dilation are due to a weakening of the dilator muscle in IFIS, which enforces the idea that iris heterogeneity plays an important role in the overall behavior of the iris.

Attempts to characterize the mechanical properties of the iris during indentation experiments have several limitations, and include potentially inappropriate assumptions. The simplifications and assumptions used in this study are reviewed in the subsequent paragraphs.

1- **Anisotropy of the tissue:** as discussed in Chapter 1, the dilator and sphincter muscles are aligned in the radial and azimuthal direction, respectively. However, the elastic moduli were extracted from indentation which was performed perpendicular to the surfaces of samples. Our simulations did not account for such anisotropy of the tissue.

2- **Variability of iris geometry:** The contour of the iris and location of each component are different from sample to sample. Due to the difficulty of taking histology images for samples, we created only one 3D model which was used for all three samples. It would be more accurate to image each sample and create its own FE model. Moreover, histology images may not be the perfect technique to determine the accurate dimensions of the porcine iris components (particularly the dilator muscle) since the posterior side of the tissue is mostly covered by a pigmented epithelium layer, which makes it difficult to compute an accurate average measurement of the dilator thickness. Future studies are necessary to assess a successful method to remove the pigmented epithelia cells and obtain more accurate histology images of the detailed structure of the iris.

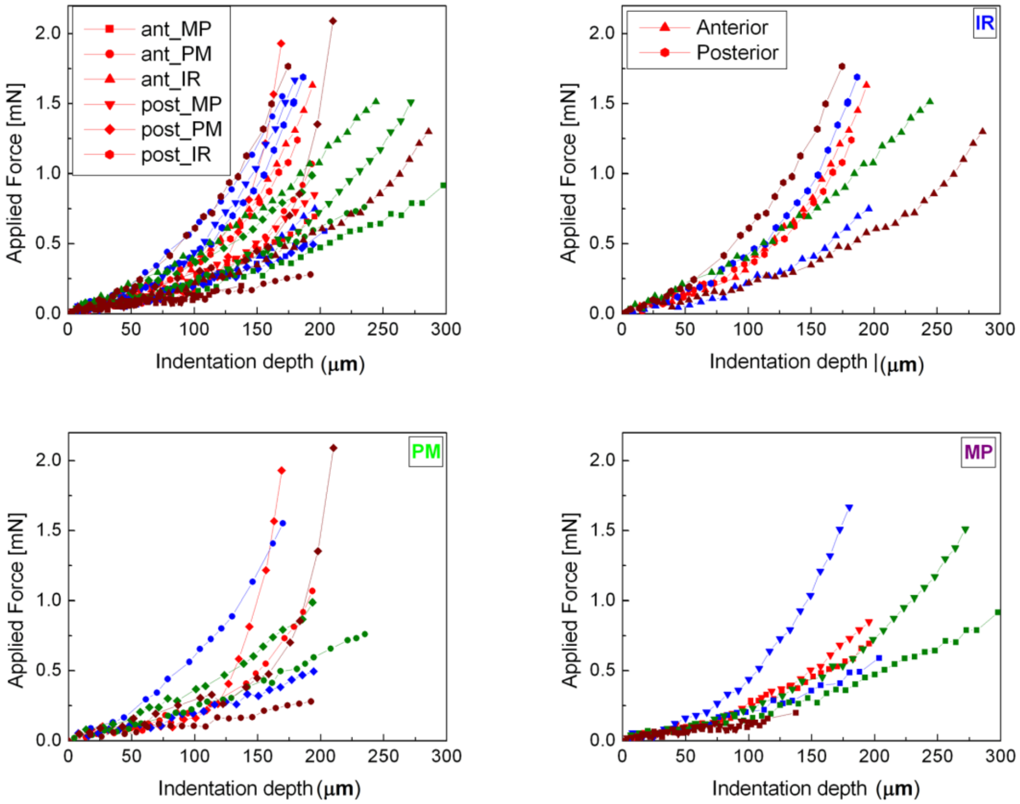

Figure 6-15 (a) Applied force-displacement curves for 4 sample porcine irides where different colors represent different sample. Force-displacement curves for 4 samples of (b) iris root (**IR**), (c) pupillary margin (**PM**), and (d) mid periphery (**MP**) regions.

3- Indentation technique: Nanoindentation has become a widely used technique to characterize the mechanical properties of various biomaterial and tissues from load-displacement measurements. The advantage of indentation in determining the mechanical properties of heterogeneous samples nondestructively makes it a suitable technique for this study. However, recent studies indicate that the indentation results strongly depend on the shape of the indenter and are less sensitive to penetration depth [105, 106]. Specifically, Simha et al. [106] showed that the elastic modulus measured using nanoindentation depends on the indenter size. In that study, different conical and cylindrical indenter tips ranging from 5 μm to 4 mm in diameter were used to examine the dependency of the equilibrium elastic modulus of cartilage on tip size. They reported that the equilibrium elastic modulus of bovine patellar cartilage increased monotonically with decreasing tip size, and postulated that their results were probably due to the inhomogeneous structure of the specimens. The modulus obtained from the 2 mm and 4 mm tips were (0.63 ± 0.23 MPa) but different when 5 μm and 90 μm diameter tips were used, and average values of 2.3 ± 0.22 MPa were calculated. The goal of our study, however, was to determine a relationship between the elasticity and assess relative contributions of each component of the iris. Dividing the iris samples into three regions during indentation tests have the advantage of obtaining useful information regarding the different components of the iris, as different force-displacement were obtained for each region.

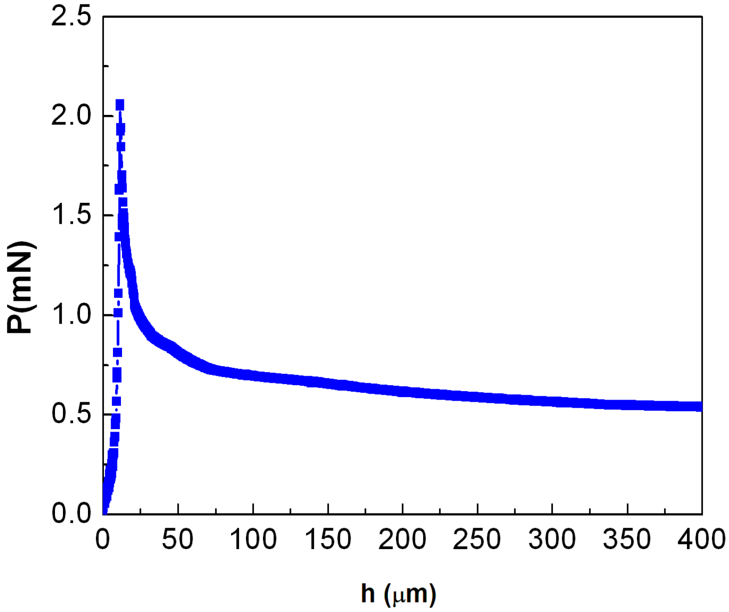

Figure 6-16 An initial sharp fall in force during the indention stress relaxation demonstrates poroelastic behavior of the tissue

4- Material behavior of iris components: In this study, a neo-Hookean material model was used to capture the large stress-strain deformation of the iris. However, as discussed in Chapter 1, several clinical studies [15, 16] suggested viscoelastic/poroelastic behavior of the iris [15]. The nature of the stroma (i.e. a loose connective tissue with incomplete layers of fibroblasts) allows the fluid to move in and out of the iris during iris movement. Moreover, in this study, an initial sharp fall in the force during the indentation stress relaxation data could be the result of exudation of fluid from the tissue (Figure 6-16). One of the challenges in simulating the stroma is, however, obtaining accurate measurements of the permeability of the iris tissue.

While these limitations and assumptions were important in this study, both experiment and simulation results suggested that the iris dilator, sphincter, and pigment epithelium on the posterior surface are significantly stiffer than the stroma located on the anterior surface. That the mechanical properties of the iris vary spatially play an important role in understanding the natural behavior of the iris. The posterior surface of the iris was found to be slightly stiffer than the anterior side, emphasizing the importance of the dilator muscle in certain ocular disease. For example, in IFIS, the perceived floppiness may not be due to a weakening of the entire iris but rather a degradation of the dilator muscle. Our results suggest that the dilator and sphincter play significant roles in determining iris flexibility whereas the effects of the stroma may be negligible due to its greater compliance.

Chapter 7 Conclusions and Future Work

7.1 Conclusions

The number of people with iris contour abnormalities such as angle closure glaucoma (ACG) necessitates improving the diagnosis and treatment of ocular diseases. As a result, many experimental studies have been devoted to understanding iris mechanics, which plays an important role in these diseases. Clinical studies have identified several anatomical risk factors associated with ACG, and in patients at risk, changes in iris configuration caused by pupil dilation could potentially lead to ACG. The mechanism and its effects on changes in iris contour, however, are still poorly understood. The objectives of my research was to investigate the iris configuration during several ocular phenomena and to examine the effect of the iris elastic response, hydrodynamics of the aqueous humor, and activity of the iris muscles on the iris profile. In this work, we developed a dynamic model for the anterior segment of the eye that accounts for anatomical factors as well as mechanical properties of the iris.

In the study of dynamic analysis of the anterior segment under graded illumination, significant changes of iris volume and cross-sectional area demonstrated that the extracellular fluid can move easily out of and into the iris. Insignificant change of anterior chamber volume and cross-sectional area supported the idea of dynamic pupillary block, in which the motion of the iris changes the equilibrium volumes of the anterior and posterior chambers. This study demonstrated our ability to quantify the geometry of the anterior segment during dilation and constriction. This experimental study, as well as several clinical studies, has emphasized the importance of three anatomical and physiological factors (dilator thickness, dynamic pupillary block, and iris compressibility) in regards to changes in iris configuration and anterior chamber angle (ACA) during pupil dilation and constriction.

Our axisymmetric computational model of the anterior segment was modified to investigate the effects of the three anatomical and physiological factors (dilator thickness, dynamic pupillary block, and iris compressibility) on the iris contour and AOD500 during dilation by creating a full factorial study. Our simulations predicted the most dramatic change in AOD500 would occur when the dilator was modeled as a thin layer in the posterior surface of an incompressible iris, and in the presence of pupillary block. The decrease in AOD500 and the iris curvature were more pronounced when the iris was incompressible and in the presence of pupillary block, respectively. Lack of significant changes in the iris volume (incompressibility) caused crowding of the peripheral iris into the trabecular meshwork and narrowing of the angle; the presence of dynamic pupillary block amplified the other effects, demonstrating a potential synergistic aspect of angle closure.

Indentation has proven to be a powerful technique to assess the iris particularly because of it small length scale. Our results stress the importance of understanding the mechanics of the iris in iris-specific disorders since the underlying pathophysiology in narrow-angle glaucoma and pigmentary glaucoma involve mechanical events. A significant difference was observed between the anterior and posterior effective moduli at all three locations. The experimental results support the hypothesis that the posterior layer is the stiffer and produces higher forces with increasing depth, showing in particular that the stroma is more compliant than the muscle tissue. Moreover, the stress-relaxation analysis revealed that the anterior surface had a shorter relaxation time than the posterior surface, perhaps due to the permeability of the stroma. This study highlighted the possible role for iris mechanics in certain ocular disease. For example, in intraoperative floppy iris syndrome (IFIS), the perceived floppiness may not be due to weakening of the entire iris but rather degradation of the dilator muscle alone. Our results suggest that the dilator and stroma play a significant role in determining iris flexibility.

7.2 Future Work

Developing an anterior-segment model for an individual subject and accounting for unique characteristics of individual patients would allow us to identify their specific problem and help doctors make better-informed treatment decisions. Medical imaging such as optical coherence topography (OCT) and ultrasound biomicroscopy (UBM) could help us to construct a precise model of an individual's anterior segment. However, prior to any further study, dealing with the resting state of iris is an important step. When medical images are taken, most likely the constituent iris muscles (sphincter and dilator) are active, and the unloaded state of the iris is not known. In order to estimate the rest state of the iris, different experiments could be performed on subjects:

- The activity of the sphincter and dilator muscle could be reduced by introducing parasympatholytic (e. g. Tropicamide) and sympathomimetic (e. g. Thymoxamine) drugs in subjects' eyes. Medical images could be taken before and after administration.
- Images of the anterior segment following the cataract surgery, when the lens is removed from the eye, would provide useful information about the state of the iris in the absence of the lens.
- Comparing the anterior segment images of subjects in light and dark conditions, we could attempt to infer the resting state of the iris.

Structural characterization of the iris is important in physiology and pathophysiology of the eye. Although combining nanoindatetion and simulation using the inversed method showed promising results in estimating the mechanical properties of the iris, the complex mechanical behavior of the iris was not adequately captured due to some simplifications and assumptions. Accounting for compressibility, viscoelasticity/poroelasticity behavior of the stroma, and the fiber direction of iris's muscles could be the next step to explore the mechanical behavior of the iris.

Bibliography

[1] J. Sebag, "The vitreous," in *Adler's Physiology of the Eye*, 9th ed., W. Hart, Ed. St. Louis: Mosby, 1992.

[2] R. Fisher. The mechanics of accommodation in relation to presbyopia. *Eye 2(6),* pp. 646-649. 1988.

[3] J. F. Koretz and G. H. Handelman, "Model of the accommodative mechanism in the human eye," *Vision Res.,* vol. 22, pp. 917-927, 1982.

[4] M. J. Hogan, J. A. Alvarado and J. E. Weddell. *Histology of the Human Eye: An Atlas and Textbook* 1971.

[5] J. S. Pepose and J. L. Ubels, "The cornea," in *Adler's Physiology of the Eye: Clinical Application,* W. M. Hart, Ed. St. Louis: Mosby-Year Book, 1992, pp. 29-70.

[6] R. A. Moses, "Intraocular pressure," in *Adler's Physiology of the Eye. 6th Edition,* R. A. Moses, Ed. St. Louis: C.V. Mosby Company, 1975, pp. 179-191.

[7] T. Shaarawy, M. B. Sherwood, R. A. Hitchings and J. G. Crowston. *Glaucoma: Expert Consult Premium Edition: Enhanced Online Features, Print, and Dvd, 2-Volume Set* 2009*2*.

[8] R. S. Carel, A. D. Korczyn, M. Rock and I. Goya, "Association between ocular pressure and certain health parameters," *Ophthalmology,* vol. 91, pp. 311-314, Apr, 1984.

[9] H. Hashemi, A. H. Kashi, A. Fotouhi and K. Mohammad, "Distribution of intraocular pressure in healthy Iranian individuals: the Tehran Eye Study," *Br. J. Ophthalmol.,* vol. 89, pp. 652-657, Jun, 2005.

[10] D. L. Epstein, "Practical aqueous humor dynamics," in *Chandler and Grant's Glaucoma*, D. L. Epstein, R. R. Allingham and J. S. Schuman, Eds. Baltimore, Maryland: Williams & Wilkins, 1997, pp. 18-24.

[11] J. Liu, D. F. Kripke, R. E. Hoffman, M. D. Twa, R. T. Loving, K. M. Rex, N. Gupta and R. N. Weinreb. Nocturnal elevation of intraocular pressure in young adults. *Invest. Ophthalmol. Vis. Sci. 39(13),* pp. 2707-2712. 1998.

[12] H. S. Thompson, "The pupil," in *Adler's Physiology of the Eye*, W. M. Hart, Ed. Chicago, IL: Mosby-Year Book, 1992, pp. 412-441.

[13] J. E. Whitcomb, R. Amini, N. K. Simha and V. H. Barocas. Anterior–posterior asymmetry in iris mechanics measured by indentation. *Exp. Eye Res. 93(4),* pp. 475-481. 2011.

[14] R. M. Santaella, J. J. Destafeno, S. S. Stinnett, A. D. Proia, D. F. Chang and T. Kim. The effect of alpha1-adrenergic receptor antagonist tamsulosin (flomax) on iris dilator smooth muscle anatomy. *Ophthalmology 117(9),* pp. 1743-1749. 2010.

[15] E. GREGERSEN. The spongy structure of the human iris; preliminary report. *Acta Ophthalmol. (Copenh) 36(3),* pp. 522-535. 1958.

[16] H. A. Quigley, D. M. Silver, D. S. Friedman, M. He, R. J. Plyler, C. G. Eberhart, H. D. Jampel and P. Ramulu. Iris cross-sectional area decreases with pupil dilation and its dynamic behavior is a risk factor in angle closure. *J. Glaucoma 18(3),* pp. 173-179. 2009.

[17] D. S. Friedman, J. Kempen, N. Congdon and J. M. Tielsch. Vision problems in the U.S.: Prevalence of adult vision impairment and age-related eye disease in america. 2007.

[18] D. L. Epstein, *Chandler and Grant's Glaucoma.* Philadephia, PA: Williams and Wilkins, 1997.

[19] J. M. Liebmann, "Ultrasound biomicroscopy of the anterior segment," *J. Glaucoma,* vol. 10, pp. S53-5, Oct, 2001.

[20] R. F. Lowe, "Aetiology of the anatomical basis for primary angle-closure glaucoma," *Br. J. Ophthalmol.,* vol. 54, pp. 161-169, 1970.

[21] R. Lavanya, M. Baskaran, R. S. Kumar, H. T. Wong, P. T. K. Chew, P. J. Foster, D. S. Friedman and T. Aung. Risk of acute angle closure and changes in intraocular pressure after pupillary dilation in asian subjects with narrow angles. *Ophthalmology* 2011.

[22] B. S. Wang, A. Narayanaswamy, N. Amerasinghe, C. Zheng, M. He, Y. H. Chan, M. E. Nongpiur, D. S. Friedman and T. Aung. Increased iris thickness and association with primary angle closure glaucoma. *Br. J. Ophthalmol. 95(1),* pp. 46-50. 2011.

[23] E. K. Woo, C. J. Pavlin, A. Slomovic, N. Taback and Y. M. Buys, "Ultrasound biomicroscopic quantitative analysis of light-dark changes associated with pupillary block," *Am. J. Ophthalmol.,* vol. 127, pp. 43-47, 1999.

[24] F. Aptel, S. Beccat, V. Fortoul and P. Denis. Biometric analysis of pigment dispersion syndrome using anterior segment optical coherence tomography. *Ophthalmology* 2011.

[25] D. L. Epstein, "Pigment dispersion and pigmentary glaucoma," in *Chandler and Grant's Glaucoma*, D. L. Epstein, R. R. Allingham and J. S. Schuman, Eds. Baltimore: Williams & Wilkins, 1997, pp. 220-231.

[26] D. F. Chang and J. R. Campbell, "Intraoperative floppy iris syndrome associated with tamsulosin," *J. Cataract Refract. Surg.,* vol. 31, pp. 664-673, Apr, 2005.

[27] D. F. Chang, R. Braga-Mele, N. Mamalis, S. Masket, K. M. Miller, L. D. Nichamin, R. B. Packard, M. Packer and ASCRS Cataract Clinical Committee, "Clinical experience with intraoperative floppy-iris syndrome. Results of the 2008 ASCRS member survey," *J. Cataract Refract. Surg.,* vol. 34, pp. 1201-1209, Jul, 2008.

[28] T. S. Prata, P. M. Palmiero, A. Angelilli, Z. Sbeity, C. G. De Moraes, J. M. Liebmann and R. Ritch, "Iris morphologic changes related to alpha(1)-adrenergic receptor antagonists implications for intraoperative floppy iris syndrome," *Ophthalmology,* vol. 116, pp. 877-881, May, 2009.

[29] R. Ursea and R. H. Silverman. Anterior-segment imaging for assessment of glaucoma. *Expert Review of Ophthalmology 5(1),* pp. 59. 2010.

[30] M. Doors, T. T. J. M. Berendschot, J. De Brabander, C. A. B. Webers and R. M. M. A. Nuijts. Value of optical coherence tomography for anterior segment surgery. *Journal of Cataract & Refractive Surgery 36(7),* pp. 1213-1229. 2010.

[31] C. A. Bruno and W. L. M. Alward. Gonioscopy in primary angle closure glaucoma. Presented at Seminars in Ophthalmology. 2002, .

[32] A. Bill and P. E. R. E. WåLINDER. The effects of pilocarpine on the dynamics of aqueous humor in a primate (macaca irus). *Invest. Ophthalmol. Vis. Sci. 5(2),* pp. 170-175. 1966.

[33] S. Nagataki and R. F. Brubaker. Effect of pilocarpine on aqueous humor formation in human beings. *Arch. Ophthalmol. 100(5),* pp. 818. 1982.

[34] D. T. L. Liu, J. S. M. Lai and D. S. C. Lam. Descemet membrane detachment after sequential argon-neodymium: YAG laser peripheral iridotomy. *Am. J. Ophthalmol. 134(4),* pp. 621-622. 2002.

[35] M. He, D. S. Friedman, J. Ge, W. Huang, C. Jin, P. S. Lee, P. T. Khaw and P. J. Foster. Laser peripheral iridotomy in primary angle-closure suspects: Biometric and gonioscopic outcomes: The liwan eye study. *Ophthalmology 114(3),* pp. 494-500. 2007.

[36] A. Nonaka, T. Kondo, M. Kikuchi, K. Yamashiro, M. Fujihara, T. Iwawaki, K. Yamamoto and Y. Kurimoto. Cataract surgery for residual angle closure after peripheral laser iridotomy. *Ophthalmology 112(6),* pp. 974-979. 2005.

[37] H. A. Quigley and A. T. Broman, "The number of people with glaucoma worldwide in 2010 and 2020," *Br. J. Ophthalmol.,* vol. 90, pp. 262-267, Mar, 2006.

[38] J. J. Heys, M. J. Taravella and V. H. Barocas, "Modeling passive mechanical interaction between the aqueous humor and iris," *J. Biomech. Eng.,* vol. 123, pp. 540-547, 2001.

[39] E. C. Huang and V. H. Barocas, "Active iris mechanics and pupillary block: steady-state analysis and comparison with anatomical risk factors," *Ann. Biomed. Eng.,* vol. 32, pp. 1276-1285, 2004.

[40] S. Dorairaj, J. M. Liebmann, C. Tello, V. Barocas and R. Ritch, "Posterior Chamber Volume Does Not Change Significantly During Dilation," *Br. J. Ophthalmol.,* Feb 4, 2009.

[41] S. K. Seah, P. J. Foster, P. T. Chew, A. Jap, F. Oen, H. B. Fam and A. S. Lim. Incidence of acute primary angle-closure glaucoma in singapore. an island-wide survey. *Arch. Ophthalmol. 115(11),* pp. 1436-1440. 1997.

[42] B. Wang, L. M. Sakata, D. S. Friedman, Y. H. Chan, M. He, R. Lavanya, T. Y. Wong and T. Aung. Quantitative iris parameters and association with narrow angles. *Ophthalmology 117(1),* pp. 11-17. 2010.

[43] C. Y. Cheung, S. Liu, R. N. Weinreb, J. Liu, H. Li, D. Y. Leung, S. Dorairaj, J. Liebmann, R. Ritch, D. S. Lam and C. K. Leung. Dynamic analysis of iris configuration with anterior segment optical coherence tomography. *Invest. Ophthalmol. Vis. Sci. 51(8),* pp. 4040-4046. 2010.

[44] F. Aptel and P. Denis. Optical coherence tomography quantitative analysis of iris volume changes after pharmacologic mydriasis. *Ophthalmology 117(1),* pp. 3-10. 2010.

[45] J. L. See, P. T. Chew, S. D. Smith, W. P. Nolan, Y. H. Chan, D. Huang, C. Zheng, P. J. Foster, T. Aung and D. S. Friedman. Changes in anterior segment morphology in

response to illumination and after laser iridotomy in asian eyes: An anterior segment OCT study. *Br. J. Ophthalmol. 91(11),* pp. 1485-1489. 2007.

[46] J. R. Karickhoff, "Reverse pupillary block in pigmentary glaucoma: follow up and new developments," *Ophthalmic Surg.,* vol. 24, pp. 562-563, Aug, 1993.

[47] C. J. Pavlin, K. Harasiewicz and F. S. Foster, "Posterior Iris Bowing in Pigmentary Dispersion Syndrome Caused by Accommodation," *Am. J. Ophthalmol.,* vol. 118, pp. 114-116, Jul 15, 1994.

[48] J. J. Heys and V. H. Barocas, "Computational Evaluation of the Role of Accommodation in Pigmentary Glaucoma," *Invest. Ophthalmol. Visual Sci.,* vol. 43, pp. 700-708, 2002.

[49] R. Amini and V. H. Barocas. Reverse pupillary block slows iris contour recovery from corneoscleral indentation. *J. Biomech. Eng. 132(7),* pp. 071010. 2010.

[50] R. Amini, J. E. Whitcomb, M. K. Al-Qaisi, T. Akkin, S. Jouzdani, S. Dorairaj, T. Prata, E. Illitchev, J. M. Liebmann, R. Ritch and V. H. Barocas. The posterior location of the dilator muscle induces anterior iris bowing during dilation, even in the absence of pupillary block. *Invest. Ophthalmol. Vis. Sci. 53(3),* pp. 1188-1194. 2012.

[51] M. D. Abràmoff, P. J. Magalhães and S. J. Ram. Image processing with ImageJ. *Biophoton Int. 11(7),* pp. 36-42. 2004.

[52] K. F. Riley, M. P. Hobson and S. J. Bence. *Mathematical Methods for Physics and Engineering* 2006.

[53] S. Liu, H. Li, S. Dorairaj, C. Y. L. Cheung, J. Rousso, J. Liebmann, R. Ritch, D. S. C. Lam and C. K. S. Leung. Assessment of scleral spur visibility with anterior segment optical coherence tomography. *J. Glaucoma 19(2),* pp. 132. 2010.

[54] A. Nonaka, T. Iwawaki, M. Kikuchi, M. Fujihara, A. Nishida and Y. Kurimoto, "Quantitative evaluation of iris convexity in primary angle closure," *Am. J. Ophthalmol.,* vol. 143, pp. 695-697, Apr, 2007.

[55] W. P. Nolan, P. J. Foster, J. G. Devereux, D. Uranchimeg, G. J. Johnson and J. Baasanhu. YAG laser iridotomy treatment for primary angle closure in east asian eyes. *Br. J. Ophthalmol. 84(11),* pp. 1255-1259. 2000.

[56] R. F. Lowe. Angle-closure, pupil dilatation, and pupil block. *Br. J. Ophthalmol. 50(7),* pp. 385-389. 1966.

[57] R. Mapstone, "Mechanics of pupil block," *Br. J. Ophthalmol.,* vol. 52, pp. 19-25, 1968.

[58] D. M. Silver and H. A. Quigley, "Aqueous flow through the iris-lens channel: estimates of differential pressure between the anterior and posterior chambers," *J. Glaucoma,* vol. 13, pp. 100-107, 2004.

[59] S. Kumar, S. Acharya, R. Beuerman and A. Palkama, "Numerical solution of ocular fluid dynamics in a rabbit eye: Parametric effects," *Ann. Biomed. Eng.,* vol. 34, pp. 530-544, Mar, 2006.

[60] A. D. Fitt and G. Gonzalez, "Fluid mechanics of the human eye: aqueous humour flow in the anterior chamber," *Bull. Math. Biol.,* vol. 68, pp. 53-71, Jan, 2006.

[61] R. Amini, S. Jouzdani and V. H. Barocas. Increased iris-lens contact following spontaneous blinking: Mathematical modeling. *J. Biomech. 45(13),* pp. 2293-2296. 2012.

[62] G. Marchini, A. Pagliarusco, A. Toscano, R. Tosi, C. Brunelli and L. Bonomi, "Ultrasound Biomicroscopic and Conventional Ultrasonographic Study of Ocular Dimensions in Primary Angle-closure Glaucoma," *Ophthalmology,* vol. 105, pp. 2091-2098, 1998.

[63] D. A. Lee, R. F. Brubaker and D. M. Ilstrup, "Anterior chamber dimensions in patients with narrow angles and angle-closure glaucoma," *Arch. Ophthalmol.,* vol. 102, pp. 46-50, 1984.

[64] R. F. Lowe. Anterior lens curvature. comparisons between normal eyes and those with primary angle-closure glaucoma. *Br. J. Ophthalmol. 56(5),* pp. 409. 1972.

[65] C. A. Patterson and N. A. Delamere, "The lens," in *Adler's Physiology of the Eye: Clinical Application,* W. M. Hart, Ed. St. Louis: Mosby-Year Book, 1992, pp. 348-390.

[66] J. Heys and V. H. Barocas, "Mechanical characterization of the bovine iris," *J. Biomech.,* vol. 32, pp. 999-1003, 1999.

[67] B. H. Crawford. The dependence of pupil size upon external light stimulus under static and variable conditions. *Proceedings of the Royal Society of London.Series B-Biological Sciences 121(823),* pp. 376. 1936.

[68] P. Reeves. Rate of pupillary dilation and contraction. *Psychol. Rev. 25(4),* pp. 330. 1918.

[69] J. A. Scott, "A finite element model of heat transport in the human eye," *Phys. Med. Biol.,* vol. 33, pp. 227-241, 1988.

[70] P. Sackinger, P. Schunk and R. Rao, "A Newton-Raphson Pseudo-Solid Domain Mapping Technique for Free and Moving Boundary Problems: A Finite Element Implementation," *Journal of Computational Physics,* vol. 125, pp. 83-103, 1996.

[71] S. Krag and T. T. Andreassen, "Mechanical properties of the human lens capsule," *Prog. Retin. Eye Res.,* vol. 22, pp. 749-767, Nov, 2003.

[72] J. D. Brown and R. F. Brubaker, "A Study of the Relation Between Intraocular Pressure and Aqueous Humor Flow in the Pigment Dispersion Syndrome," *Opthalmology,* vol. 96, pp. 1468-1470, 1989.

[73] R. Amini, V. H. Barocas, H. P. Kavehpour and J. P. Hubschman. Computational simulation of altitude change-induced intraocular pressure alteration in patients with intravitreal gas bubbles. *Retina 31(8),* pp. 1656. 2011.

[74] C. B. Toris and C. B. Camras, "Measuring the outflow of aqueous humor," *Glaucoma Today,* pp. 15-22, 2007.

[75] A. J. Sit, C. B. Nau, J. W. McLaren, D. H. Johnson and D. Hodge. Circadian variation of aqueous dynamics in young healthy adults. *Invest. Ophthalmol. Vis. Sci. 49(4),* pp. 1473-1479. 2008.

[76] R. Amini, "Iris Biomechanics in Health and Disease," 2010.

[77] E. C. Huang and V. H. Barocas, "Accommodative microfluctuations and iris contour," *Journal of Vision,* vol. 6, pp. 653-660, 2006.

[78] C. K. Leung, C. Y. Cheung, H. Li, S. Dorairaj, C. K. Yiu, A. L. Wong, J. Liebmann, R. Ritch, R. Weinreb and D. S. Lam, "Dynamic analysis of dark-light changes of the anterior chamber angle with anterior segment OCT," *Invest. Ophthalmol. Vis. Sci.,* vol. 48, pp. 4116-4122, Sep, 2007.

[79] C. J. Pavlin, P. Macken, G. E. Trope, K. Harasiewicz and F. S. Foster, "Accommodation and Iridotomy in the Pigment Dispersion Syndrome," *Ophthalmic Surg. Lasers,* vol. 27, pp. 113-120, 1996.

[80] J. A. McWhae, R. L. Piemontesi and A. C. S. Crichton, "Letter to the Editor re: Blinking and Iris Configuration in PDS," *Ophthalmology,* vol. 103, pp. 197-199, 1996.

[81] J. F. Koretz, G. H. Handelman and N. P. Brown, "Analysis of human crystalline lens curvature as a function of accommodative state and age," *Vision Res.,* vol. 24, pp. 1141-1151, 1984.

[82] C. A. Cook and J. F. Koretz, "Acquisition of the curves of the human crystalline lens from slit lamp images: an application of the Hough transform," *Appl. Opt.,* vol. 30, pp. 2088-2099, 1991.

[83] T. Fontana and R. F. Brubaker, "Volume and depth of the anterior chamber in the normal aging human eye," *Arch. Ophthalmol.,* vol. 98, pp. 1803-1808, 1980.

[84] C. N. Karson, R. A. Dykman and S. R. Paige. Blink rates in schizophrenia. *Schizophr. Bull. 16(2),* pp. 345. 1990.

[85] W. S. Sun, R. S. Baker, J. C. Chuke, B. R. Rouholiman, S. A. Hasan, W. Gaza, M. W. Stava and J. D. Porter, "Age-related changes in human blinks. Passive and active changes in eyelid kinematics," *Invest. Ophthalmol. Vis. Sci.,* vol. 38, pp. 92-99, Jan, 1997.

[86] S. Dorairaj, C. Oliveira, A. K. Fose, J. M. Liebmann, C. Tello, V. H. Barocas and R. Ritch, "Accommodation-induced changes in iris curvature," *Exp. Eye Res.,* vol. 86, pp. 220-225, Feb, 2008.

[87] S. D. Potash, C. Tello, J. Liebmann and R. Ritch, "Ultrasound Biomicroscopy in Pigment Dispersion Syndrome," *Ophthalmology,* vol. 101, pp. 332-339, 1994.

[88] L. Liu. Anatomical changes of the anterior chamber angle with anterior-segment optical coherence tomography. *Arch. Ophthalmol. 126(12),* pp. 1682-1686. 2008.

[89] R. Ritch, "Pigment dispersion syndrome - update 2003," in *Glaucoma*, F. Grehn and R. Stamper, Eds. Berlin: Springer-Verlag, 2004, pp. 177-192.

[90] N. Niyadurupola and D. C. Broadway. Pigment dispersion syndrome and pigmentary glaucoma–a major review. *Clin. Experiment. Ophthalmol. 36(9),* pp. 868-882. 2008.

[91] Y. Lei, K. Zhang, C. Chen, H. Song, H. Cao and Z. Liu. Experimental research on the biomechanical properties of the porcine iris. Presented at World Congress on Medical Physics and Biomedical Engineering 2006. 2007, .

[92] J. E. Whitcomb, V. A. Barnett, T. W. Olsen and V. H. Barocas. Ex vivo porcine iris stiffening due to drug stimulation. *Exp. Eye Res. 89(4),* pp. 456-461. 2009.

[93] L. Yoo, J. Reed, A. Shin, J. Kung, J. K. Gimzewski, V. Poukens, R. A. Goldberg, R. Mancini, M. Taban and R. Moy. Characterization of ocular tissues using microindentation and hertzian viscoelastic models. *Invest. Ophthalmol. Vis. Sci. 52(6),* pp. 3475-3482. 2011.

[94] I. E. Loewenfeld and D. A. Newsome, "Iris mechanics. I. Influence of pupil size on dynamics of pupillary movements," *Am. J. Ophthalmol.,* vol. 71, pp. 347-362, Jan, 1971.

[95] H. Tabandeh, G. M. Thompson, C. Kon and T. Bolton, "Phenylephrine and pilocarpine in the treatment of post-operative irido-corneal adhesion," *Eye,* vol. 9, pp. 452-455, 1995.

[96] K. Yamaji, T. Yoshitomi, S. Usui and Y. Ohnishi, "Mechanical properties of the rabbit iris smooth muscles," *Vision Res.,* vol. 43, pp. 479-487, Feb, 2003.

[97] D. M. Ebenstein and L. A. Pruitt. Nanoindentation of soft hydrated materials for application to vascular tissues. *J. Biomed. Mater. Res. A. 69(2),* pp. 222-232. 2004.

[98] M. L. Oyen and R. F. Cook. A practical guide for analysis of nanoindentation data. *Journal of the Mechanical Behavior of Biomedical Materials 2(4),* pp. 396-407. 2009.

[99] B. Briscoe, K. Sebastian and M. Adams. The effect of indenter geometry on the elastic response to indentation. *J. Phys. D 27*pp. 1156. 1994.

[100] S. Chiravarambath, N. K. Simha, R. Namani and J. L. Lewis. Poroviscoelastic cartilage properties in the mouse from indentation. *J. Biomech. Eng. 131(1),* pp. 011004. 2009.

[101] W. Hayes, L. Keer, G. Herrmann and L. Mockros. A mathematical analysis for indentation tests of articular cartilage. *J. Biomech. 5(5),* pp. 541-551. 1972.

[102] J. K. Suh and M. DiSilvestro. Biphasic poroviscoelastic behavior of hydrated biological soft tissue. *Journal of Applied Mechanics 66(2),* pp. 528-535. 1999.

[103] K. D. Costa and F. C. Yin, "Analysis of indentation: implications for measuring mechanical properties with atomic force microscopy," *J. Biomech. Eng.,* vol. 121, pp. 462-471, Oct, 1999.

[104] E. U. Azeloglu, G. Kaushik and K. D. Costa. Developing a hybrid computational model of AFM indentation for analysis of mechanically heterogeneous samples. Presented at Engineering in Medicine and Biology Society, 2009. EMBC 2009. Annual International Conference of the IEEE. 2009, .

[105] P. Parakala, R. A. Mirshams, S. Nasrazadani and K. Lian. Effects of thickness and indenter geometry in nanoindentation of nickel thin films. Presented at MATERIALS RESEARCH SOCIETY SYMPOSIUM PROCEEDINGS. 2004, .

[106] N. K. Simha, H. Jin, M. L. Hall, S. Chiravarambath and J. L. Lewis, "Effect of indenter size on elastic modulus of cartilage measured by indentation," *J. Biomech. Eng.,* vol. 129, pp. 767-775, Oct, 2007.

[107] M. A. Mandell, C. J. Pavlin, D. J. Weisbrod and E. R. Simpson. Anterior chamber depth in plateau iris syndrome and pupillary block as measured by ultrasound biomicroscopy. *Am. J. Ophthalmol. 136(5),* pp. 900-903. 2003.

[108] L. R. Ritch R, "Angle-closure glaucoma: mechanisms and epidemiology. *The glaucomas,* chapter 37," 1996.

[109] Y. Yamamoto, T. Uno, K. Shisida, L. Xue, A. Shiraishi, X. Zheng and Y. Ohashi, "Demonstration of aqueous streaming through a laser iridotomy window against the corneal endothelium," *Arch. Ophthalmol.,* vol. 124, pp. 387-393, Mar, 2006.

[110] C. Hong, K. H. Park, S. -. Hyung, K. Y. Song, D. M. Kim and D. H. Youn, "Evaluation of pupillary block component in angle-closure glaucoma," *Jpn. J. Ophthalmol.,* vol. 40, pp. 239-245, 1996.

[111] J. M. Liebmann, C. Tello, S. J. Chew, H. Cohen and R. Ritch, "Prevention of blinking alters iris configuration in pigment dispersion syndrome and in normal eyes," *Ophthalmology,* vol. 102, pp. 446-455, Mar, 1995.

[112] R. Amini, J. E. Whitcomb, T. S. Prata, S. Dorairaj, J. M. Liebmann, R. Ritch and V. H. Barocas. Quantification of iris concavity. *Journal of Ophthalmic & Vision Research 5(3),* pp. 211-212. 2010.

[113] M. K. Al-Qaisi and T. Akkin. Swept-source polarization-sensitive optical coherence tomography based on polarization-maintaining fiber. *Optics Express 18(4),* pp. 3392-3403. 2010.

[114] S. Yun, G. Tearney, J. de Boer, N. Iftimia and B. Bouma. High-speed optical frequency-domain imaging. *Opt. Express 11(22),* pp. 2953-2963. 2003.

[115] P. R. Amestoy, I. S. Duff and J. -. L'Excellent, "Multifrontal parallel distributed symmetric and unsymmetric solvers," *Comput. Methods Appl. Mech. Eng.,* vol. 184, pp. 501-520, 2000.

[116] A. Heijl, M. C. Leske, B. Bengtsson, L. Hyman, B. Bengtsson and M. Hussein. Reduction of intraocular pressure and glaucoma progression: Results from the early manifest glaucoma trial. *Arch. Ophthalmol. 120(10),* pp. 1268. 2002.

[117] R. N. Weinreb and P. T. Khaw. Primary open-angle glaucoma. *The Lancet 363(9422),* pp. 1711-1720. 2004.

[118] M. C. Leske, A. Heijl, M. Hussein, B. Bengtsson, L. Hyman and E. Komaroff. Factors for glaucoma progression and the effect of treatment: The early manifest glaucoma trial. *Arch. Ophthalmol. 121(1),* pp. 48. 2003.

[119] B. Bengtsson and A. Heijl. Diurnal IOP fluctuation: Not an independent risk factor for glaucomatous visual field loss in high-risk ocular hypertension. *Graefe's Archive for Clinical and Experimental Ophthalmology 243(6),* pp. 513-518. 2005.

[120] C. Tello, H. V. Tran, J. Liebmann and R. Ritch. Angle closure: Classification, concepts, and the role of ultrasound biomicroscopy in diagnosis and treatment. Presented at Seminars in Ophthalmology. 2002, .

[121] K. Matsunaga, K. Ito, K. Esaki, K. Sugimoto, T. Sano, K. Miura, M. Sasoh and Y. Uji, "Evaluation and comparison of indentation ultrasound biomicroscopy gonioscopy in relative pupillary block, peripheral anterior synechia, and plateau iris configuration," *J. Glaucoma,* vol. 13, pp. 516-519, Dec, 2004.

[122] M. Forbes, "Gonioscopy with corneal indentation: a method for distinguishing between appositional closure and synechial closure," *Arch. Ophthalmol.,* vol. 76, pp. 488-492, 1966.

[123] H. Ishikawa, K. Inazumi, J. M. Liebmann and R. Ritch, "Inadvertent corneal indentation can cause artifactitious widening of the iridocorneal angle on ultrasound biomicroscopy," *Ophthalmic Surg. Lasers,* vol. 31, pp. 342-345, Jul-Aug, 2000.

[124] R. Ritch, "A unification hypothesis of pigment dispersion syndrome," *Trans. Am. Ophthalmol. Soc.,* vol. 94, pp. 381-405; discussion 405-9, 1996.

[125] R. Amini and V. H. Barocas. Anterior chamber angle opening during corneoscleral indentation: The mechanism of whole eye globe deformation and the importance of the limbus. *Invest. Ophthalmol. Vis. Sci. 50(11),* pp. 5288-5294. 2009.

[126] C. C. Collins, "Miniature Passive Pressure Transensor for Implanting in the Eye," *IEEE Trans Bio-Medical Eng,* vol. 14, pp. 74-83, 1967.

[127] C. L. Percicot, C. R. Schnell, C. Debon and C. Hariton, "Continuous intraocular pressure measurement by telemetry in alpha-chymotrypsin-induced glaucoma model in the rabbit: Effects of timolol, dorzolamide, and epinephrine," *J. Pharmacol. Toxicol. Methods,* vol. 36, pp. 223-228, 1996.

[128] F. N. Kanadani, S. Dorairaj, A. M. Langlieb, W. A. Shihadeh, C. Tello, J. M. Liebmann and R. Ritch. Ultrasound biomicroscopy in asymmetric pigment dispersion syndrome and pigmentary glaucoma. *Arch. Ophthalmol. 124(11),* pp. 1573. 2006.

[129] C. Pavlin, K. Harasiewicz and F. Foster, "Ultrasound Biomicroscopy of Anterior Segment Structures in Normal and Glaucomatous Eyes," *Am J Ophth,* vol. 113, pp. 381-389, 1992.

[130] K. C. Yoon, L. D. Won, H. J. Cho and K. J. Yang. Ultrasound biomicroscopic changes after laser iridotomy or trabeculectomy in angle-closure glaucoma. *Korean Journal of Ophthalmology 18(1),* pp. 9-14. 2004.

Appendix A- The Posterior Location of the Dilator Muscle Induces Anterior Iris Bowing during Dilation Even in the Absence of Pupillary Block

(This work was part of the paper “The Posterior Location of the Dilator Muscle Induces Anterior Iris Bowing during Dilation, Even in the Absence of Pupillary Block” by R. Amini, J.E. Whitcomb, M.K. Al-Qaisi, T. Akkin, S. Jouzdani, T.S. Prata, S. Dorairaj, J.M. Liebmann, R. Ritch and V.H. Barocas, (Invest Ophthalmol Vis Sci. 2012;53:1188–1194) DOI:10.1167/iovs.11-8408 (American Society of Mechanical Engineers as the copyright holder is acknowledged)

A.1 Summary

In vivo and *ex vivo* experiments were performed in combination with an *in silico* computational model to show how the posterior location of the dilator leads to iris anterior bowing during dilation even in the absence of AH pressure. Iris anterior curvature was measured *in vivo* before and after dilation by time-domain slit lamp optical coherence tomography (SL-OCT). All patients (n = 7) had previously had LPI to eliminate any pupillary block due to primary ACG. In the *ex vivo* experiments, isolated porcine irides (n = 30) were secured at the periphery and immersed in an oxygenated Krebs-Ringer buffer. Dilation was induced pharmaceutically by the addition of 2.5% phenylephrine and 1% tropicamide. Iris images were taken before and after dilation using an in-house OCT system. A FE model was also developed based on typical geometry of

the iris from the initial OCT image. The iris was modeled as a neo-Hookean solid, and the active muscle component was applied only to the region specified as the dilator.

An increase in curvature and a decrease in the chord length after dilation were observed in both experiments. In both the *in vivo* and *ex vivo* experiments, the curvature to chord length ratio increased significantly during dilation. Computer simulations agreed well with the experimental results only when the proper anatomical position of dilator was used.

We conclude that the posterior location of the dilator contributes to the anterior iris bowing via a non-pupillary block dependent mechanism.

A.2 Introduction

Anterior bowing of the iris, resulting in a narrow or closed angle, is often attributed to pupillary block[54, 107, 108] even though it is recognized that the angle can close by multiple mechanisms, some independent of pupillary block. In particular, the mechanism by which the iris bows anteriorly during dilation [23] is unclear. We have shown theoretically [39] that the pressure increase from blocking the steady flow of aqueous cannot explain the increased anterior bowing when the pupil dilates, and Woo et al. [23] reported that the anterior bowing during dilation occurs within seconds, far too quickly for AH to build up in the posterior chamber. Yamamoto et al. [109] reported that when rabbits with a LPI were dilated, the aqueous flowed posteriorly, not anteriorly, which would imply that the anterior-chamber pressure was, in fact, higher. In some cases, LPI does not lead to opening of the angle, and following dilation, the angle can still narrow and the iris can still bow forward considerably [35, 36, 110]. Taken together, these observations require that non-pupillary-block mechanisms for anterior iris bowing, especially during dilation, be considered. In this paper, we explore the hypothesis that the anatomy of the iris, specifically the posterior position of the dilator muscle within the iris, contributes to spontaneous anterior curvature of the iris during dilation independent of pupillary block.

A.3 Methodology

This work included three parallel studies:

- *In vivo* experiments, in which the curvature of the iris was measured before and after dilation for a set of subjects, all of whom had had LPIs, eliminating any pupillary block.
- *Ex vivo* experiments, in which the isolated porcine iris was dilated pharmacologically and imaged via OCT to determine the iris contour.
- *In silico* computer simulations, in which the *ex vivo* experiments were modeled using realistic geometry and dilator placement.

A.3.1 *In Vivo* Experiments

All patients had been diagnosed previously with anatomically narrow-angles (ANA) and primary ACG. Patients diagnosed with ANA who underwent LPI surgery to open the angle were imaged by SL-OCT in light and dark conditions. Institutional review board approval was obtained, as was written informed consent for all subjects. At the time of imaging, all subjects' angles were noted to be open. The SL-OCT system (Heidelberg Engineering, GmbH, Dossenheim, Germany) had an optical axial image resolution <25 µm and a lateral resolution of 20-100 µm. Initially, five high-quality cross-sectional images were taken from each subject in dark conditions while in the sitting position. Subsequently, images were acquired under standardized lighting conditions (300 lux), using a 5 x 1 mm light beam set at the maximum intensity of the device. Subjects were instructed to blink normally and to fixate with the non-imaged eye on a target 1 meter from the device to minimize accommodation artifact. All images were taken horizontally through the center of the pupil to avoid interference with the lid margins, and iris crypts were avoided whenever possible. Quality control parameters were defined as a well-centered image, a clearly defined scleral spur, and the absence of artifacts. Patients diagnosed with exfoliation syndrome, uveitis, or pigmentary glaucoma, were excluded, as were those with previous intraocular surgery. Patients who were on systemic α-1 adrenergic receptor antagonists (such as Flomax) or on topical medications known to alter the iris configuration [14, 28] were also excluded. Whenever both eyes were eligible, one randomly selected eye was. The study was conducted in accordance with the ethical standards stated in the 1964 Declaration of Helsinki and was approved by the Institutional Review Board (IRB).

Images were analyzed using the ImageJ software available from NIH (National Institutes of Health, Maryland) [51]. Chord length [23], iris curvature [111], and iris concavity ratio [112] were calculated. Positive curvature indicates anterior bowing (concavity) whereas negative curvature reflects posterior bowing. The iris concavity ratio, as described previously, is defined as the ratio of iris curvature to chord length, which has the advantage of being a scale-invariant measure of curvature [112]. Results were compared using a two-sided paired t-test assuming equal variance.

A.3.2 *Ex Vivo* Experiments

Experiments were performed on 30 isolated porcine irides and were in compliance with the ARVO statement for use of animals in ophthalmic and vision research. The irides were tested within 2-6 hours post mortem and prepared as described previously [92]. The isolated irides were pinned at two locations on the periphery of the tissue in a Petri dish with a silicone-based polymer lining (Figure A-1).

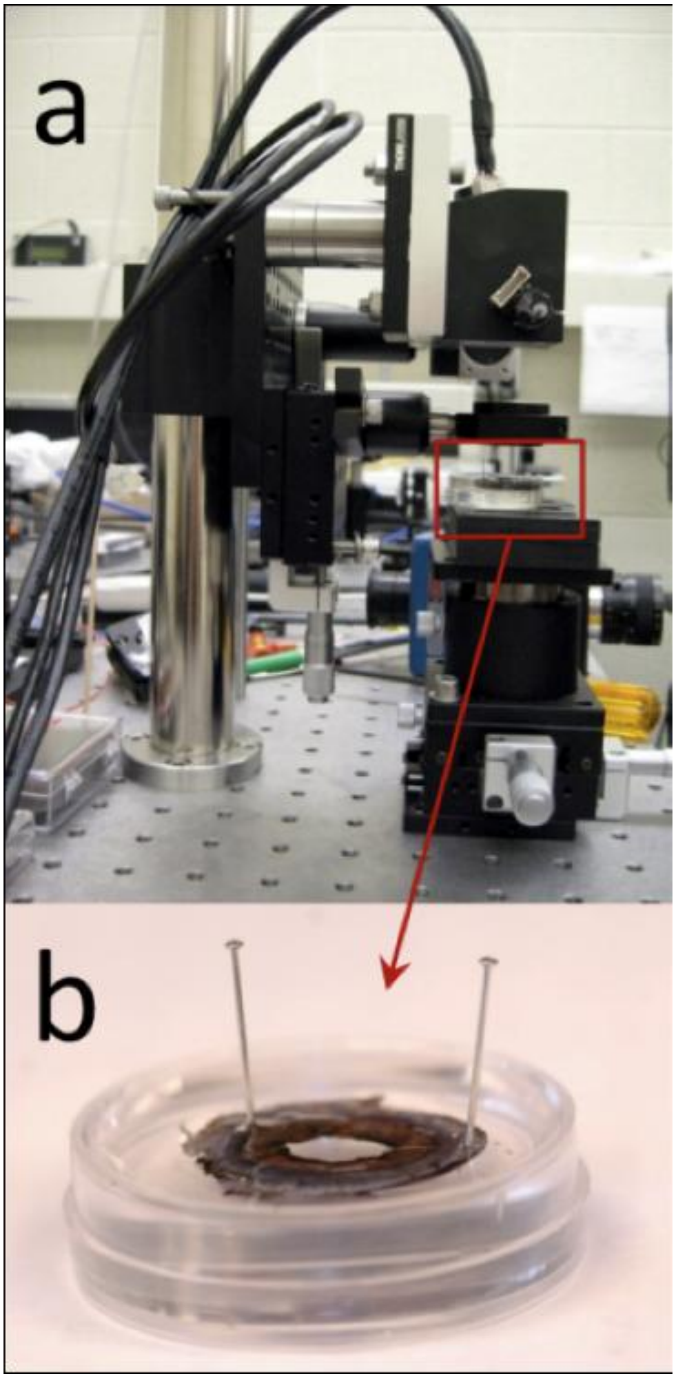

Figure A-1 Ex Vivo Experimental Setup.

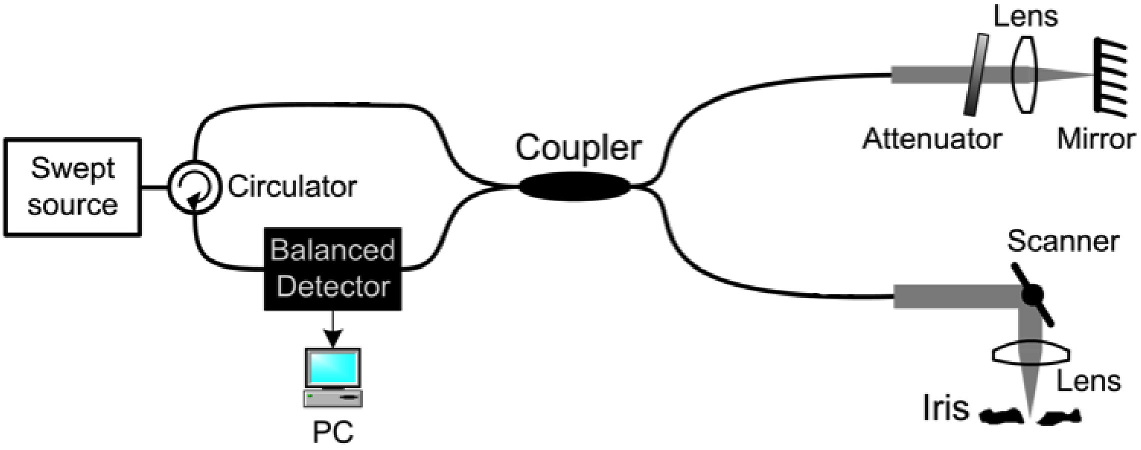

Figure A-2 Representation of the OCT system used to image the iris during dilation.

The irides were immersed at room temperature in a 5 mL bath of oxygenated Krebs-Ringer buffer to maintain a physiological pH of 7.4. Before dilation, reference images of the iris were taken via the fiber-based swept-source OCT system [113] shown schematically in Figure A-2.

The system operated in the Fourier domain, by which modulations on the optical spectrum were related to the spatial information along a depth profile called an A-line [114]. After the initial image was captured, the irides were dilated pharmaceutically by addition of 40 µL of 2.5% phenylephrine and 40 µL of 1% tropicamide solutions. Images of the dilated iris were taken every 40 seconds for 10-15 minutes. The initial and final images were analyzed using ImageJ (National Institutes of Health, Maryland)[51] to calculate the change in pupil diameter, chord length (AB), curvature (CD), and the concavity ratio (CD/AB). These measurements are described in Figure A-3a. Iris cross-sectional area (the nasal and temporal iris) were traced manually via a custom ImageJ macro and, and their areas and centroids were calculated before and after dilation. The center of the pupil was defined as the midpoint of the line segment joining the centroids of nasal and temporal iris cross-sectional areas and the corneal axis as perpendicular line passed through the pupil center. The volume of the iris (both nasal and temporal) was calculated using Equation 3-1. Results were compared using a two-sided paired t-test assuming equal variance.

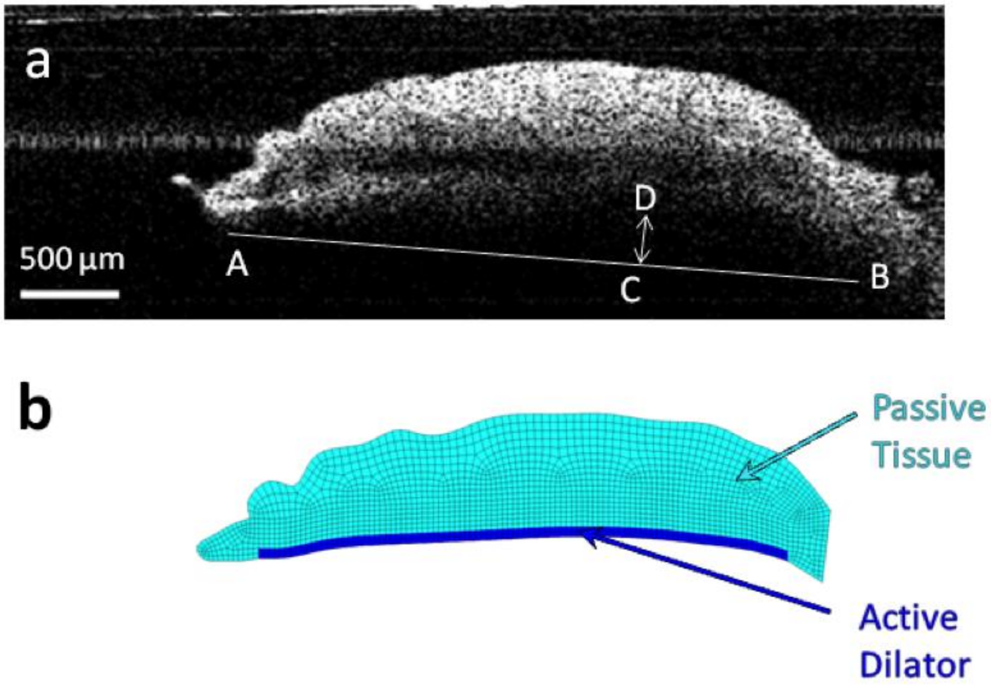

Figure A-3 (a) OCT image of the iris before dilator is activated. (b) FE model based on the OCT image of the iris before dilation.

A.3.3 *In Silico* Studies

A realistic FE mesh of the iris was constructed based on the initial OCT image of the non-dilated iris (Figure A-3b). The dilator muscle is a very thin radially-aligned smooth muscle located on the posterior surface of the iris. The dilator extends centrally to the midpoint of sphincter muscle. For humans, the average thickness of the dilator is 4.0-8.5 μm [4, 14], whereas in the porcine model the average dilator thickness is 26 μm [13].

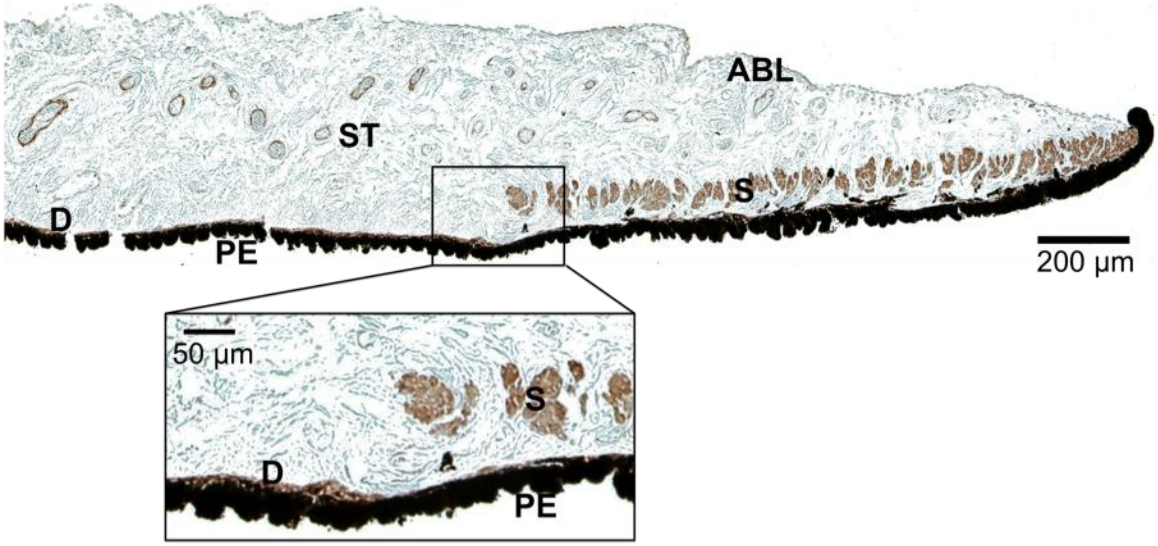

Figure A-4 Histological image of the pupillary and mid-peripheral portions of the porcine iris.

We placed the dilator muscle in the posterior portion of the iris based on histological analysis of the porcine iris (Figure A-4). The iris was modeled as a nearly incompressible neo-Hookean solid [38] governed by the static stress balance:

A-1

where σ was the Cauchy stress tensor, and derivatives of the stress were with respect to the current coordinate system. The Cauchy stress tensor was defined by neo-Hookean, , and active dilator, , contributions:

A-2

The neo-Hookean stress was defined by

A-3

where was the shear modulus, ν the Poisson's ratio, the identity tensor, the deformation gradient, and the left Cauchy-Green deformation tensors, in which and were defined as follows:

A-4

A-5

with being the current position of a material point, being its rest position.

The iris shear modulus (= 9 kPa) and Poisson’s ratio (ν = 0.49) were set based on our previous studies [66]. The dilator term was applied only in the dilator region (represented by a darker color in Figure A-3b). To ensure that the muscle contraction was always in the direction of the non-deformed dilator muscle, it was define by , the scalar muscle contraction stress, and , the unit vector representing the direction of non-deformed dilator muscle:

A-6

The Galerkin FE method was employed for spatial discretization of the mathematical model. GAMBIT (Fluent Inc., Lebanon, NH) mesh generation software was used to generate the FE mesh. The nonlinear algebraic equation system was solved using Newton-Raphson iteration and the direct solver MUMPS [115].

The model was used to simulate spontaneous contraction of the dilator muscle *ex vivo*, based on the experiments described above. The pupil diameter was increased from 5.0 mm to 7.0 mm by applying a muscle contraction stress . To assess the importance of the location of the dilator muscle, three simulations were performed. In the first case, the dilator muscle was located in the posterior iris based on the histological porcine images. In the second case, the dilator layer was artificially positioned more anteriorly. Finally, in the third case, the entire thickness of the iris was modeled as the active dilator muscle. In all three cases, the iris chord length, and the iris curvature (Figure A-3a) were calculated from the model.

A.4 Results

A.4.1 *In Vivo* Experiments

We examined seven patients diagnosed with ANA and/or ACG; patient details are given in Table A.1. The measurements for the patients are shown in Figure A-5. The pupil diameter (Figure A-5a) was 2.73 ± 0.39 mm in the light and increased to 4.71 ± 0.55 mm ($p < 0.001$) in the dark (mean ± 95% CI, $n = 7$). The iris chord length (Figure A-5b) decreased significantly from 5.18 ± 0.35 mm to 4.23 ± 0.37 mm ($p < 0.0001$). Both the curvature and concavity ratio increased, but only the concavity ratio increased significantly. The curvature (Figure A-5c) increased from 0.13 ± 0.09 mm to 0.16 ± 0.02

mm (p = 0.481) and the concavity ratio (Figure A-5d) from 0.026 ± 0.01 to 0.04 ± 0.01 (p = 0.004), including a significant change in shape due to the combination of chord length and curvature changes.

Table A-1 ANA patient information.

Gender	Race	Age	Diagnosis	Eye	Refractive Erro		IOP (mmHg)	
					OD	OS	OD	OS
F	C	68	ACG	OS	+2.75	+2.50	15	15
M	C	66	ACG	OD	+2.50	+2.00	15	16
M	H	62	ACG	OD	-2.00	-1.50	15	17
F	C	50	ANA	OD	-7.75	-7.75	14	15
M	C	47	ANA	OU	+1.25	+1.50	14	14
M	C	58	ACG	OD	-0.75	-1.00	15	16
M	H	60	ANA	OD	+1.00	+0.75	19	19

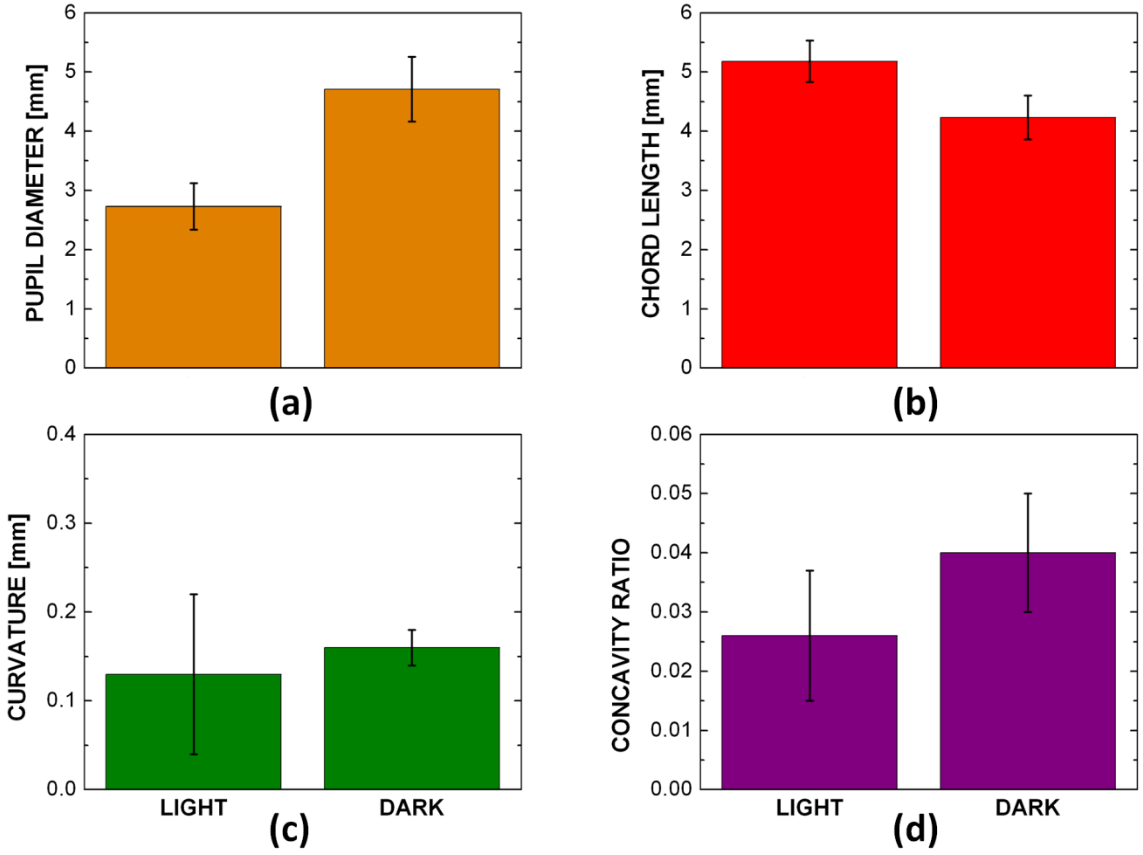

Figure A-5 *In vivo* ANA patients' iris chord length, curvature, and concavity ratio results.

A.4.2 *Ex Vivo* Experiments

Figure A-6 shows a pinned porcine iris before (a) and after (b) dilation. The pupil diameter increased in the experiment, indicating that there was still activation of the dilator muscle (phenylephrine) and possibly relaxation of the sphincter muscle (tropicamide). The bar graph in Figure A-7a shows that the pupil diameter increased from 2.82 ± 0.16 mm (mean ± 95% CI, n = 30) to 3.72 ± 0.21 mm ($p < 0.001$) after the addition of the 40 µL of 2.5% phenylephrine and 40 µL of 1% tropicamide. The iris chord length (Figure A-7b) decreased from 1.43 ± 0.11 mm to 1.12 ± 0.09 mm ($p < 0.0001$) following activation of the dilator muscle. The iris curvature also changed following dilation (Figure A-7c), increasing from 0.12 ± 0.01 mm to 0.20 ± 0.02 mm ($p < 0.002$). The concavity ratio also changed significantly (Figure A-7d), increasing from 0.09 ± 0.01 to 0.21 ± 0.02 ($p < 0.0001$) following drug-induced dilation. These results were all consistent with the *in vivo* experiments.

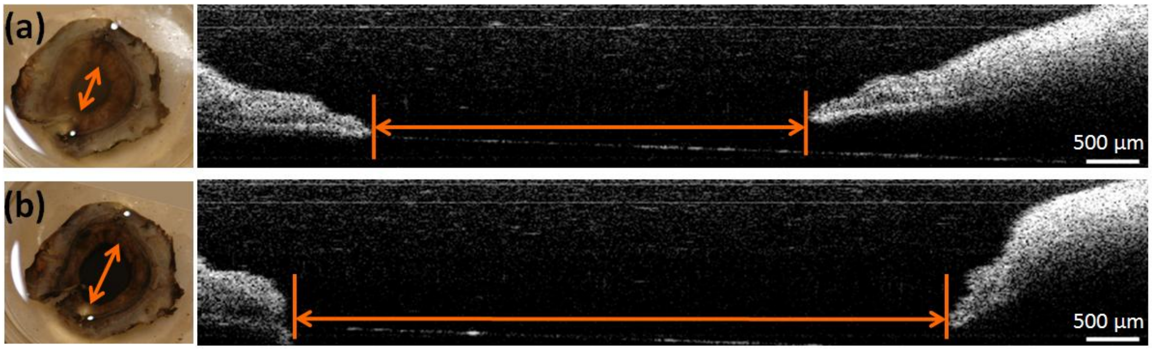

Figure A-6 Ex Vivo Pupil Dilation Results.

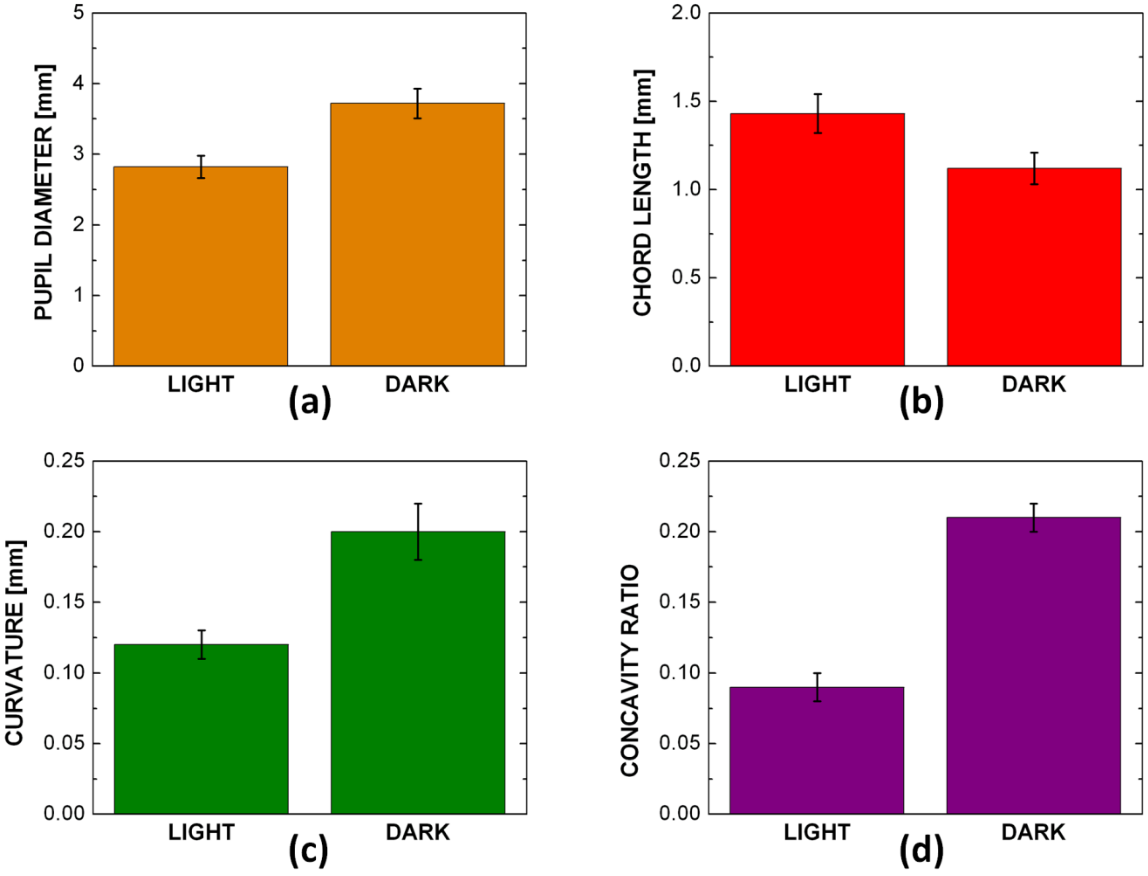

Figure A-7 Ex Vivo iris pupil diameter, chord length, curvature, and concavity ratio results.

The iris cross-sectional area (Figure A-8a) and volume (Figure A-8b) both showed a significant decrease. The cross-sectional area of iris decrease from 0.34 ± 0.02 mm to 0.32 ± 0.01 mm^2 ($p < 0.05$) where the iris volume decreased from 1.74 ± 0.13 μL to 1.64 ± 0.14 μL ($p < 0.05$) following activation of the dilator muscle.

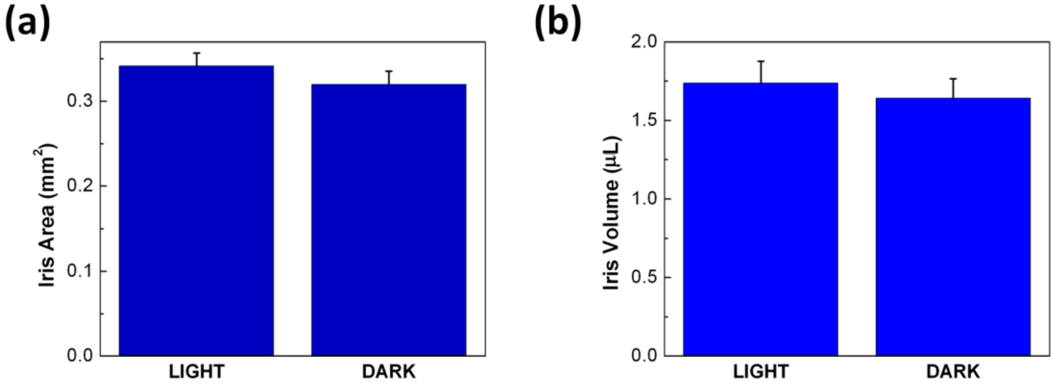

Figure A-8 Ex Vivo (a) iris cross-sectional area and (b) volume results.

A.4.3 *In Silico* Studies

Figure A-9 shows the iris deformation following dilation in a typical ex vivo experiment compared with the three simulation results created based on the undeformed geometry the tissue. In both the experiment (Figure A-9a) and the realistic model, in which the dilator muscle was positioned in the posterior portion of the iris (Figure A-9b), the iris curvature increased and the iris chord length decreased. The unrealistic models, however, did not predict the experimental results correctly. Positioning the dilator anteriorly within the iris led to a smaller increase in the iris curvature following dilation (Figure A-9c). Modeling the whole thickness of iris as the active muscle led to a decrease in the iris curvature (i.e., shift to the posterior). As quantified in Figure A-10, the realistic model was the only one that predicted the iris concavity ratio following dilation consistently with the experimental results.

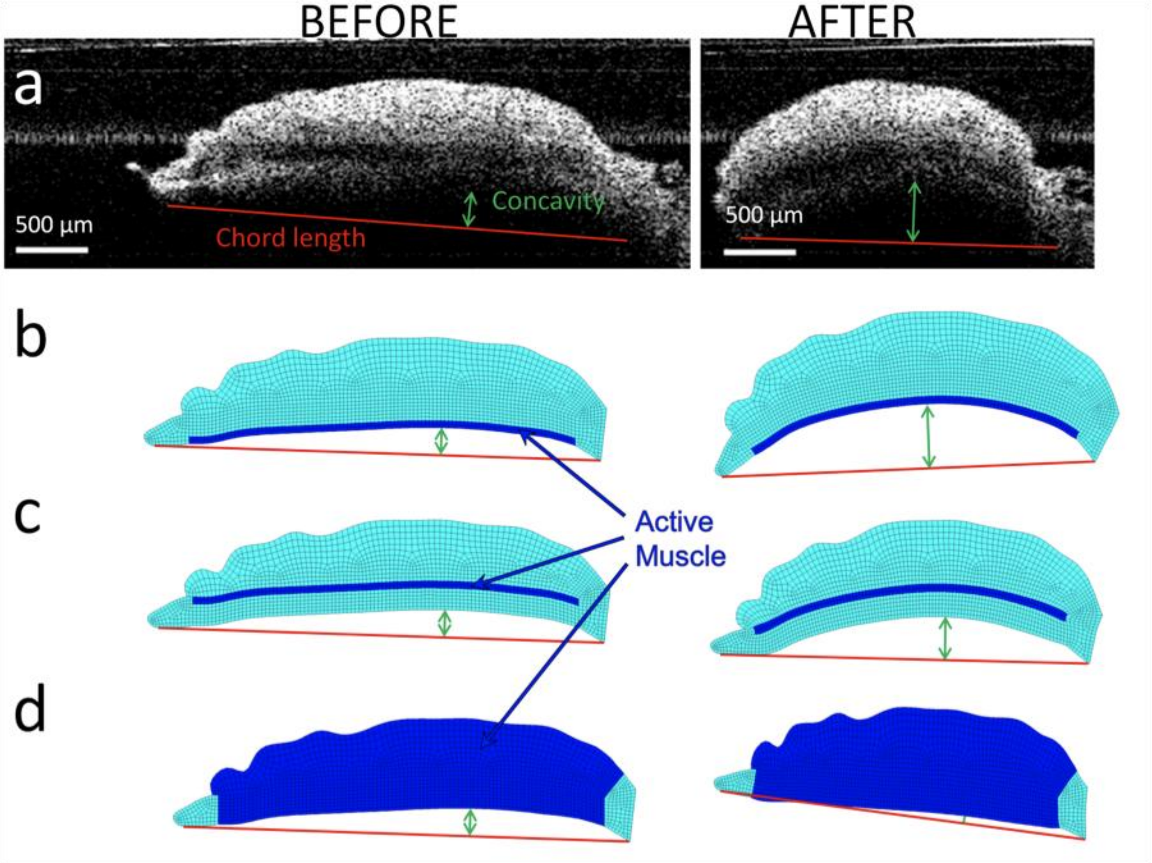

Figure A-9 Iris chord length and curvature before (left) and after (right) dilation in. (a) a typical ex vivo experiment, (b) an anatomical realistic model of the iris with the dilator muscle in the posterior, (c) an artificial model in which the dilator was positioned anteriorly, and (d) an artificial model in which the dilator was thickened throughout the entire iris contour.

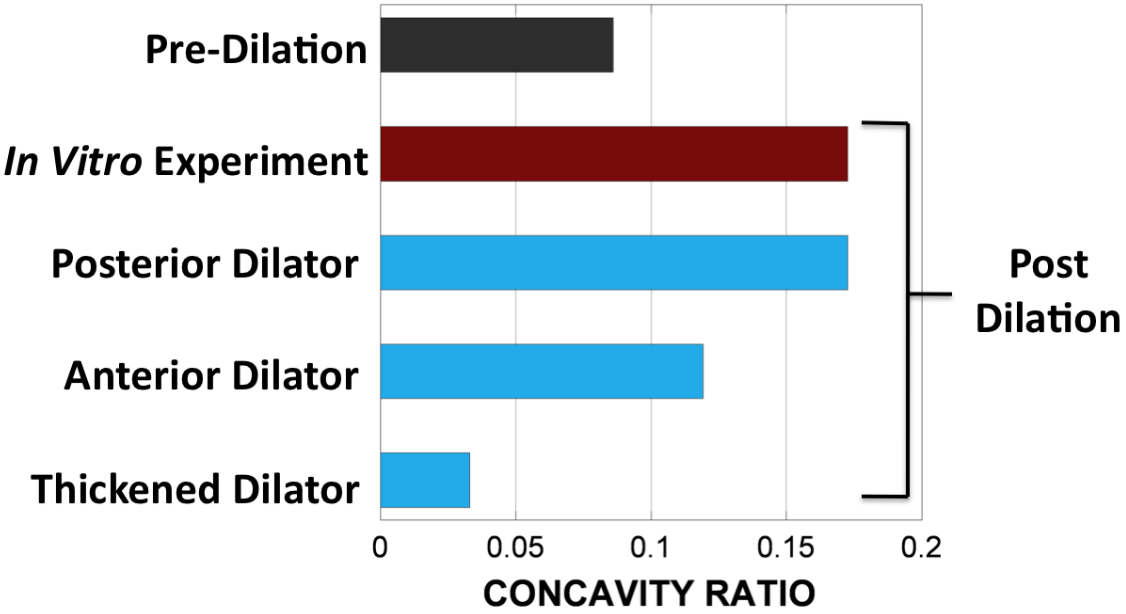

Figure A-10 Iris concavity ratio before and after dilation in a typical experiment and three models based on the geometry of the experiment.

A.5 Discussion

The major conclusion drawn from this work is that the location of the dilator itself can cause iris anterior bowing. Three different types of experiments (clinical, experimental, and computational) all confirmed the contribution of the dilator's position to a non-pupillary-block-dependent mechanism for anterior bowing.

While it is possible that the lack of radial symmetry in pinning of the *ex vivo* iris led to a small artifact, we observed no difference when more pins were used, so the two-pin method was deemed acceptable. We also have found previously [92] that *ex vivo* irides lose the ability to dilate approximate 5-6 hours post mortem, so it is essential that the eyes be harvested and tested quickly if the iris is the target. It is noted that *in vivo* studies were on patients who had received LPIs for narrow angles, so some effects that observed could have been more or less pronounced than they would be in the general population. Healthy subjects are not given LPIs, but LPI is used to treat pigmentary glaucoma patients, who could provide an alternative test group.

It has been suggested [16] that incompressibility of the iris (or inability of water to escape from the iris stroma) may contribute to the risk of angle narrowing or closure. The present study focuses on the contour as described by the posterior surface of the iris, so no conclusion can be drawn relative to the aforementioned studies, but it may be that a synergistic effect exists between dilator-induced curvature and the pushing of the iris into the angle. Both ideas must also be examined in light of the role of pupillary block.

Appendix B- Increased Iris-lens Contact Following Spontaneous Blinking: Mathematical Modeling

This work was part of the paper "Increased iris-lens contact following spontaneous blinking: Mathematical modeling" by R. Amini, S. Jouzdani, and V.H. Barocas, (J Biomech. 2012 Aug 31;45(13):2293-6. doi: 10.1016/j.jbiomech.2012.06.018. Epub 2012 Jul 21. (American Society of Mechanical Engineers as the copyright holder is acknowledged))

B.1 Summary

The purpose of this work was to study *in silico* how iris root rotation due to spontaneous blinking alters the iris contour. An axisymmetric FE model of the anterior segment was developed that included changes in the iris contour and the AH flow. The model geometry was based on average values of ocular dimensions. Blinking was modeled by rotating the iris root posteriorly and returning it back to the anterior. Simulations with maximum rotations of 2°, 4°, 6°, and 8° were performed. The iris-lens contact distance and the pressure difference between the posterior and anterior chambers were calculated. When the peak iris root rotation was 2°, the maximum iris-lens contact increased gradually from 0.28 to 0.34 mm within eight blinks. When the iris root was rotated 6° and 8°, the pressure difference between the posterior and anterior chambers dropped from a positive value (1.23 Pa) to negative values (-0.86 and -1.93 Pa) indicating the presence of reverse pupillary block. Apparent iris-lens contact increased with steady blinking, and the increase became more pronounced as posterior rotation increased. We conclude that repeated iris root rotation caused by blinking could maintain the iris in a

posterior position under normal circumstances, which would then lead to the clinically-observed anterior drift of the iris when blinking is prevented.

B.2 Introduction

In the anterior eye, AH (henceforth “aqueous”) is secreted from the ciliary body into to the posterior chamber, flows through the gap between the lens and iris into the anterior chamber, and finally drains via the trabecular meshwork (Figure 2-1b). Aqueous brings oxygen and nutrients to avascular ocular tissues, notably the lens and cornea. Resistance to aqueous outflow generates IOP. A typical IOP value of 10–15 mmHg (1300–2000 Pa) is necessary for normal function of the eye [8]. Increased IOP, although not a defining criterion for glaucoma [37], is widely accepted as a major risk factor [116-119].

The iris configuration can affect the IOP and has been used to classify different types of glaucoma [120]. For example, in primary ACG, the peripheral iris blocks the aqueous outflow pathway. Angle closure derives its name from the closed or narrowed angle between the anterior surface of the iris and posterior surface of the cornea.

Unlike angle closure, pigmentary glaucoma occurs when the iris is abnormally bowed towards the posterior. Although the cause of iris posterior bowing is not known for certain, “reverse pupillary block” has been proposed as a possible explanation [46]. In reverse pupillary block, a transient elevation of the pressure in the anterior chamber pushes the iris towards the posterior and pins the iris tip against the lens surface. Consequently, the aqueous flow from the anterior chamber to the posterior chamber is transiently blocked, and iris bowing is prolonged until the aqueous pressure in the anterior chamber is lower than that of the posterior chamber. Reverse pupillary block may be initiated by accommodation [47, 48, 79] or corneoscleral indentation [49]. External indentation of the cornea and/or sclera by various objects [31, 121-124] is known to cause opening of the ACA, possibly via whole-globe deformation and consequent posterior rotation of the iris root [125]. Although no external object indents the corneoscleral surface during blinking, changes in the iris contour [86, 111] and in IOP [126, 127], observed experimentally, suggest that a similar mechanism occurs. In particular, in eyes with pigmentary glaucoma [86, 111], narrow angles [86], and healthy controls [86], when blinking was prevented by the presence of an eye cup for UBM examination, the iris drifted anteriorly. Considering the similarities between blinking and corneoscleral indentation, these observations suggest that during each blink, pressure on the corneoscleral surface from the eyelids leads to iris root rotation, altering aqueous flow and iris contour.

As shown in our previous work [49], due to reverse pupillary block, even an extremely short-duration (~ms) rotation of the iris root can require a long recovery time (~min); a normal individual blinks every 2-4 seconds [84, 85]. Therefore, before the iris can recover fully from one blink, a new blink occurs. We hypothesize that regular blinking prevents the full recovery of the iris-aqueous system and keeps the iris in a posterior position. Prevention of blinking would allow the iris-aqueous system to reequilibrate and consequently would lead to the observed anterior drift of the iris. In this paper, we explore the hypothesis via a FE model of the anterior segment[38, 48, 49].

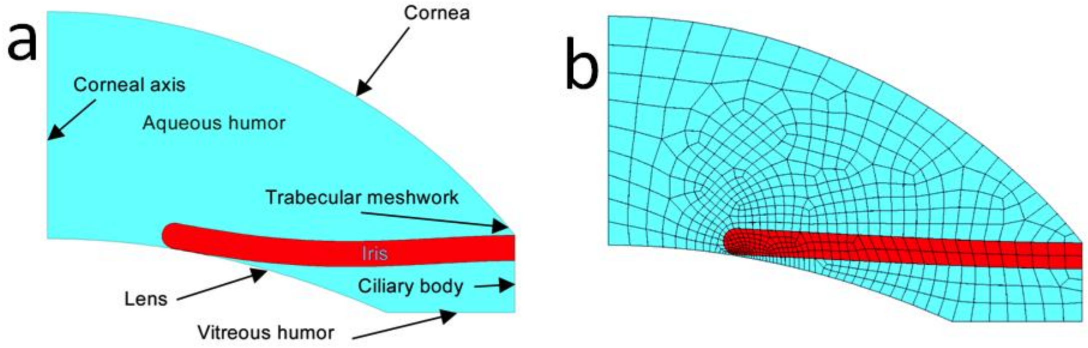

Figure B-1 Anterior segment model (a, b) was created based average geometrical values for healthy individuals from published data (Table 3-1).

B.3 Methodology

A FE model of aqueous-iris interaction was modified to simulate blinking (Table 3-1, Figure B-1). The governing equations and all of the boundary conditions except for the iris root rotation were identical to those discussed extensively in previous work [49]. Briefly, the iris was modeled as an incompressible neo-Hookean solid and the aqueous as incompressible viscous fluid. Geometry of model domain and the FE meshes were generated using GAMBIT (Fluent Inc., Lebanon, NH) via a paving technique. The Galerkin FE method was employed for spatial discretization of the mathematical model, and the implicit Euler method was used to solve the initial value problem.

We simulated each blink as 80 ms closing, no hold, and 200 ms opening, with one blink per every 3 seconds [84, 85]. The iris root was rotated posteriorly during 0.08 s using Drichlet boundary condition. The iris root was then rotated back to the pre-blinking (non-rotated) location over 0.2 s and followed by maintaining the pre-blinking configuration for 2.72 s to complete the three-second blink period (Figure B-2). These steps were repeated over time to simulate blinking.

Since no experimental data on the exact value of iris root rotation were available in the literature, we performed a parametric study on the effect of rotation angle. We repeated the simulation for four different iris root rotation angles. The maximum iris root rotations in the four cases studied were 2°, 4°, 6°, and 8°. The largest value of the parameter (i.e. 8°) was chosen as close to the value of iris root rotation due to the corneal indentation [125].

We calculated the apparent iris-lens contact and pressure difference between the anterior and posterior chambers. Apparent contact length, commonly used in UBM studies [111, 128-130], is defined as the distance over which there is no resolvable space between the iris and lens in the UBM image. In the computational model, we estimated the apparent contact as the distance over which the iris was at most 50 μm from the lens.

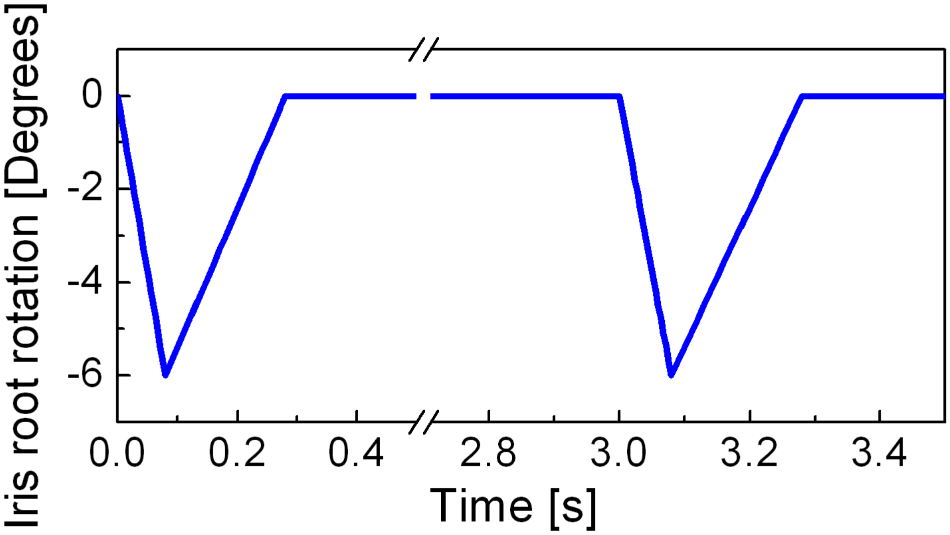

Figure B-2 Iris root angle during blinking for 6° posterior (negative) rotation. The iris was rotated towards the posterior in 0.08 s, rotated back in 0.2 s, and held for almost 2.72 s. Blinking was repeated every 3 seconds.

B.4 Results

Figure B-3 shows the iris-lens gap before blinking and immediately after the 10th blink. Before blinking, the iris-lens gap was open and aqueous flowed from the posterior to the anterior chamber (shown with an arrow in Figure B-3). As blinking continued, the iris tip became closer to the lens and the iris-lens gap narrowed. In the computational model, since the fluid domain was required to be continuous, a finite gap remained [48, 49]. Following blinking, however, the flow through the gap became negligibly small (< 2% of steady-date value).

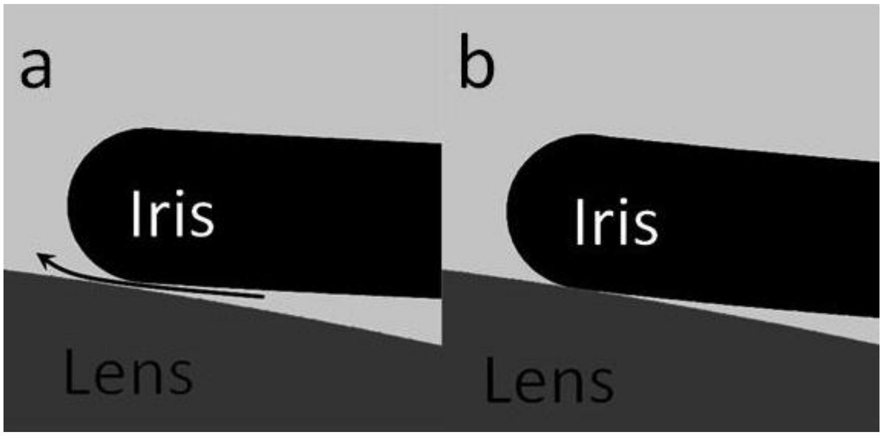

Figure B-3 The iris-lens gap without blinking (a) and after 10 blinks (b) simulated in the models (6° iris root rotation). When the iris-lens gap is not closed, the aqueous flows from the posterior chamber to the anterior chamber across the gap as shown schematically with an arrow.

During simulated repeated blinking, pressure difference between posterior and anterior chambers, ΔP, (Figure B-4a) and apparent iris-lens contact (Figure B-4b) stabilized after a few blinks. When the iris root was rotated 6° and 8° to the posterior, ΔP became negative, indicating higher pressure in the anterior chamber and the existence of reverse pupillary block. The parametric study (Figure B-5) showed a monotonic increase in iris-lens contact with iris rest rotation, as expected.

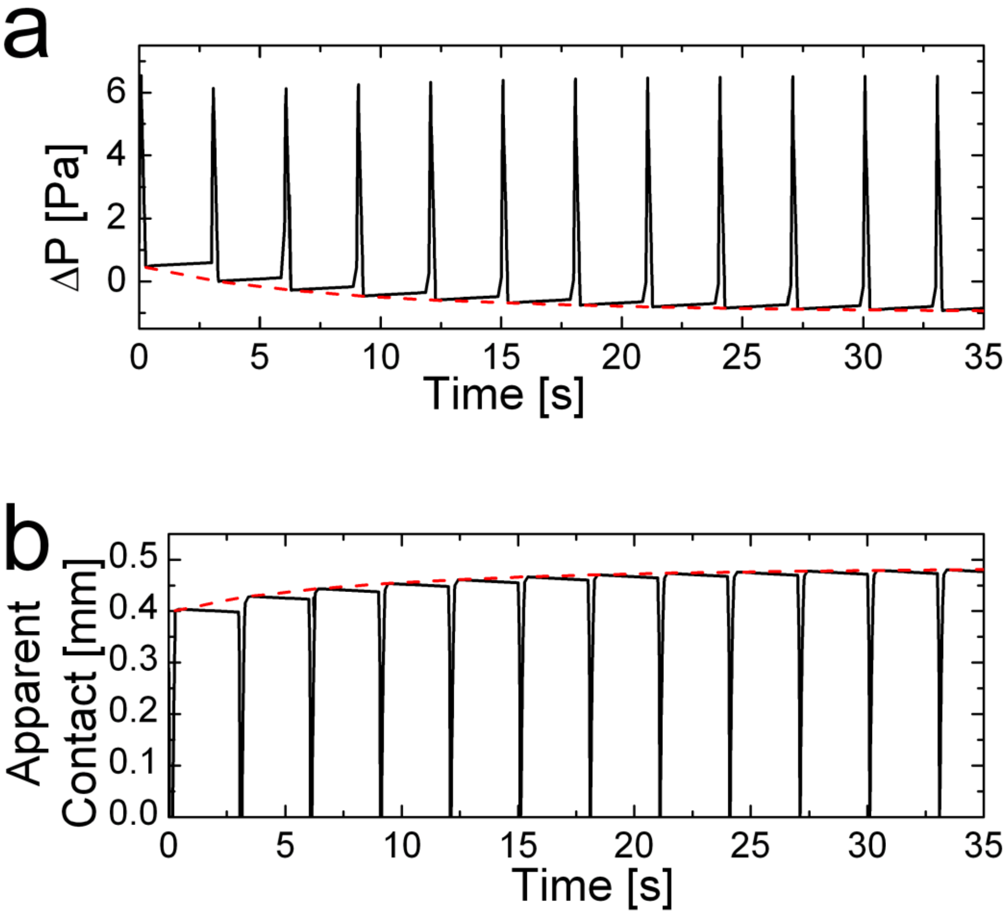

Figure B-4(a) ΔP, aqueous pressure difference between the posterior and the anterior chambers, and (b) apparent iris-lens contact as blinking prolongs (6° iris root rotation).

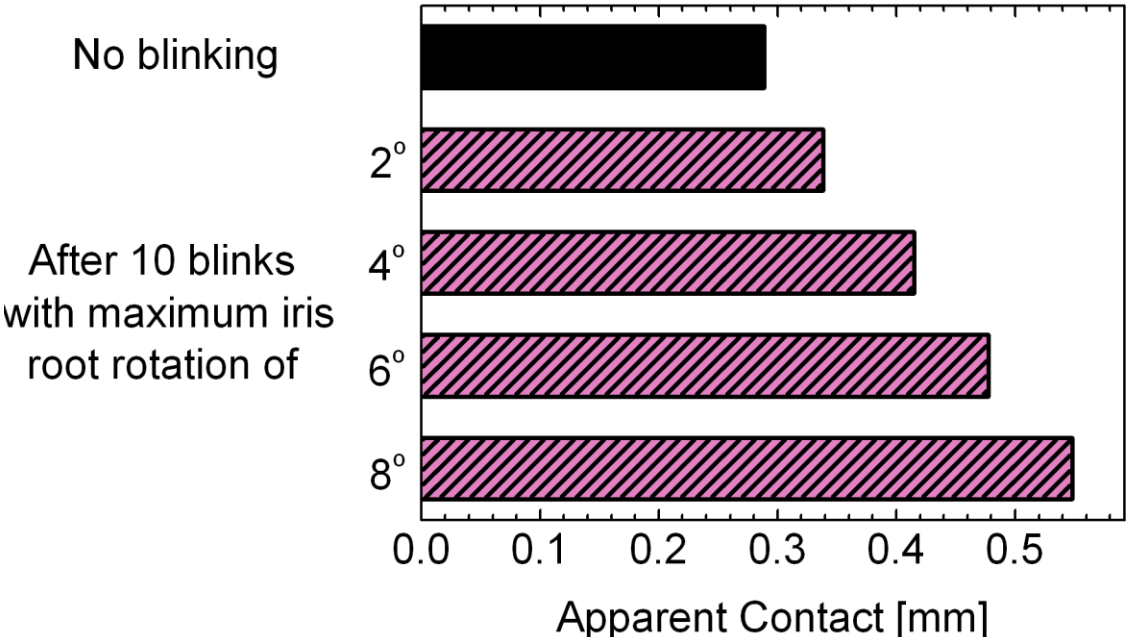

Figure B-5 The apparent iris-lens contact after 10 blinks when blinking was modeled using different iris root rotations (sparse bars) in comparison to the contact without blinking (solid bars).

B.5 Discussion

Our computational model showed that apparent iris-lens contact increased following blinking as aqueous was pumped from the posterior to the anterior chamber via iris motion. When an individual is awake and conscious, spontaneous blinking occurs every 2-4 seconds [84, 85], and the iris stays more toward the posterior. We suggest that in the absence of blinking, as in the initial condition of our model, the iris is more anteriorly located. Therefore, when blinking is prevented [86, 111], the aqueous-iris system returns to its blink-free steady-state, and the iris drifts forward.

In this study, we were not able to model globe deformation during blinking due to lack of quantitative experimental data on the effect of the ocular muscles. We expected that, similar to other cases of corneal indentation (e.g. indentation gonioscopy), the iris root would rotate to the posterior when the corneoscleral surface is pressurized by the eyelids during a blink. Parametric studies showed that regardless of how much the iris-root was rotated, the iris-lens contact increased. Based on our model, we conclude that the apparent iris-lens contact increases following prolonged blinking, but a precise estimate of the increase would require more information than is currently unavailable.

It should be noted that the elastic modules E = 27 kPa in the study was based on our previous published experimental data [66]. In particular, Heys and Barocas [66] performed mechanical testing on an incompressible bovine iris and in the radial direction. More recently, Whitcomb et al. [13] calculated the instantaneous and equilibrium modulus of porcine irides using indentation mechanical testing. Instantaneous modulus of 6.0 ± 0.6 kPa and 4.0 ± 0.5 kPa and equilibrium modulus of 4.4 ± 0.9 kPa and 2.3 ± 0.3 kPa, were reported for posterior and anterior surface of the porcine irides. Recently, Yoo et al. [93] also calculated the stiffness of different ocular tissues including the bovine irides using microindentation, and reported 4.86 kPa and 0.24 kPa, for instantaneous and equilibrium modulus of the bovine irides, respectively. Based on our previous work [48], we would expect that varying the elastic modulus would change the pressure difference between the posterior and anterior chamber, but would have no effect on the apparent iris-lens contact and iris curvature.

A recent study using imaging of the anterior eye [16] has proposed that the normal iris is compressible and that incompressibility of the iris (or inability of water to escape from the iris stroma) may contribute to the risk of angle narrowing or closure. In the present study, the iris was modeled as an incompressible homogeneous neo-Hookean solid, but other models could be explored.

Our model results indicate that posterior rotation of the iris every few seconds, as one might reasonably expect to occur during blinking, can induce reverse pupillary block and maintain the iris in a state of posterior bowing. When blinking is prevented, the iris can transition to a more anterior curvature over a few minutes, but upon resumption of blinking, the iris will return to the posterior configuration. All of these results are consistent with clinical observation. Our results suggest that although laser iridotomy, by allowing pressure equilibration across the iris, would lead to flattening of the iris but might not eliminate iris-lens contact, which could be driven by iris root rotation rather than by pressurization of the aqueous in the anterior chamber. That is the iris could still rub against the lens and zonules during every blink even though the rapid return to a flat contour because of the iridotomy would reduce the observable iris-lens contact to nearly zero.

Finally, it should be noted that Studies have shown there are several risk factors that may contribute to pigmentary dispersion glaucoma including large eye, age, sex, and race. For example it has been shown that have pigmentary glaucoma most commonly found in young, myopic, white males [90, 124]. A relative posterior position of the iris to the lens may also contribute to pigmentary dispersion glaucoma, however, by itself does not necessary imply the existence of pigmentary dispersion glaucoma.